

The Structure of  
Dark and Luminous Matter  
in Early-Type Galaxies



# The Structure of Dark and Luminous Matter in Early-Type Galaxies

Proefschrift

ter verkrijging van  
de graad van Doctor aan de Universiteit Leiden,  
op gezag van de Rector Magnificus prof. mr. P.F. van der Heijden,  
volgens besluit van het College voor Promoties  
te verdedigen op woensdag 9 september 2009  
klokke 16.15 uur

door

Anne-Marie Weijmans

geboren te Boxmeer  
in 1981

## Promotiecommissie

Promotor: Prof. dr. P. T. de Zeeuw

Overige leden: Prof. dr. R. G. Bower (Durham University)  
Prof. dr. M. Franx  
Prof. dr. A. Helmi (Rijksuniversiteit Groningen)  
Prof. dr. K. H. Kuijken  
Dr. R. Morganti (ASTRON / Rijksuniversiteit Groningen)  
Dr. J. Schaye



voor mama

Omslag: *De Sterrenplukster*  
door Clemens Weijmans

# Table of Contents

<b>1</b>	<b>Introduction</b>	<b>1</b>
1.1	Dark matter . . . . .	1
1.2	Dark matter in early-type galaxies . . . . .	2
1.3	Integral-field spectrography . . . . .	4
1.4	Dynamical models . . . . .	5
1.5	Stellar halo populations . . . . .	5
1.6	This thesis . . . . .	6
1.7	Conclusions and outlook . . . . .	9
<b>2</b>	<b>The dark matter halo in NGC 2974</b>	<b>11</b>
2.1	Introduction . . . . .	12
2.2	Observations and data reduction . . . . .	14
2.3	Analysis of velocity fields . . . . .	17
2.4	Rotation curve . . . . .	21
2.5	Mass model and dark matter content . . . . .	29
2.6	Summary . . . . .	43
2.7	Appendix: Asymmetric drift correction in a thin disc . . . . .	46
<b>3</b>	<b>Stellar velocity profiles out to <math>4 R_e</math></b>	<b>51</b>
3.1	Introduction . . . . .	52
3.2	Observations and data reduction . . . . .	55
3.3	Stellar kinematics . . . . .	57
3.4	Line strengths . . . . .	62
3.5	Dynamical models . . . . .	70
3.6	Summary and conclusion . . . . .	79
<b>4</b>	<b>The stellar and dark halo of NGC 2549</b>	<b>83</b>
4.1	Introduction . . . . .	84
4.2	Observations and data reduction . . . . .	86
4.3	Extraction of kinematics and line strengths . . . . .	88
4.4	Stellar population models . . . . .	96
4.5	Dynamical models . . . . .	99

4.6 Discussion and summary . . . . .	106
<b>5 The emission halo of LAB1</b>	<b>109</b>
5.1 Introduction . . . . .	110
5.2 Observations and data reduction . . . . .	112
5.3 Analysis . . . . .	114
5.4 Discussion and conclusion . . . . .	122
<b>Colour figures</b>	<b>125</b>
<b>Bibliography</b>	<b>135</b>
<b>Publicatielijst</b>	<b>139</b>
<b>Nederlandse samenvatting</b>	<b>143</b>
<b>Curriculum vitae</b>	<b>155</b>
<b>Nawoord</b>	<b>157</b>





---

# Chapter 1

---

## Introduction

Galaxies come in different shapes and sizes. Some have impressive spiral arms and dustlanes and are classified as spiral or *late-type* galaxies. Others have a simpler appearance, looking very smooth without any apparent structure. These systems are the elliptical and lenticular galaxies, or *early-type* galaxies (see Figure 1.1). How did these galaxies form, and how have they developed into such different shapes and sizes? These are some of the big questions that astronomers are attempting to solve.

### 1.1 Dark matter

In 1933 Swiss astronomer Fritz Zwicky made an important discovery. While studying galaxies in the Coma cluster, he found that the dynamical mass, mea-

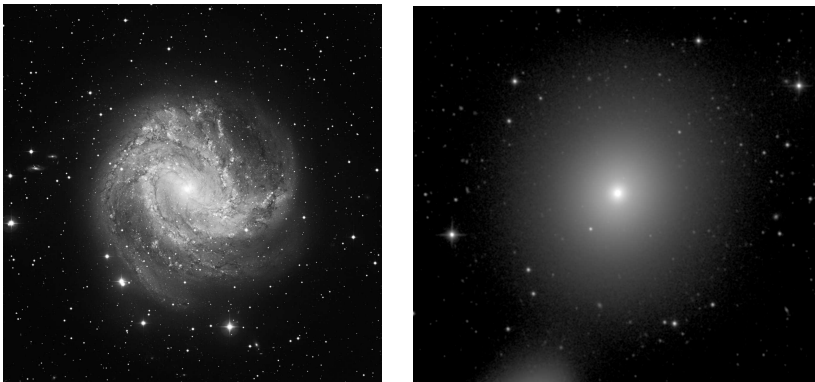


**Figure 1.1** — Two images of different types of galaxies. Left: spiral galaxy M83, captured by the Wide Field Imager of La Silla Observatory, Chile (Credit: ESO). Right: elliptical galaxy NGC 3379, imaged by the 1.3m McGraw-Hill Telescope of MDM Observatory, Kitt Peak, US.

sured by means of kinematics of the galaxies, far exceeded the luminous mass, formed by stars and gas in the cluster (Zwicky 1933). The implication of this discovery was that there had to be some kind of invisible mass, dark matter, to keep the galaxies in the cluster gravitationally bound. Later, more evidence was found for dark matter in the Universe. Rotation curves of neutral gas (H I) around spiral galaxies obtained with radio telescopes revealed that these systems are embedded in haloes of dark matter (e.g. Rubin et al. 1985; van Albada et al. 1985). Large clusters of galaxies acting as gravitational lenses also point to the existence of large amounts of dark matter (e.g. Soucail et al. 1988), and from observations of the cosmological background radiation, we know that the amount of dark matter in the Universe exceeds the amount of normal, baryonic matter by a factor five (Komatsu et al. 2009).

Dark matter is ubiquitous, and plays an important role in the formation and evolution of galaxies. In the current galaxy formation paradigm (e.g. Springel et al. 2005), the early Universe had a much smoother dark matter distribution than it has today. Through gravitational instabilities, dark matter started to form clumps and provided a framework for structure formation. Within these structures, gas cooled and formed stars. In order to understand galaxy formation and evolution, we therefore also need to study the structure and evolution of the dark matter haloes that surround them. That is the main topic of this thesis.

## 1.2 Dark matter in early-type galaxies

Dark haloes around late-type spiral galaxies have been observationally confirmed, using rotation curves of cold neutral gas. For early-type galaxies, observational proof of dark matter haloes is however much more difficult to obtain. Because the dark matter halo only starts to dominate over the luminous matter in the outskirts of the galaxy (beyond  $\sim 3$  effective radii  $R_e$ <sup>1</sup>) we need to trace the gravitational potential at large radii to map the dark halo. Large cold neutral gas discs (or rings), that extend far beyond the stellar disc, are ideal tracers of the gravitational potential, as the cold gas moves on circular orbits. But since these gas discs are only rarely found around early-type galaxies (though see Morganti et al. 2006 for recent discoveries of H I gas in these systems), we need to resort to other tracers of the gravitational potential in order to study dark haloes in these galaxies.

Instead of gas kinematics, stellar kinematics can in principle also be used to infer the dark matter distribution. However, galaxies fade relatively quickly with

---

<sup>1</sup>An effective radius or  $R_e$  is defined as the radius within which half the total light of the galaxy is contained, and is therefore also sometimes called a half-light radius.



radius, so that with traditional long-slit spectrography it is almost impossible to obtain spectra with sufficient signal-to-noise ( $S/N$ ) outside  $\sim 2 R_e$ . Mass models based on spectra out to this radius are not always conclusive, though many studies with long-slit spectra hint at the existence of dark matter haloes around early-type galaxies (e.g. Carollo et al. 1995; Rix et al. 1997).

X-ray observations of the hot interstellar medium can also be used to constrain the dark matter content of galaxies. Assuming hydrostatic equilibrium, the total mass profile can be recovered from density and temperature measurements (e.g. Humphrey et al. 2006; Pellegrini & Ciotti 2006). However, not all early-type galaxies contain a large enough amount of hot gas to be detected in X-ray, and the assumption of hydrostatical equilibrium has to be validated.

Weak gravitational lensing (e.g. Gavazzi et al. 2007) is another technique to study the mass and shapes of dark haloes around galaxies that are lensed by massive clusters. This technique is however not applicable to galaxies in the nearby Universe, as there are no nearby massive galaxy clusters that could act as gravitational lenses for these nearby systems. Strong gravitational lensing in combination with stellar dynamics has been used to determine the dark matter content of early-type galaxies that act as lenses themselves (e.g. van de Ven et al. 2008b; Barnabe et al. 2009).

Another approach to probe the gravitational potential in galaxies at large radii is by measuring the radial velocities of discrete tracers, such as globular clusters (e.g. Côté et al. 2003; Pierce et al. 2006) and planetary nebulae (e.g. Douglas et al. 2006; Napolitano et al. 2009). Both these tracers are visible in nearby (within  $\sim 50$  Mpc) galaxies: globular clusters because of their concentration of starlight emitted by hundred thousands of stars, and planetary nebulae because of their strong emission of the [O III] line.

With the Planetary Nebulae Spectrograph (Douglas et al. 2002) over one hundred planetary nebulae can be observed in a galaxy, allowing the construction of smoothed velocity and velocity dispersion maps (Cocato et al. 2009). However, obtaining higher order moments of the line-of-sight velocity distribution (LOSVD), such as the Gauss-Hermite moments  $h_3$  and  $h_4$ , requires an even larger number of measurements. These higher order moments, most importantly  $h_4$ , are needed to constrain the orbital structure of the galaxy, in order to break the mass-anisotropy relation (e.g. Gerhard 1993). Briefly, by replacing tangential orbits by radial ones (i.e. increasing the radial anisotropy over the tangential anisotropy) it is possible to increase the total mass of a spherical or axisymmetric system, for a decreasing or constant velocity dispersion profile (e.g. Richstone & Tremaine 1984; Dekel et al. 2005; de Lorenzi et al. 2009). However,  $h_4$  provides constraints

for the anisotropy, with positive  $h_4$  corresponding to more tangential anisotropy, while negative  $h_4$  indicates more radially anisotropic systems.

We therefore developed in this thesis a new technique to use integral-field spectrography to measure the LOSVD of the integrated stellar light at large radii. This way, we can measure also the higher order moments of the LOSVD and by not limiting ourselves to a discrete representation of the stellar population we are confident that indeed we are tracing the gravitational potential (e.g. Sambhus, Gerhard & Méndez 2006).

### 1.3 Integral-field spectrography

With integral-field spectrography we can simultaneously obtain spectra at each position in the field-of-view, resulting in a three dimensional datacube  $(x, y, \lambda)$ . From the spectra not only the kinematics of stars and gas, but also absorption line strengths of the stars can be obtained, providing means to determine metallicity and age of the system. All these quantities can be displayed in two dimensional maps. This is an enormous advantage over traditional long-slit spectrography, where in order to get the same spatial coverage, multiple slits need to be observed.

In this thesis we use the integral-field spectrograph SAURON (Spectrographic Aerial Unit for Research on Optical Nebulae, see also Bacon et al. 2001). This spectrograph has an optical system of lenslets to map the galaxy (see Figure 1.2), and is a visitor instrument at the William Herschel Telescope of the Isaac Newton Group at La Palma, Canary Islands, Spain. We develop a new observing technique to obtain stellar kinematics in early-type galaxies out to large radii, using SAURON as a 'photon-collector'. Even though the light collected by one lenslet is too faint to yield a spectrum with sufficient  $S/N$  to measure the LOSVD in the faint outskirts of galaxies, by combining the light of all 1400 lenslets we obtain a spectrum from which we can reliably extract the kinematics.

In one chapter we also use the integral-field spectrograph PPAK (Kelz et al. 2006), which is mounted at the 3.5m Telescope at Calar Alto, Spain. This spectrograph works with fibers instead of lenslets, and has a lower spatial resolution than SAURON: the diameter of one fiber is 2.7 arcsec, while SAURON has lenslets that measure  $0.94 \times 0.94$  arcsec. However, the field-of-view of PPAK is four times as large as that of SAURON and its spectral range is also longer, allowing us to measure a larger number of line strength indices.

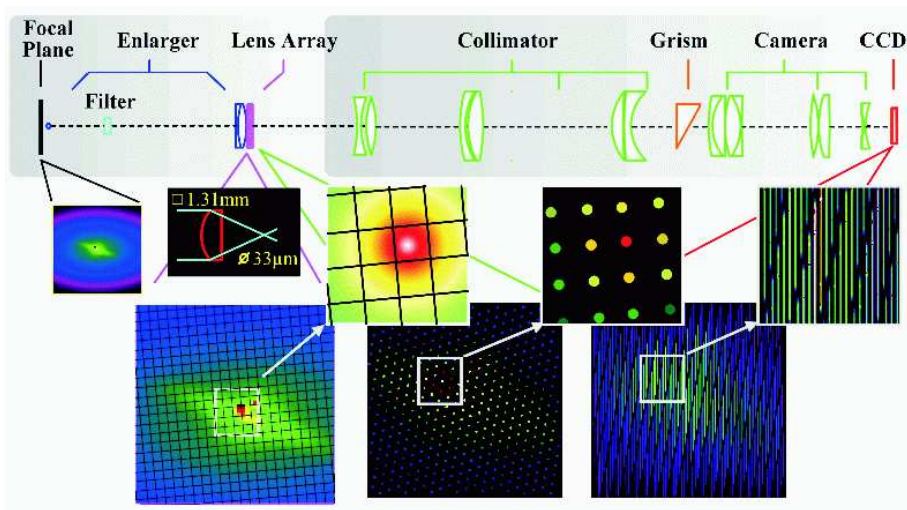


**Figure 1.2** — Optical lay-out of the integral-field spectrograph SAURON. Light within the desired wavelength interval (4810 - 5350 Å) is selected by a filter, after which it hits the central part of the instrument, which consists of a matrix of lenslets. Each lenslet maps its infalling light beam on a pinhole, after which a grism breaks up the light in a spectrum. The spectra are imaged on a CCD under a small angle (about  $6^\circ$ ) to prevent overlap between adjacent spectra. See Bacon et al. (2001) for a detailed description of the instrument and data processing.

## 1.4 Dynamical models

In this thesis we mostly make use of Schwarzschild orbital superposition models (Schwarzschild 1979), to find the properties of the dark haloes around our observed galaxies. In an a priori specified potential we calculate stellar orbits, which are stored in a library. From this library a superposition of orbits is calculated, that best fits the observed LOSVD (including higher order Gauss-Hermite moments), as well as the observed surface brightness. These models are fully general, and yield best-fit parameters such as viewing angles, mass-to-light ratio and halo mass. They also allow a study of the intrinsic orbital structure, to identify different orbit families and the presence of separate components.

## 1.5 Stellar halo populations

Stellar absorption line strengths trace the properties of the stellar population. Based on these measurements, stellar population models (e.g. Bruzual & Charlot 2003; Thomas, Maraston & Bender 2003; Schiavon et al. 2007) can pro-

vide several quantities, such as age, metallicity and stellar mass-to-light ratios. With integral-field spectrography we can now for the first time measure these line strengths outside  $2 R_e$ , to study the stellar halo population. In this thesis we study line strength gradients and investigate the connection between stellar populations and halo mass at large radii.

The behaviour of line strengths as a function of radius provides strong constraints for the starformation and merging history of a galaxy. Briefly, if galaxies form in a monolithic collapse, the line strengths are expected to follow a steep gradient (Carlberg 1984). Mergers however can dilute these gradients (White 1980), but subsequent starformation triggered by the merger can steepen the gradients again in the central part of the galaxy (Hopkins et al. 2009b).

There exists a tight relation between local line strength index (most notably the magnesium absorption line  $Mg\ b$ ) and the local escape velocity  $V_{\text{esc}}$  (e.g. Davies, Sadler & Peletier 1993; Scott et al. 2009). This relation was also observed for colours and  $V_{\text{esc}}$  (Franx & Illingworth 1990), reflecting the fact that colours trace metallicity in a galaxy. By including a dark halo into the gravitational potential of the galaxy,  $V_{\text{esc}}$  becomes larger. This effect is relatively larger at large radii: a test-particle at larger radii would perhaps have escaped relatively easy from the potential well of the luminous matter in the galaxy, but now also has to overcome the halo potential. The result is that at large radii the shift in  $V_{\text{esc}}$  is larger than at smaller radii, close to the centre of the galaxy. This introduces a change in slope of the  $Mg\ b - V_{\text{esc}}$  relation, when taking the halo into account (see also Franx & Illingworth 1990).

## 1.6 This thesis

In this thesis we explore new techniques to study the dark and luminous matter in the outskirts of galaxies.

In **Chapter 2** we use the Very Large Array (VLA) to map the H I ring around the early-type NGC 2974. This gas ring extends out to  $5 R_e$  (24 kpc) and displays regular rotation. We compare the kinematics of the H I with the ionised gas and stellar kinematics in the central  $R_e$  of the galaxy, as observed by SAURON. Both neutral and ionised gas share the same kinematics, which supports the view that they form one coherent gas structure. To combine the kinematics of the cold and warm gas, we apply an asymmetric drift correction (see e.g. Binney & Tremaine 2008, section 4.8.2) to the observed rotation curve of the latter. This is needed because the ionised gas has a high velocity dispersion, which is a measure of random motions. The cold gas does not have this high dispersion and is on circular

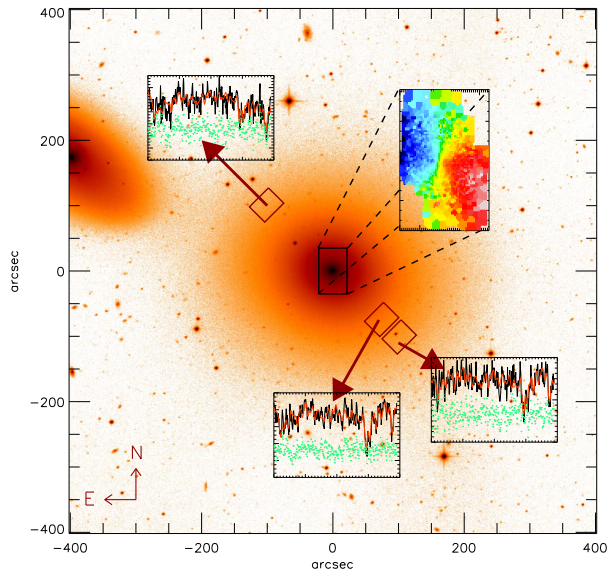


**Figure 1.3** — Illustration of the usage of SAURON as a ‘photon-collector’. The underlying image is a  $V$ -band image of early-type galaxy NGC 3379. In the central part of the galaxy,  $S/N$  in individual spectra is high, and we can construct kinematic maps, where binning of spectra is only needed along the edges of the field-of-view (FoV), where the galaxy is fainter. At large radii ( $3$  and  $4 R_e$ ) we bin the light of all spectra within the SAURON FoV together, in order to obtain a spectrum with sufficient  $S/N$  to measure the stellar kinematics. See colour supplement for a colour version of this figure.

orbits, and therefore its observed rotation curve agrees with its circular velocity, which traces the gravitational potential. After this correction is done, we combine the rotation curves of the central warm gas with the cold gas in the outskirts, and construct mass models of this galaxy. We find that NGC 2974 is surrounded by an axisymmetric dark halo, and that within  $5 R_e$  at least 55% of the total mass is dark.

**Chapter 3** deals with two other early-type galaxies: NGC 3379 and NGC 821. These galaxies are not detected in H I and therefore we need to obtain stellar kinematics in order to model the haloes of these systems. We use SAURON as a ‘photon-collector’ to measure the LOSVD at  $3$  and  $4 R_e$ . Combining these measurements at large radii with the SAURON kinematics maps covering the inner  $R_e$  of these galaxies (see Figure 1.3), we construct triaxial Schwarzschild models and add a dark halo to the potential. We find that both galaxies contain dark matter haloes: for NGC 3379, at least 34% of the total mass within  $4 R_e$  is dark, while for NGC 821 this percentage is even higher, at least 49%. We also find that the orbital structure of our best-fitting models becomes radially anisotropic at larger

radii, but that an increase of halo mass does not translate into an increase of radial anisotropy, as observed in spherical models (e.g. Richstone & Tremaine 1984). More studies of the orbital structure in triaxial models are needed to understand this trend. We also obtained line strengths from the spectra at large radii, and for the first time confirm that line strength gradients observed within  $1 R_e$  extend out to at least  $4 R_e$ . Constructing the  $\text{Mg } b - V_{\text{esc}}$  relation, we find that the slope of this relation steepens by including the dark halo in our model, as was previously found by Franx & Illingworth (1990) using colours instead of line strength indices.

In **Chapter 4** we observe the early-type galaxy NGC 2549 with the integral-field spectrograph PPAK. We compose a mosaic of four pointings, mapping the galaxy out to almost  $5 R_e$ . The stellar kinematic maps show that this galaxy has a disc-like rotation out to the edge of the observed field. Also there are indications of a disc component, embedded in a larger disc or bulge. From the line strengths we construct age and metallicity maps, and these also provide some evidence for a younger, metal-enriched central component. The line strength gradients remain stable from  $0.1$  to at least  $4 R_e$ .

The line strength maps allow us to construct a map of the stellar mass-to-light ratio, and we find only small variations over the observed galaxy field. While constructing a mass model based on the PPAK spectra, complemented with higher spatial resolution SAURON kinematics for the inner  $R_e$ , we find that dark matter is necessary to explain the observations, and that therefore like the galaxies studied in Chapters 2 and 3, NGC 2549 is embedded in a dark matter halo, with at least 63 per cent of the total mass being dark within  $5 R_e$ . We find however that our models cannot reproduce the observed rise in velocity dispersion at larger radii. Most likely this is caused by the limitations on the shape of the dark halo in our models, which we have kept fixed to spherical. This could imply that kinematics over the full field-of-view (in contrast to discrete measurepoints as we obtained in Chapter 3) can be used to constrain the shape of the dark halo. This is currently under investigation.

Finally, we turn our attention in **Chapter 5** to the high-redshift Universe. With SAURON we study the structure and kinematics of a  $\text{Ly}\alpha$  emitting gas cloud at  $z = 3.1$ . This object, Lyman Alpha Blob 1 (LAB1), is situated in a dense proto-cluster environment, and is the largest LAB discovered to date, with diameter  $> 100$  kpc. LABs are still mysterious objects, as it is not clear what powers the ionisation of these gas clouds. Proposed scenarios include photo-ionisation (possibly by massive starbursts and/or AGN, obscured along our line-of-sight), cooling flows, and superwinds caused by overlapping supernova remnants. With our deep (23.5 hrs) SAURON observations we find that LAB1 is not one large



coherent structure, but instead consists of five separate blobs. Two of these blobs are identified with Lyman Break Galaxies and a third is most likely associated with a dust-obscured submillimeter galaxy. The remaining two blobs cannot be connected with any source in the optical or infra-red, and could be genuine gas clouds trapped in the proto-cluster potential.

## 1.7 Conclusions and outlook

By using integral-field spectrography it has now become possible to measure the LOSVD and absorption line strengths of integrated stellar light out to large radii in early-type galaxies. We explore the behaviour of line strength gradients and subsequently investigate differences in age, metallicity and stellar mass-to-light ratio ( $M_*/L$ ). These studies provide important constraints for the starformation and merger histories of early-type galaxies. By constructing dynamical models based on the observed LOSVD we can map the dark haloes around early-type galaxies, similar to what was done for spiral galaxies with HI kinematics, and build statistical sample of halo properties, as a function of galaxy type and environment.

Our dynamical models however have still room for improvement. One of the main uncertainties in our models is  $M_*/L$ . Most models in this thesis have used a maximal spheroid (or equivalently: minimal halo) assumption, with  $M_*/L$  fixed to its maximal value, as allowed by the observed kinematics. Therefore the dark matter fractions we found for these galaxies are lower limits: the actual halo could very well be heavier. In Chapter 4 we explored the determination of  $M_*/L$  from stellar population models. This requires accurate measurements of multiple line strength indices. With spectra over long wavelength ranges, possibly complemented with colour measurements (e.g. Zibetti, Charlot & Rix 2009), we can start to remove this uncertainty from our dynamical models.

Another assumption in our models concerns the shape and profile of the dark halo. Most galaxy formation theories predict triaxial haloes (e.g. Frenk et al. 1988; Hayashi, Navarro & Springel 2007), while we so far modeled our galaxies with spherical haloes. Also, although structure formation simulations find cuspy haloes (such as the NFW profile that we utilized in this thesis, see Navarro, Frenk & White 1996), observations of nearby low-surface brightness and dwarf galaxies point to haloes with central cores (e.g. de Blok et al. 2008). We need to investigate whether with kinematics over a large field-of-view (Chapter 4) we can distinguish between different halo shapes and profiles.

In order to understand the evolution of dark haloes, we should also explore

the dynamics of galaxies at higher redshift. Obtaining kinematic maps of galaxies at high redshift is not straightforward: these systems are faint and small, so that we need long integrations times and high spatial resolution (Chapter 5). Still, integral-field spectrographs with high spatial resolution have already been employed to obtain the gas kinematics of disc galaxies at  $z \sim 2$  (e.g. Shapiro et al. 2008; van Starckenburg et al. 2008). Also, by using gravitational lenses, some lensed galaxies residing at  $z = 1$  have been mapped with a resolution comparable to  $z = 0.1$  galaxies (e.g. Swinbank et al. 2006). Observationally there has been a lot of progress in the study of high-redshift kinematics, and now modeling techniques should be developed to analyse these systems in more detail.

Our ultimate goal is to understand the formation and evolution of galaxies. Observations of galaxies nearby and at high redshift show us how galaxies change in time, due to starformation and interactions with other galaxies. If we want to understand these observations, we need to develop a theoretical framework to explain them. Simulations of galaxy formation are not always in agreement with observations, predicting haloes that are too massive or too concentrated (e.g. Napolitano et al. 2009). We therefore need to bring theory and observations together, to solve the mysteries that still surround the formation and evolution of galaxies.



---

## Chapter 2

---

# The shape of the dark matter halo in the early-type galaxy NGC 2974

We present H I observations of the elliptical galaxy NGC 2974, obtained with the Very Large Array. These observations reveal that the previously detected H I disc in this galaxy (Kim et al.

1988) is in fact a ring. By studying the harmonic expansion of the velocity field along the ring, we constrain the elongation of the halo and find that the underlying gravitational potential is consistent with an axisymmetric shape.

We construct mass models of NGC 2974 by combining the H I rotation curve with the central kinematics of the ionised gas, obtained with the integral-field spectrograph SAURON. We introduce a new way of correcting the observed velocities of the ionised gas for asymmetric drift, and hereby disentangle the random motions of the gas caused by gravitational interaction from those caused by turbulence. To reproduce the observed flat rotation curve of the H I gas, we need to include a dark halo in our mass models. A pseudo-isothermal sphere provides the best model to fit our data, but we also tested an NFW halo and Modified Newtonian Dynamics (MOND), which fit the data marginally worse.

The mass-to-light ratio  $M/L_I$  increases in NGC 2974 from  $4.3 M_\odot/L_{\odot,I}$  at one effective radius to  $8.5 M_\odot/L_{\odot,I}$  at  $5 R_e$ . This increase of  $M/L$  already suggests the presence of dark matter: we find that within  $5 R_e$  at least 55 per cent of the total mass is dark.

Anne-Marie Weijmans, Davor Krajnović, Glenn van de Ven, Tom A. Oosterloo,  
Raffaella Morganti & P. Tim de Zeeuw  
*Monthly Notices of the Royal Astronomical Society*, **383**, 1343–1358 (2008)

## 2.1 Introduction

Although the presence of dark matter dominated haloes around spiral galaxies is well established (e.g. van Albada et al. 1985), there is still some controversy about their presence around early-type galaxies. Spiral galaxies often contain large regular H I discs, which allow us to obtain rotation curves out to large radii, and therefore we can constrain the properties of their dark haloes. But these discs are much rarer in elliptical galaxies (e.g. Bregman, Hogg & Roberts 1992), so that for this class of galaxies we are often required to use other tracers to obtain velocity measurements, such as stellar kinematics, planetary nebulae or globular clusters. These tracers however are not available for all early-type galaxies, and give mixed results (e.g. Rix et al. 1997; Romanowsky et al. 2003; Bridges et al. 2006).

With the increase in sensitivity of radio telescopes, it has been discovered that many early-type galaxies in the field do contain H I gas, though with smaller surface densities than in spiral galaxies (e.g. Morganti et al. 2006). The average H I surface density in the Morganti et al. sample is around  $1M_{\odot} \text{ pc}^{-2}$ , which is far below the typical value for spiral galaxies ( $4 - 8M_{\odot} \text{ pc}^{-2}$ , e.g. Cayatte et al. 1994). This would explain why previously only the most gas-rich early-type galaxies were detected in H I. Morganti et al. find that H I can be present in different morphologies: H I discs seem to be as common as off-set clouds and tails, though they occur mostly in the relatively gas-rich systems.

Recently rotation curves of H I discs in low surface brightness galaxies and dwarf galaxies, complemented with H $\alpha$  observations, have been used not only to confirm the existence of dark matter haloes, but also to obtain estimates on the inner slope of the density profiles of the haloes (e.g. van den Bosch et al. 2000; Woldrake, de Blok & Walter 2003). Simulations within a cold dark matter (CDM) cosmology yield haloes with cusps in their centres (NFW profiles, see Navarro, Frenk & White 1996), but observations suggest core-dominated profiles (e.g. de Blok & Bosma 2002; de Blok 2005).

Detailed studies of rotation curves of early-type galaxies that contain H I discs are sparser, due to lack of spatial resolution: to detect low H I surface densities, larger beams are needed. Also, only few early-type galaxies have H I discs that are extended and regular enough to allow for detailed studies. Comparing  $M/L$  values at large radii, derived from H I velocities, to  $M/L$  at smaller radii measured from ionised gas kinematics, the conclusion is that early-type galaxies also have dark matter dominated haloes (e.g. Bertola et al. 1993; Morganti et al. 1997; Sadler et al. 2000). Franx, van Gorkom & de Zeeuw (1994) used the H I ring of the elliptical galaxy IC 2006 to determine not only the mass, but also the shape of the dark halo. They concluded that IC 2006 is surrounded by an axisymmetric dark halo, using

Parameter	Value
Morphological Type	E4
$M_B$ (mag)	-20.07
Effective $B - V$ (mag)	0.93
PA ( $^\circ$ )	41
Distance modulus (mag)	31.60
Distance (Mpc)	20.89
Distance scale (pc arcsec $^{-1}$ )	101.3
Effective radius (arcsec)	24

**Table 2.1** — Properties of NGC 2974. The values are taken from the Lyon/Meudon Extragalactic Database (LEDa) and corrected for the distance modulus, which is taken from the surface brightness fluctuation measurements by Tonry et al. (2001). Note that 0.06 mag is subtracted to adjust to the Cepheid zeropoint of Freedman et al. (2001); see Mei et al. (2005), section 3.3, for a discussion. The effective radius is taken from Cappellari et al. (2006).

the geometry of the ring and an harmonic expansion of its velocity map.

In this paper, we present a similar analysis of the regularly rotating H I ring around the elliptical (E4) field galaxy NGC 2974. Kim et al. (1988) observed this galaxy before in H I but their data had lower spatial resolution than ours, and they found a filled disc instead of a ring. Cinzano & van der Marel (1994) found an embedded stellar disc in their dynamical model of this galaxy, based upon long-slit spectroscopic data, but Emsellem, Goudfrooij & Ferruit (2003) constructed a dynamical model of NGC 2974 based on TIGER integral-field spectrography and long-slit stellar kinematics, that does not require a hidden disc structure. They did report the detection of a two-arm gaseous spiral in the inner 200 pc of NGC 2974 from high resolution WFPC2 imaging. Krajnović et al. (2005) constructed axisymmetric dynamical models of both the stars and ionised gas based upon SAURON integral-field data. These models require a component with high angular momentum, consisting of a somewhat flattened distribution of stars, though not a thin stellar disc. Emsellem et al. (2007) classify NGC 2974 as a fast rotator, which means that it possesses large-scale rotation and that its angular momentum is well defined. Some of the characteristics of NGC 2974 are given in Table 2.1.

For our analysis of NGC 2974 we combine kinematics of neutral gas, obtained from our observations with the Very Large Array (VLA), with that of ionised gas, obtained with the integral-field spectrograph SAURON (Bacon et al. 2001). This combination of a small scale two-dimensional gas velocity map in the centre of

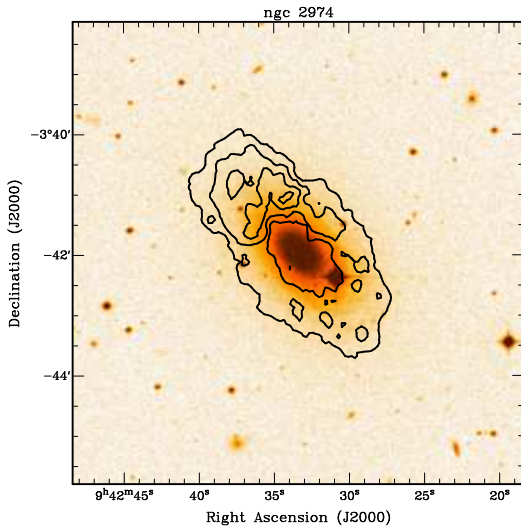


**Figure 2.1** — Total H I intensity contours superimposed onto the Digital Sky Survey optical image of NGC 2974. Contour levels are  $1, 3, 5$  and  $7 \times 10^{20} \text{ cm}^{-2}$ . The beamsize is  $19.9 \times 17.0$  arcseconds.

the galaxy, and a H I velocity map at the outskirts, allows measurements of a rotation curve ranging from 100 pc within the centre of the galaxy to 10 kpc at the edges of the H I ring. We use this rotation curve, together with ground- and space based optical imaging, to determine the dark matter content in NGC 2974, and to constrain the shape of the dark halo.

In section 2.2, we discuss the two datasets and their reduction, and describe the H I ring. We concentrate on the analysis of the velocity maps in section 2.3. Section 2.4 is devoted to the rotation curve that we extract from the velocity maps, and in section 2.5 we show mass models with various halo models, and find the best fit to the rotation curve. Section 2.6 summarizes our results.

## 2.2 Observations and data reduction

### 2.2.1 VLA observations

Earlier VLA observations (Kim et al. 1988) of NGC 2974 showed that this galaxy contains a significant amount of H I that, in their observations, appears to be distributed in a regularly rotating disc. Given the modest spatial and velocity resolution of those observations, we re-observed NGC 2974 with the VLA C-array while also using a different frequency setup that allows us to study this galaxy at both higher spatial and higher velocity resolution. The observations were performed on 11 and 19 September 2005 with a total on-source integration time of 15 hours. In each observation, two partially overlapping bands of 3.15 MHz and

64 channels were used. The two bands were offset by  $500 \text{ km s}^{-1}$  in central velocity. This frequency setup allows us to obtain good velocity resolution over a wide range of velocities (about  $1080 \text{ km s}^{-1}$ ).

The data were calibrated following standard procedures using the MIRIAD software package (Sault, Teuben & Wright 1995). A spectral-line data cube was made using robust weighting (robustness = 1.0) giving a spatial resolution of  $19.9'' \times 17.0''$  and a velocity resolution of  $20.0 \text{ km s}^{-1}$  (after Hanning smoothing). The noise in the final datacube is  $0.23 \text{ mJy beam}^{-1}$ .

To construct the total H I image, a mask was created using a datacube that was smoothed to about twice the spatial resolution and that was clipped at twice the noise of that smoothed datacube. The resulting total H I is shown in Figure 2.1, and our observations show that the H I is distributed in a regular rotating ring instead of a filled disc. The inner radius of the ring is approximately  $50''$  ( $\sim 5 \text{ kpc}$ ) and extends to  $120''$ , which corresponds to  $12 \text{ kpc}$ , or 5 effective radii ( $1 R_e = 24''$ ).

The H I velocity field was derived by fitting Gaussians to the spectra at those positions where signal is detected in the total H I image. The resulting velocity map is shown in Figure 2.2. Typical errors on this map are  $5 - 10 \text{ km s}^{-1}$ .

We find a total mass of  $5.5 \times 10^8 M_\odot$  for the H I gas content of the ring, which is in agreement with Kim et al. (1988), if we correct for the difference in assumed distance modulus. The amount and morphology of the H I observed in NGC 2974 are not unusual for early-type galaxies. Oosterloo et al. (2007) have found that between 5 and 10 per cent of early-type galaxies show H I masses well above  $10^9 M_\odot$ , while the fraction of detections increases further for lower H I masses (Morganti et al. 2006). The majority of the H I-rich systems have the neutral hydrogen distributed in disc/ring like structures (often warped) with low surface brightness density and no or little ongoing star formation, as observed in NGC 2974. However, there is a region in the North-East of the H I ring where the surface density is higher, and the gas could be forming stars. Jeong et al. (2007) published UV imaging of NGC 2974, obtained with GALEX. Their images reveal indeed a region of increased starformation in the North-East of the galaxy, as well as a starforming ring at the inner edges of the H I ring.

At least some of the most H I rich structures are the results of major mergers (see e.g. Serra et al. 2006). For the systems with less extreme H I masses, like NGC 2974, the origin of the gas is less clear. Accretion of small companions is a possibility, but smooth, cold accretion from the intergalactic medium (IGM) is an alternative scenario.

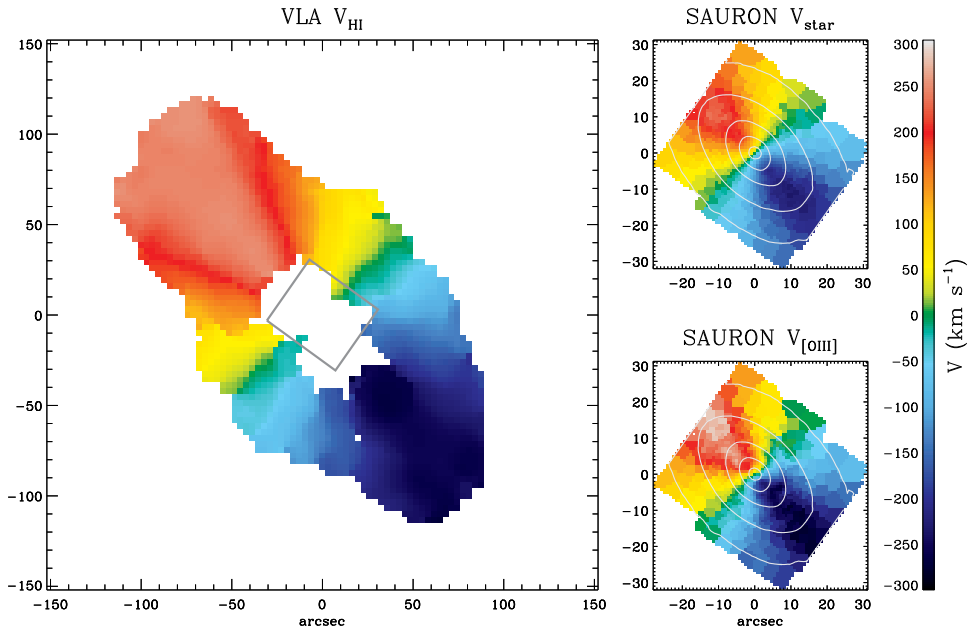


**Figure 2.2** — Velocity maps of the neutral hydrogen (VLA) and ionised gas and stars (SAURON) in NGC 2974. Both the stars and the neutral and ionised gas are well aligned. The maps are orientated so that North is up and East is to the left. The grey box in the VLA map encloses the SAURON fields shown at the right. See colour supplement for a colour version of this figure.

### 2.2.2 SAURON observations

Maps of the stellar and ionised gas kinematics of NGC 2974, obtained with the integral-field spectrograph SAURON, were presented in Emsellem et al. (2004) and Sarzi et al. (2006), respectively, and we refer the reader to these papers for the methods of data reduction and extraction of the kinematics.

In Figure 2.2 we compare both the SAURON velocity maps of stars and [O III] with the velocity map of the H I ring. Stars and gas are well aligned, and the transition between the ionised and the neutral gas seems to be smooth, suggesting that they form one single disc. The twist in the velocity map of the ionised gas in the inner  $4''$  is likely caused by the inner bar of this galaxy (Emsellem et al. 2003; Krajnović et al. 2005).

## 2.3 Analysis of velocity fields

We used kinemetry (Krajnović et al. 2006) to analyse the SAURON and VLA velocity maps. In our application to a gas disc, kinemetry reduces to the tilted-ring method (Begeman 1978). The velocity along each elliptical ring is expanded in Fourier components (e.g. Franx et al. 1994; Schoenmakers, Franx & de Zeeuw 1997):

$$V_{\text{los}}(R, \phi) = V_{\text{sys}}(R) + \sum_{n=1}^N c_n(R) \cos n\phi + s_n(R) \sin n\phi, \quad (2.1)$$

where  $V_{\text{los}}$  is the observed velocity,  $R$  is the length of the semimajor axis of the elliptical ring,  $\phi$  the azimuthal angle, measured from the projected major axis of the galaxy,  $V_{\text{sys}}$  the systemic velocity of the ring and  $c_n$  and  $s_n$  are the coefficients of the harmonic expansion. The  $c_1$  term relates to the circular velocity  $V_c$  in the disc, so that  $c_1 = V_c \sin i$ , where  $i$  is the inclination of the gas disc. Assuming that motions in the ring are intrinsically circular and that the ring is infinitely thin, the inclination can be inferred from the flattening  $q$  of the fitted ellipse:  $\cos i = q$ .

If a gas disc only displays pure circular motions, all harmonic terms other than  $c_1$  in Equation (2.1) are zero. Noncircular motions, originating from e.g. inflows caused by spiral arms or bars, or a triaxial potential, will cause these terms to deviate from zero. Alternatively, also wrong input parameters of the ring (which are flattening  $q$ , position angle  $\Gamma$  and the coordinates of the centre of the ellipse) will result in specific patterns in these terms, see e.g. van der Kruit & Allen (1978); Schoenmakers et al. (1997) and also Krajnović et al. (2006) for details. Therefore, the flattening and position angle of each ring are determined by minimising  $s_1, s_3$  and  $c_3$  along that ring. The centre is kept constant and is chosen to coincide with the position of maximal flux in the galaxy.

### 2.3.1 Noncircular motions

Figure 2.3 shows the properties of the elliptic rings that were fitted to the SAURON and VLA velocity fields, and Figure 2.4 shows the resulting harmonic terms. The datapoints of the VLA data are separated by approximately one beamsize. Error bars were calculated by constructing 100 Monte Carlo realisations of the velocity fields, where the measurement errors of the maps were taken into account.

Both the position angles and the inclinations of the rings show some variation in the SAURON field, but are very stable in the VLA field. The dashed line in the top two panels of Figure 2.3 indicates the mean value of the position angle and inclination of the H I data, which are  $\Gamma = 47 \pm 1^\circ$  and  $i = 60 \pm 2^\circ$ . Here,  $\Gamma$

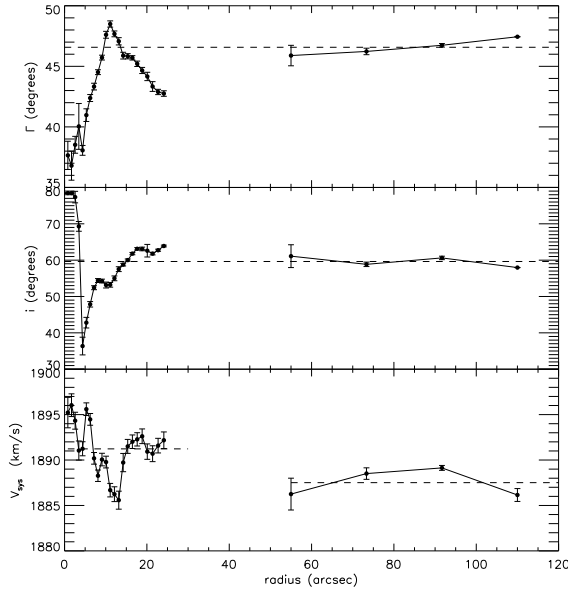


**Figure 2.3** — From top to bottom: position angle  $\Gamma$ , inclination  $i$  and systemic velocity of the rings that are fitted to the SAURON and VLA velocity fields of NGC 2974. The position angle indicates the receding side of the galaxy and is measured North through East. The dashed lines in the top two panels indicate the mean value of  $\Gamma$  and  $i$  generated by the H I rings. The bottom panel has two dashed lines, indicating the mean systemic velocity of the SAURON and VLA rings separately.

is the position angle of the receding side of the galaxy, measured North through East. The systemic velocities (lower panel of Figure 2.3) have been corrected for barycentric motion and are in good agreement. For the SAURON field we find a systemic velocity of  $1891 \pm 3 \text{ km s}^{-1}$ , while for the VLA field we find  $1888 \pm 2 \text{ km s}^{-1}$ . The dashed lines give both these mean velocities. Both the inclination and the systemic velocity that we find are in agreement with previous studies (Cinzano & Van der Marel 1994; Emsellem et al. 2003; Krajnović et al. 2005).

The harmonic terms are shown in Figure 2.4. All terms are normalised with respect to  $c_1$ . From  $c_1$  we see that the velocity curve of the gas rises steeply in the centre, but flattens out at larger radii. This already suggests that a dark halo is present around this galaxy. In §2.4 we will analyse the rotation curve in more detail. The other terms have small amplitudes, and are small compared to  $c_1$  ( $< 4$  per cent). We do not observe signatures that could indicate incorrect ring parameters, as described in Schoenmakers et al. (1997) and Krajnović et al. (2006).



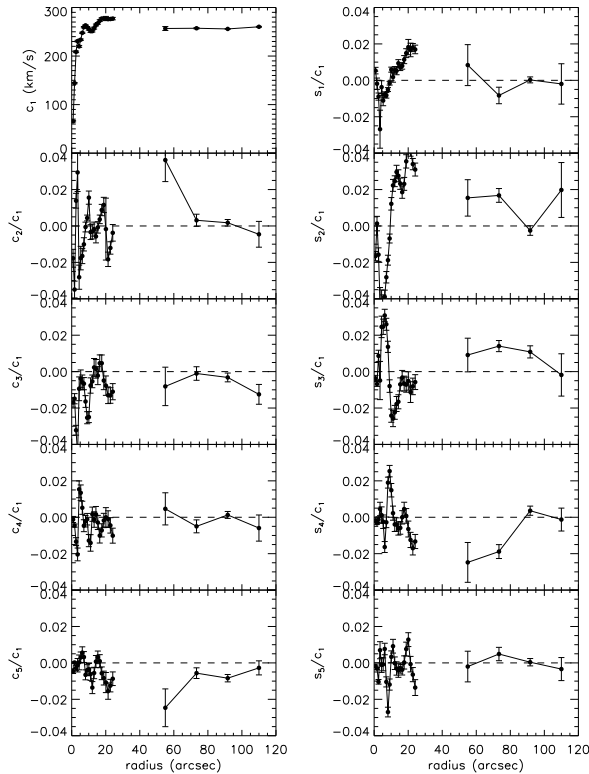


**Figure 2.4** — Coefficients of the harmonic expansion on the SAURON and VLA velocity fields. All except  $c_1$  are normalized with respect to  $c_1$ .

### 2.3.2 Shape of the gravitational potential

Following Schoenmakers et al. (1997), we calculate the elongation of the potential from the harmonic terms. Using epicycle theory these authors showed that an  $\cos m\phi$ -term perturbation of the potential results in signal in the  $m - 1$  and  $m + 1$  coefficients of the harmonic expansion in Equation (2.1).

We assume that the potential of NGC 2974 is affected by an  $m = 2$  perturbation, which could correspond to a perturbation by a bar. We assume that the galaxy is not affected by lopsidedness, warps or spiral arms. To first order, the potential of the galaxy in the plane of the gas ring can then be written as:

$$\Phi(R, \phi) = \Phi_0(R) + \Phi_2(R) \cos 2\phi, \quad (2.2)$$

with  $\Phi_2(R) \ll \Phi_0(R)$ . As explained in Schoenmakers et al. (1997), the elongation of the potential  $\varepsilon_{\text{pot}}$  in the plane of the gas is in this case given by:

$$\varepsilon_{\text{pot}} \sin 2\varphi = \frac{(s_3 - s_1)}{c_1} \frac{(1 + 2q^2 + 5q^4)}{1 - q^4}, \quad (2.3)$$

where  $\varphi$  is one of the viewing angles of the galaxy, namely the angle between the minor axis of the galaxy and the observer, measured in the plane of the disc. This viewing angle is in general unknown, so that from this formula only a lower limit on the elongation can be derived. Schoenmakers (1998) used this method in a statistical way and found an average elongation  $\varepsilon_{\text{pot}} = 0.044$  for a sample of 8 spiral galaxies.

We calculated the elongation at different radii in NGC 2974, and the result is plotted in Figure 2.5. As in Schoenmakers et al, we did not fix  $\Gamma$  and  $q$  when determining the harmonic terms, because an offset in  $\Gamma$  or  $q$  introduces extra signal in  $c_1, s_1$  and  $s_3$ , that would then be attributed to the elongation of the potential.

Although the ionised gas has high random motions (see also § 2.4) and therefore the calculated elongation is probably only approximate, it is striking that the elongation changes sign around  $10''$ . The potential in the inner 10 arcseconds has a rather high elongation  $\varepsilon_{\text{pot}} \sin 2\varphi = 0.10 \pm 0.08$ , while outside this region the elongation as measured from the ionised gas is  $\varepsilon_{\text{pot}} \sin 2\varphi = -0.047 \pm 0.020$ . The change of sign could be the result of the bar system in NGC 2974, with the direction along which the potential is elongated changing perpendiculary. It is worth mentioning here that Krajnović et al. (2005) find a ring in the [O III] equivalent width map, with a radius of  $9''$ . Their data suggest also the presence of a (pseudo-)ring around  $28''$ , and Jeong et al. (2007) find a ring with a radius of  $\sim 60''$  in their GALEX UV map, which is where our H I starts. Assuming that these three rings are resonances of a single bar, Jeong et al. (2007) deduce a pattern speed of  $78 \pm 6 \text{ km s}^{-1} \text{ kpc}^{-1}$ . In addition to the large scale bar, Emsellem et al. (2003) postulate a small nuclear bar ( $\sim 3''$ ).

The H I gas is more suitable for measuring the elongation of the potential, since the cold gas has a small velocity dispersion (typical values  $< 10 \text{ km s}^{-1}$ ) and is on nearly circular orbits. Taking the mean value of the elongation as obtained from the H I field, we find  $\varepsilon_{\text{pot}} \sin 2\varphi = 0.016 \pm 0.022$ . We conclude that the potential of NGC 2974 is well approximated by an axisymmetric one.

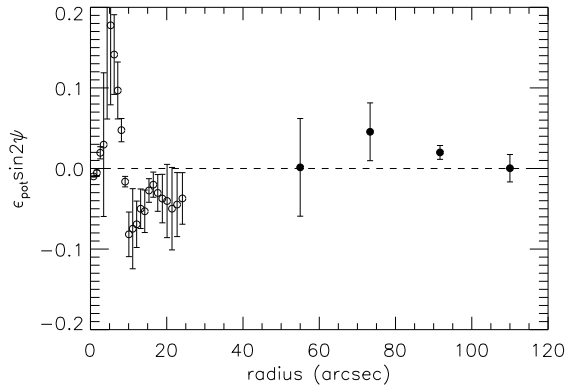


**Figure 2.5** — Elongation of the potential ( $\epsilon_{\text{pot}} \sin 2\psi$ ) of NGC 2974 as a function of radius. Open dots denote measurements from the ionised gas, filled dots represent the H I gas. The elongation as measured from the ionised gas is varying, due to the bar and high random motions of the gas. The cold neutral gas yields a more reliable value for the elongation, and shows that the potential is consistent with axisymmetry.

## 2.4 Rotation curve

To find the rotation curve of NGC 2974, we subtract the systemic velocities from the ionised and neutral gas velocity fields separately. Next, we fix  $\Gamma = 47^\circ$  and  $q = 0.50$  (or equivalently  $i = 60^\circ$ ) of the ellipses to the mean values obtained from the neutral gas, and rerun kinemetry on both the velocity maps, now forcing the position angle and flattening to be the same everywhere in the gas disc. Also, because velocity is an odd moment, the even terms in the harmonic expansion should be zero, and are not taken into account during the fit (see Krajnović et al. 2006). The rotation curve of the ionised gas is shown in Figure 2.6 (open diamonds).

The ionised gas has a high observed velocity dispersion  $\sigma_{\text{obs}}$ , exceeding  $250 \text{ km s}^{-1}$  in the centre of the galaxy. Three phenomena can contribute to the observed velocity dispersion of a gas: thermal motions, turbulence and gravitational interactions:

$$\sigma_{\text{obs}}^2 = \sigma_{\text{thermal}}^2 + \sigma_{\text{turb}}^2 + \sigma_{\text{grav}}^2. \quad (2.4)$$

The thermal velocity dispersion is always present, and caused by the thermal energy of the gas molecules:

$$\sigma_{\text{thermal}}^2 = \frac{kT}{m}, \quad (2.5)$$

where  $k$  is Boltzmann's constant,  $T$  the temperature of the gas and  $m$  the typical mass of a gas particle. The contribution of  $\sigma_{\text{thermal}}$  to the total velocity distribution in ionised gas is small: a typical temperature for ionised gas is  $10^4$  K, which implies  $\sigma_{\text{thermal}} \sim 10$  km/s.

Turbulence can be caused by e.g. internal motions within the gas clouds or shocks induced by a non-axisymmetric perturbation to the potential, such as a bar. This increases the dispersion, but has a negligible effect on the circular velocity of the gas. In contrast, gravitational interactions of individual gas clouds not only increase random motions of the clouds and therefore their dispersion, but also lower the observed velocity. To correct for this last effect, we need to apply an asymmetric drift correction to recover the true circular velocity.

Unfortunately, it is not possible *a priori* to determine which fraction of the high velocity dispersion in the ionised gas is caused by turbulence and which by gravitational interactions. We therefore now first investigate the effect of asymmetric drift on the rotation curve of the ionised gas.

### 2.4.1 Asymmetric drift correction

Due to gravitational interactions of gas clouds on circular orbits, the observed velocity is lower than the circular velocity connected to the gravitational potential. Since we are interested in the mass distribution of NGC 2974, we need to trace the potential, and therefore we have to increase our observed velocity with an asymmetric drift correction, to obtain the true circular velocity. We follow the formalism described in Appendix 2.7, which is based on the Jeans equations and the higher order velocity moments of the collisionless Boltzmann equation.

We assume that the galaxy is axisymmetric, which is a valid approach given the low elongation of the potential that we derived in section 2.3.2. Further we assume that the gas lies in a thin disc.

We fit the prescription that Evans & de Zeeuw (1994) used for their power-law models to the rotation curve extracted from the ionised gas,

$$v_{\text{mod}} = \frac{V_{\infty} R}{R_{\text{mod}}}, \quad (2.6)$$

where  $V_{\infty}$  is the rotation velocity at large radii, and we introduce

$$R_{\text{mod}}^2 = R^2 + R_c^2, \quad (2.7)$$

with  $R_c$  the core radius of the model. This is Equation (2.36) (Appendix 2.7) evaluated in the plane of the disc ( $z = 0$ ), with a flat rotation curve at large radii

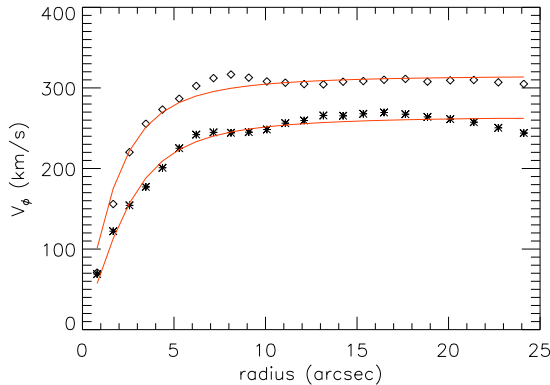


**Figure 2.6** — Rotation curves of the ionised gas (open diamonds) and stars (stars), together with their best fit power-law models (red curves). The rotation curves have been extracted from the SAURON velocity fields.

( $\beta = 0$ ). Since we observe the gas only in the equatorial plane of the galaxy, we cannot constrain the flattening of the potential  $q_\Phi$ . We therefore assumed a spherical potential  $q_\Phi = 1$ , which is not a bad approximation even if the density distribution is flattened, since the dependence on  $q_\Phi$  is weak. Moreover, even though the density distribution of most galaxies is clearly flattened, the potential is in general significantly rounder than the density. For example, an axisymmetric logarithmic potential is only about a third as flattened as the corresponding density distribution (e.g. §2.3.2 of Binney & Tremaine 2008).

To be able to fit the observed velocity we need to convolve our model with the point-spread function (PSF) of the observations, and take the binning into account that results from the finite pixel size of the CCD. We therefore constructed a two-dimensional velocity field of the extracted rotation curve, such that

$$V(R, \phi) = v_{\text{mod}} \cos \phi \sin i, \quad (2.8)$$

and we convolved this field with a kernel as described in the appendix of Qian et al. (1995). This kernel takes into account the blurring caused by the atmosphere and the instrument (FWHM =  $1.4''$ , for the SAURON observations of NGC 2974, see Emsellem et al. 2004) and the spatial resolution of the reduced observations ( $0.8''$  for SAURON). We extracted the velocity along the major axis of the convolved velocity model and used the resulting rotation curve to fit our observations. The best fit is shown in Figure 2.6, and has a core radius  $R_c = 2.1''$  ( $\sim 0.2$  kpc).

Under the assumptions of Equation (2.6), the asymmetric drift correction of

Equation (2.39) reduces to

$$V_c^2 = \overline{v_\phi}^2 - \sigma_R^2 \left[ \frac{\partial \ln \Sigma}{\partial \ln R} + \frac{\partial \ln \sigma_R^2}{\partial \ln R} + \frac{R^2}{2R_{\text{mod}}^2} + \frac{\kappa R^2}{\kappa(2R_{\text{mod}}^2 - R^2) + R^2} \right], \quad (2.9)$$

where  $\overline{v_\phi}$  is the observed velocity,  $\Sigma$  is the surface brightness of the ionised gas and  $\sigma_R$  the radial dispersion of the gas. The last two terms in the equation are connected to the shape of the velocity ellipsoid, with  $\kappa$  indicating the alignment of the ellipsoid, see Appendix 2.7.

To determine the slope of the surface brightness profile, we run kinemetry on the [O III] flux map, extracting the surface brightness along ellipses with the same position angle and flattening as the ones used to describe the velocity field. To decrease the noise we fit a double exponential function to the profile,

$$\Sigma(R) = \Sigma_0 e^{-R/R_0} + \Sigma_1 e^{-R/R_1}, \quad (2.10)$$

and determine the slope needed for the asymmetric drift correction from this parametrisation. The observed surface brightness profile and its fit are shown in Figure 2.7. As with the velocity profile, we convolved our model of the surface brightness during the fit with the kernel of Qian et al. (1995) to take seeing and sampling into account.

$\sigma_R$  can be obtained from the observed velocity dispersion  $\sigma$  using Equation (2.35) of Appendix 2.7. Along the major axis, and under the assumptions made above, this expression simplifies to

$$\sigma_{\text{obs}}^2 = \sigma_R^2 \left[ 1 - \frac{R^2 \sin^2 i}{2R_{\text{mod}}^2} - \frac{R^2 \cos^2 i}{\kappa R_{\text{mod}}^2 (2 - R^2/R_{\text{mod}}^2) + R^2} \right], \quad (2.11)$$

with  $R_{\text{mod}}$  defined in Equation (2.7), and adopting  $R_c = 2.1''$  from the velocity profile.

We choose  $\kappa = 0.5$ , which is a typical value for a disc galaxy (e.g. Kent & de Zeeuw 1991), but we also experimented with other values for this parameter. Varying  $\kappa$  between 0 and 1 resulted in differences in  $V_c$  of approximately 10  $\text{kms}^{-1}$ , and we adopt this value into the error bars of our final rotation curve.

To obtain the slope of  $\sigma_R$  we follow the same procedure as for the surface brightness, extracting the profile of  $\sigma_{\text{obs}}$  from the velocity dispersion map with kinemetry. We assume for the moment that turbulence is negligible in the galaxy

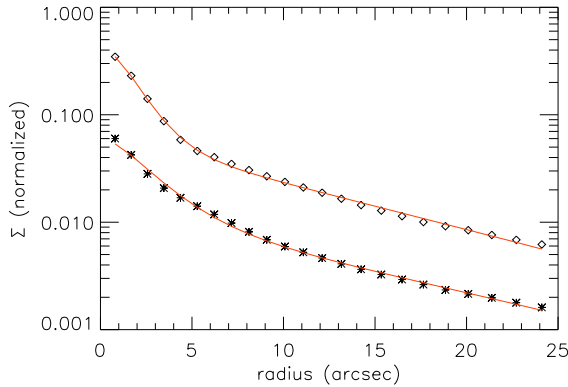


**Figure 2.7** — Profile and fit to the surface brightness of the ionised gas (diamonds) and to the stars (stars). Both profiles have been normalized, and the profile of the stellar surface brightness has been offset by a factor of 10, to distinguish it from the gaseous one.

( $\sigma_{\text{turb}} = 0$ ) and subtract quadratically  $\sigma_{\text{thermal}} = 10 \text{ km s}^{-1}$  from  $\sigma_{\text{obs}}$ . We convert the resulting  $\sigma_{\text{obs}} = \sigma_{\text{grav}}$  into  $\sigma_R$  using the relation in Equation (2.11). We parametrise this profile by

$$\sigma_R(R) = \sigma_0 + \sigma_1 e^{-R_{\text{mod}}/R_1}. \quad (2.12)$$

This profile has a core in the centre (introduced by  $R_{\text{mod}}$ ), so that we can better reproduce the flattening of the profile towards the centre. Again, we convolved our model to take seeing and sampling into account during the fit. The top panel of Figure 2.8 shows the resulting profile and fit, as well as the observed velocity dispersion.

We first assume that turbulence plays no role in this galaxy, and we use  $\sigma_R$  as computed above to calculate the asymmetric drift correction (Equation 2.9). The resulting rotation curve, as well as the observed rotation curve of the ionised gas, is shown in the top panel of Figure 2.9.

To check our asymmetric drift corrected rotation curve of the ionised gas, we compare it with the asymmetric drift corrected stellar rotation curve. Stars do not feel turbulence and are not influenced by thermal motions like the gas, and therefore their observed velocity dispersion contains only contributions of gravitational interactions:  $\sigma_{\text{obs}} = \sigma_{\text{grav}}$ . If we are correct with our assumption that turbulence does not play a role in the ionised gas, then the stellar corrected rotation curve should overlap with the corrected curve of the gas. If it does not, then we know that we should not have neglected the turbulence.

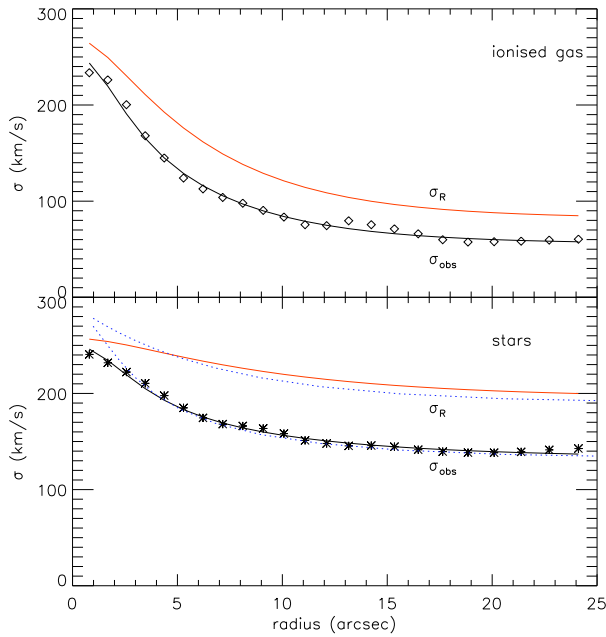


**Figure 2.8** — Top panel: observed velocity dispersion  $\sigma_{\text{obs}}$  of the ionised gas (black diamond) with its best fit (black line). The grey line denotes the radial dispersion  $\sigma_R$ , calculated from the fit to  $\sigma_{\text{obs}}$ . Bottom panel: same as above, but now for the stellar observed velocity dispersion (black stars). The dotted lines represent  $\sigma_R$  and  $\sigma_{\text{obs}}$  as extracted from the Schwarzschild model of Krajnović et al. (2005).

To derive the asymmetric drift correction of the stars, we obtain the observed rotation curve, surface density and velocity dispersion of the stars from our SAURON observations with kinemetry, and parametrise them in the same way as we did for the ionised gas (see Figures 2.6 - 2.8 for the observed profiles and their models). The models were convolved during the fitting as described for the ionised gas. Because for the stars  $\sigma_{\text{obs}} = \sigma_{\text{grav}}$  we do not need to subtract  $\sigma_{\text{thermal}}$  as we did for the ionised gas and hence can calculate  $\sigma_R$  directly from Equation (2.11), where we inserted a core radius  $R_c = 3.0''$  from the stellar velocity model.

In the above, we assumed that the stars lie in a thin disc, which is not the case in NGC 2974. To check the validity of our thin disc approximation for our model of  $\sigma_R$ , we extract this quantity from the Schwarzschild model of Krajnović et al. (2005), for  $\theta = 84^\circ$ , close to the  $z = 0$  plane. The resulting profile is smoothed and shown as the upper dotted blue line in Figure 2.8. It is not a fit to the data, but derived independently from the Schwarzschild model, and agrees very well with



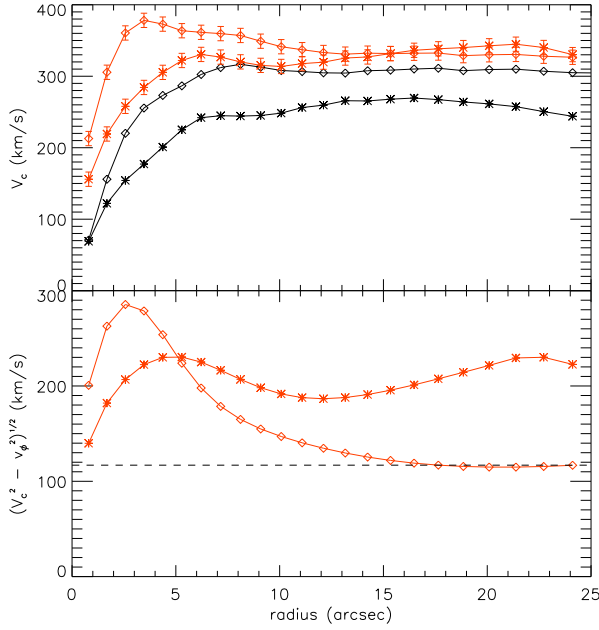


**Figure 2.9** — Top panel: observed rotation curve of the ionised gas (black diamonds) and stars (black stars) with their asymmetric drift corrected curve (grey diamonds and stars, the lower two curves). The correction to the ionised gas seems too high in the central part of the galaxy, when compared to the corrected stellar rotation curve. Bottom panel: asymmetric drift correction  $(V_c^2 - v_\phi^2)^{1/2}$  of the ionised gas (diamonds) and the stars (stars). The dashed line denotes the mean asymmetric drift correction of the ionised gas outside 15 arcseconds.

the stellar  $\sigma_R$  we got from kinemetry. Also,  $\sigma_{\text{obs}}$  derived from the Schwarzschild model (lower dotted blue line) agrees with the results from kinemetry, giving us confidence that our stellar  $\sigma_R$  is reliable.

When we compare the asymmetric drift corrected rotation curves of the ionised gas and of the stars in Figure 2.9, then it is clear that although for  $R > 15''$  the agreement between the curves is very good, the correction for the gas is too high in the central part of the galaxy. This is an indication that turbulence cannot be neglected here, and needs to be taken into account.

### 2.4.2 Turbulence

For radii larger than  $15''$ , the corrected velocity curve of the ionised gas is in agreement with the stellar corrected velocity curve, and since stellar motions are not influenced by turbulence, we can conclude that in this region turbulence is negligible. The bottom panel of Figure 2.9 shows the asymmetric drift correction

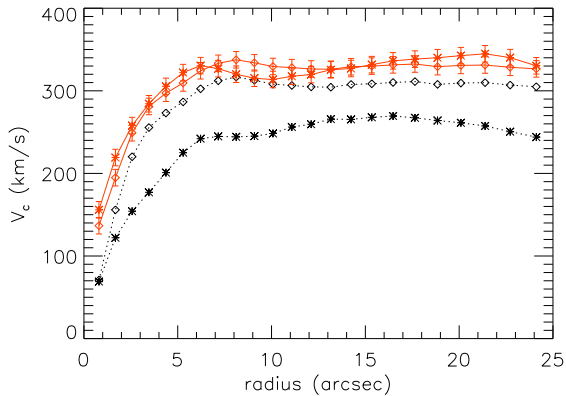


**Figure 2.10** — Asymmetric drift corrected rotation curve of the gas (grey diamonds), removing turbulence as described in the text. The grey stars denote the asymmetric drift corrected rotation curve of the stars. The two curves agree very well, suggesting that our turbulence model is adequate for our purposes. For comparison, also the observed rotation curves of the gas and stars are plotted (dotted lines with black diamonds and stars, respectively).

$(V_c^2 - v_\phi^2)^{1/2}$  itself, and we see that outside  $15''$ , the correction is more or less constant at approximately  $120 \text{ km s}^{-1}$  (dashed line). In order to remove the turbulence from the central region in NGC 2974, we now assume that the asymmetric drift correction has the same value everywhere in the galaxy, namely  $120 \text{ km s}^{-1}$ . We add this value quadratically to the observed rotation curve of the ionised gas, and obtain the rotation curve shown in Figure 2.10. This corrected rotation curve agrees strikingly well with the corrected rotation curve of the stars, and this is a strong indication that our model for turbulence is reasonable, and at least good enough to get a reliable rotation curve for the ionised gas.

We now investigate the random motions resulting from turbulence and gravitational interaction in some more detail. Since we assumed a constant asymmetric drift correction  $(V_c^2 - v_\phi^2)^{1/2}$  of  $\sim 120 \text{ km s}^{-1}$ , we can at each radius calculate the corresponding  $\sigma_R$  with Equation (2.9). Using Equation (2.11) we obtain the observed velocity dispersion, which in this case consists only of  $\sigma_{\text{grav}}$ . Since we know  $\sigma_{\text{obs}}$ , we can subtract quadratically  $\sigma_{\text{grav}}$  and  $\sigma_{\text{thermal}} = 10 \text{ km s}^{-1}$  to obtain  $\sigma_{\text{turb}}$ .

Figure 2.11 shows  $\sigma_{\text{obs}}$  (deconvolved model) and its components  $\sigma_{\text{thermal}}$ ,  $\sigma_{\text{grav}}$  and  $\sigma_{\text{turb}}$ . We fitted a single exponential function (Equation 2.10) with  $R_c = 2.1''$  to the inner 15 arcseconds of  $\sigma_{\text{turb}}$  and find that with this parametrisation we can get a decent fit. We find a lengthscale of  $5.0''$  for the turbulence. The fit is also

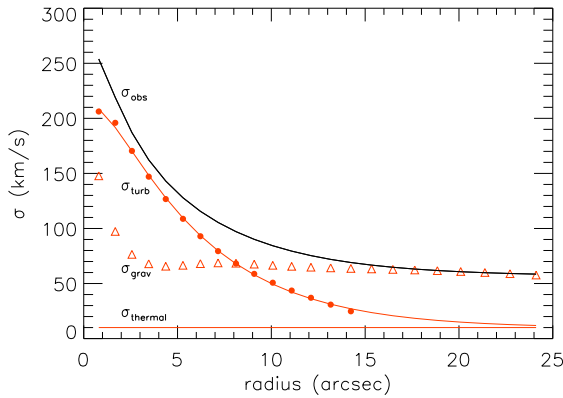


**Figure 2.11** — Observed deconvolved velocity dispersion (solid black line), with its components  $\sigma_{\text{thermal}}$  (horizontal line),  $\sigma_{\text{grav}}$  (open triangles) and  $\sigma_{\text{turb}}$  (filled dots). An exponential fit to  $\sigma_{\text{turb}}$  is overplotted.

shown in Figure 2.11.

## 2.5 Mass model and dark matter content

In this section we combine the corrected rotation curve of the ionised gas with the rotation curve of the neutral gas. The rotation curve of NGC 2974 rises quickly to a maximal velocity and then declines to a somewhat lower velocity, after which it flattens out (see e.g. Figure 2.15). Unfortunately, we lack the data to study this decline in more detail, because our H I ring is not filled. The behaviour of our rotation curve is similar to what is seen in other bright galaxies with a concentrated light distribution (Casertano & van Gorkom 1991; Noordermeer et al. 2007). The decline of the rotation curve in such systems could indicate that the mass distribution in the centre is dominated by the visible mass and that the dark halo only takes over at larger radii. In contrast, in galaxies where the light distribution is less concentrated, such as low-luminosity later-type galaxies, the rotation curves does not decline (e.g. Spekkens & Giovanelli 2006; Catinella, Giovanelli & Haynes 2006).

We separately model the contribution of the stars, neutral gas and dark halo to the gravitational potential. Also we derive the total mass-to-light ratio as a function of radius, and obtain a lower limit on the dark matter fraction in NGC 2974.

In our model, we do not take the weak bar system of NGC 2974 into account. Emsellem et al. (2003) find that the perturbation of the gravitational potential

	HST/WFPC2	MDM
Filter Band	F814W	<i>I</i>
Exposure Time (s)	250	1500
Field of View	$32'' \times 32''$	$17.4' \times 17.4'$
Pixel scale (arcsec)	0.0455	0.508
Date of Observation	16 April 1997	26 March 2003

**Table 2.2** — Properties of the space- and ground-based imaging of NGC 2974, used to model the stellar contribution to the potential. The MDM image was constructed of 3 separate exposures, resulting in a total integration time of 1500 s.

caused by the inner bar in their model of this galaxy is less than 2 per cent. Also, we find that the harmonic coefficients that could be influenced by a large scale bar ( $s_1$ ,  $s_3$  and  $c_3$ ) are small compared to the dominant term  $c_1$  ( $< 4$  per cent). We therefore conclude that although the rotation curve probably is affected by the presence of the bar system, this effect is small, and negligible compared to the systematic uncertainties introduced by the asymmetric drift correction. Furthermore, the largest constraints in our models come from the rotation curve at large radii, where we showed that the elongation of the potential is consistent with axisymmetry.

### 2.5.1 Stellar contribution

The contribution of the stellar mass to the gravitational potential and the corresponding circular velocity can be obtained by deprojecting and modelling the surface photometry of the galaxy. We use the Multi-Gaussian Expansion (MGE) method for this purpose, as described in Cappellari (2002).

Krajnović et al. (2005) presented an MGE model of NGC 2974, based upon the PC part of a dust-corrected WFPC2/F814W image and a ground-based *I*-band image obtained at the 1.0m Jacobus Kapteyn Telescope (JKT). This image was however not deep enough to yield an MGE model that is reliable out to  $5 R_e$  or  $120''$ , which is the extent of our rotation curve. We therefore construct another MGE model, replacing the JKT *I*-band image with a deeper one obtained with the 1.3-m McGraw-Hill Telescope at the MDM Observatory (see Table 2.2). This image is badly contaminated by a bright foreground star, so we do not include the upper half of the image in the fit. Since our model is axisymmetric, enough signal remained to get a reliable fit. We also exclude other foreground stars and bleeding from the image. The parameters of the point spread function (PSF) for

the WFPC2 image were taken from Krajnović et al. (2005).

We match the ground-based MDM image to the higher resolution WFPC2 image, and use it to constrain the MGE-fit outside  $15''$ . Outside  $200''$ , the signal of the galaxy dissolves into the background and we stop the fit there. We are therefore confident of our MGE model out to a radius of at least  $120''$ , which is the extent of the observed H I rotation curve. The goodness of fit can be examined as a function of radius in Figure 2.12.

We forced the axial ratios  $q_j$  of the Gaussians to lie in the interval  $[0.58, 0.80]$  (which is the same range as Krajnović et al. (2005) used in their paper), maximising the number of allowed inclinations and staying as close as possible to a model with constant ellipticity, without significantly increasing the  $\chi^2$  of the fit. This resulted in an MGE model consisting of twelve Gaussians, whose parameters can be found in Table 2.3. The parameters of the inner Gaussians agree very well with the ones in Krajnović et al.'s model, which is not surprising as we used the same dust-corrected WFPC image. The outer Gaussians deviate, where their JKT image is replaced by our MDM image.

Figure 2.13 shows the WFPC2 and MDM photometry and the overlaid contours of the MGE model. Also shown is the masked MDM image. The deviations in the WFPC plot between the isophotes and the MGE model around  $10''$  are point-symmetric and therefore probably reminiscent of a spiral structure (e.g. Emsellem et al. 2003). The deviations are however small, and we conclude that the MGE model is a good representation of the galaxy surface brightness.

## 2.5.2 Gas contribution

The contribution of the H I ring to the gravitational potential is small compared to the stars and halo ( $5.5 \times 10^8 M_\odot$ , three orders of magnitude smaller than the stellar mass) but still included in our mass models. We include a factor 1.3 in mass to account for the helium content of the ring. The mass of the ionised gas is estimated at only  $2.2 \times 10^5 M_\odot$  (Sarzi et al. 2006), and therefore can be neglected in our models.

## 2.5.3 Mass-to-light ratio

By comparing the observed rotation curve and the light distribution from the MGE model, we can already calculate the mass-to-light ratio in NGC 2974. The enclosed mass within a certain radius  $r$  in a spherical system follows directly from

$j$	$I_j(L_\odot \text{ pc}^{-2})$	$\sigma_j$ (arcsec)	$q_j$	$L_j(\times 10^9 L_\odot)$
1	187628.	0.0376306	0.580000	0.0099
2	44798.9	0.0923231	0.800000	0.0197
3	25362.4	0.184352	0.800000	0.0445
4	28102.0	0.343100	0.586357	0.1251
5	23066.0	0.607222	0.722855	0.3964
6	9694.88	1.20984	0.774836	0.7089
7	5019.87	3.56754	0.659952	2.7186
8	1743.48	9.23267	0.580000	5.5578
9	329.832	16.9511	0.770081	4.7057
10	111.091	30.5721	0.580000	3.8829
11	96.2559	44.0573	0.717554	8.6440
12	16.7257	103.085	0.800000	9.1678

**Table 2.3** — Parameters of the Gaussians of the MGE model of NGC 2974. From left to right: number of the Gaussian, central intensity, width (standard deviation), axial ratio and total intensity.

the circular velocity:

$$M(< r) = \frac{V_c^2 r}{G}, \quad (2.13)$$

with  $G$  the gravitational constant. Here we assume that the gravitational potential of the total galaxy is spherical symmetric. This is clearly not the case for the neutral gas, which resides in a thin disc. However, the total mass of the gas is three orders of magnitudes smaller than the total mass, and therefore can be neglected. Also, the stars reside in a flattened potential, as can be shown from their MGE model. But since we cannot disentangle the contributions of the stars and the dark matter to the observed rotation velocity *a priori*, we will for the moment assume that also the stellar mass density can be approximated by a spherical distribution.

Since we know the mass within a sphere of radius  $r$ , we also need to calculate the enclosed  $I$ -band luminosity within a sphere. We first obtain the gravitational potential of our MGE model as a function of radius (see appendix A of Cappellari et al. 2002). Here, we take the flattening of the separate Gaussians into account. We subsequently calculate the corresponding circular velocity, with an arbitrary  $M_*/L$ . To find the luminosity enclosed in a sphere we calculate the spherical mass needed to produce this circular velocity with Equation (2.13), and convert this mass back to a luminosity using the same  $M_*/L$  that we used to calculate the velocity curve. This way we have replaced the luminosity within a flattened

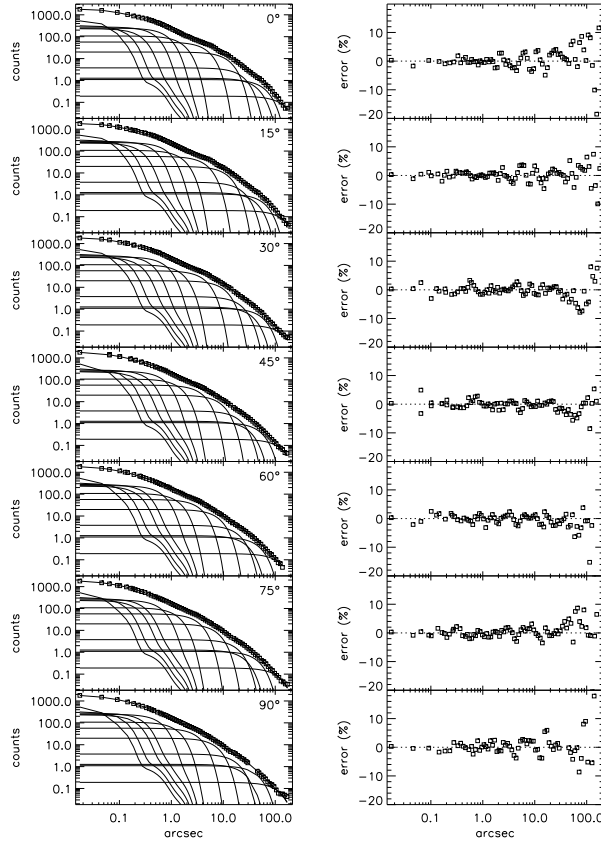


**Figure 2.12** — Left panels: comparison between the WFPC2 and MDM photometry (open squares) and the convolved gaussians composing the MGE model of NGC 2974 (solid line), as a function of radius. Different panels show different angular sectors. Right panels: relative error of the MGE model compared to the data, as a function of radius.

axisymmetric ellipsoid (oblate sphere) by a sphere with radius equal to the long axis of the ellipsoid.

With this method we arrive at a mass-to-light ratio  $M/L_I = 8.5 M_\odot/L_{\odot,I}$  at 5 effective radii ( $1R_e = 24''$ ). In the literature, this value is usually expressed in  $B$ -band luminosities. Using an absolute magnitude of  $M_B = -20.07$  for NGC 2974 (see Table 2.1), we find that  $M/L_B = 14 M_\odot/L_{\odot,B}$ . We checked that  $M_B$  is consistent with our MGE model, adopting a colour  $B - I = 2.13$  for NGC 2974 (see Tonry et al. 2001 and Table 2.1). H I studies of other early-type galaxies yield similar numbers (Morganti et al. 1997 and references therein). For example, Franx et al. (1994) find  $M/L_B = 16 M_\odot/L_{\odot,B}$  at  $6.5 R_e$  using the H I ring around IC 2006,

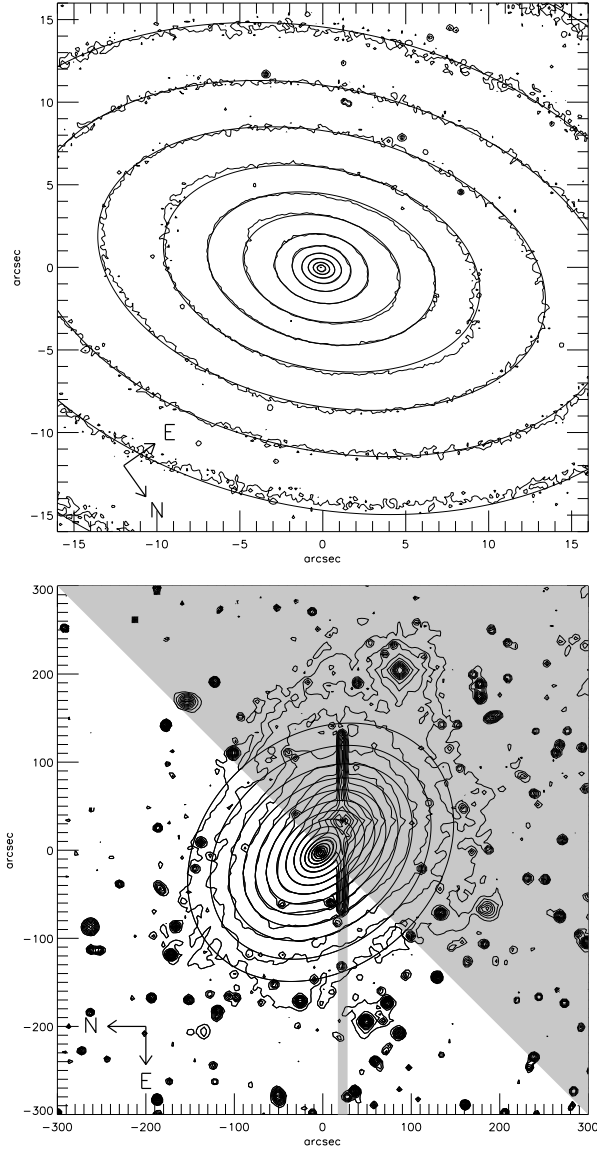


**Figure 2.13** — Contour maps of the *I*-band photometry of NGC 2974. From top to bottom: dust-corrected PC of WFPC2/F814W image and MDM image. The grey area in the MDM image indicates the area that has been excluded from the fit, because of contamination by the bright foreground star. Apart from this area, other foreground stars were also masked during the fit. Overplotted are the contours of the MGE surface brightness model, convolved with the PSF of WFPC2.



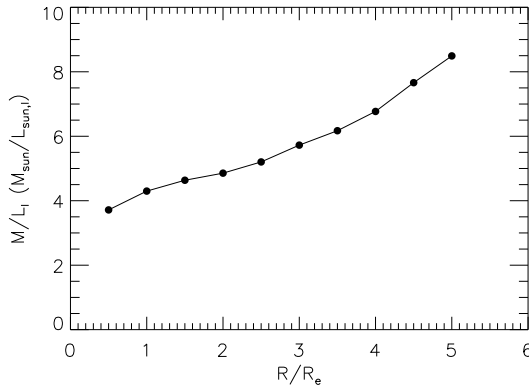


**Figure 2.14** —  $M/L_I$  as a function of radius. The increase of  $M/L_I$  is a strong indication for a dark matter halo around NGC 2974.

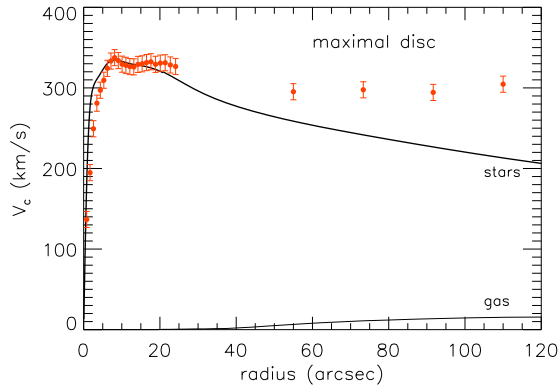
and Oosterloo et al. (2002) report  $M/L_B = 18 M_{\odot}/L_{\odot,B}$  for NGC 3108 at  $6 R_e$ .

Figure 2.14 shows the increase of  $M/L_I$  with radius. We find that within  $1 R_e$ ,  $M/L_I = 4.3 M_{\odot}/L_{\odot,I}$ , which agrees with the results from Schwarzschild modeling of Krajnović et al. (2005) and Cappellari et al. (2006). The increase of  $M/L$  indicates that the fraction of dark matter grows towards larger radii.

#### 2.5.4 Dark matter fraction

To calculate the dark matter fraction, we need to know the stellar mass-to-light ratio  $M_*/L$ . An upper limit on  $M_*/L_I$  can be derived by constructing a maximal disc model. From the MGE model we calculate a rotation curve (taking the flattening of the potential into account, as in Cappellari et al. 2002), and we increase  $M_*/L_I$  until the calculated curve exceeds the observed rotation curve. This way, we find that  $M_*/L_I$  cannot be larger than  $3.8 M_{\odot}/L_{\odot,I}$ . We plotted the rotation curve of the maximal disc model, together with the observed rotation curve in Figure 2.15. The rotation curve of the model has been convolved to take seeing and the resolution of the observations into account, as described in § 2.4.1. The contribution of the neutral gas to the gravitational potential has been included in the model, but has only a negligible effect on the fit.

It is clear that even in the maximal disc model, a dark matter halo is needed to explain the flat rotation curve of the H I gas at large radii. From this model, we can calculate a lower limit to the dark matter fraction in NGC 2974. We then find that within one  $R_e$ , 12 per cent of the total mass is dark, while within  $5 R_e$ , this



**Figure 2.15** — Best fit of a maximal disc model to the observed rotation curve. Grey points indicate the observations and the thick black curve is the fit to these datapoints. This curve is calculated from the combined stellar and gaseous mass, and convolved with a kernel that takes seeing and sampling into account. The stellar mass-to-light ratio in this model is  $3.8 M_{\odot}/L_{\odot,I}$ .

fraction has grown to 55 per cent.

There is however no reason to assume that the stellar mass-to-light ratio is well represented by its maximal allowed value. Cappellari et al. (2006) find  $M_*/L_I = 2.34 M_{\odot}/L_{\odot,I}$  for NGC 2974, measured from line-strength values using single stellar population models. The formal error that they report on this mass-to-light ratio is  $\sim 10$  per cent, but they warn that this value is strongly assumption dependent. Secondary star formation in a galaxy can result in an underestimation of  $M_*/L$ , and the GALEX observations of Jeong et al. (2007) indeed show evidence for recent star formation in NGC 2974. The population models of Cappellari et al. (2006) are based on a Kroupa initial mass function (IMF), but if instead a Salpeter IMF is used, their  $M_*/L_I$  values increase by  $\sim 40$  per cent, which for NGC 2974 would result in  $M_*/L_I = 3.3 M_{\odot}/L_{\odot,I}$ . Cappellari et al. (2006) discard the Salpeter IMF based models, because for a large part of their sample their models then have  $M_*/L_I > M_{\text{tot}}/L_I$ , which is unphysical.

If we adopt  $M_*/L_I = 2.34 M_{\odot}/L_{\odot,I}$  from the stellar population models, then 46 per cent of the total mass within  $1 R_e$  is dark. The dark matter fraction increases to 72 per cent within  $5 R_e$ . See Figure 2.16 for the change in dark matter fraction as a function of radius, and the comparison with the lower limits derived above.

Gerhard et al. (2001) and Cappellari et al. (2006) find an average dark matter fraction of  $\sim 30$  per cent within one effective radius in early-type galaxies, but we note that NGC 2974 is an outlier in the sample of Cappellari et al. The value

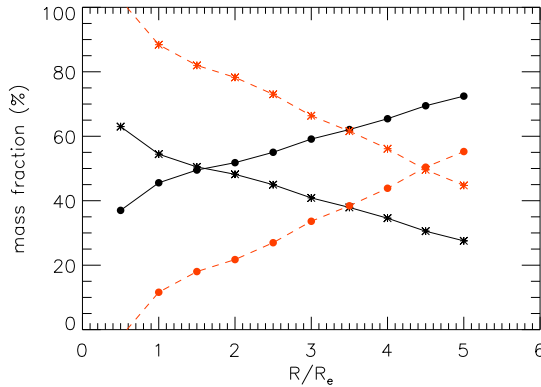


**Figure 2.16** — Dark matter fraction (filled dots) and stellar mass fraction (stars). The black solid lines assume a stellar  $M/L_I$  of  $2.34 M_\odot/L_{\odot,I}$  as predicted by single stellar population models of NGC 2974. The grey dashed lines provide lower and upper limits for the dark matter and stellar mass fraction, respectively, and are based on  $M_*/L_I = 3.8 M_\odot/L_{\odot,I}$ , from the maximal disc model.

of 47 per cent that we find is a bit high compared to this average, though the minimal fraction of dark matter is 14 per cent in our galaxy. Without an accurate determination of  $M_*/L$  we can not give a more precise estimate on the dark matter fraction in NGC 2974.

### 2.5.5 Halo models

We now include a dark halo in our model, to explain the flat rotation curve that we extracted from the H I ring. We explore two different halo models: the pseudo-isothermal sphere and the NFW profile.

The pseudo-isothermal sphere has a density profile given by:

$$\rho(r) = \frac{\rho_0}{1 + (r/r_c)^2}, \quad (2.14)$$

where  $\rho_0$  is the central density of the sphere, and  $r_c$  is the core radius.

The velocity curve resulting from the density profile of the pseudo-isothermal sphere is straightforward to derive analytically, and given by

$$V_c^2(r) = 4\pi G \rho_0 r_c^2 \left( 1 - \frac{r_c}{r} \arctan \frac{r}{r_c} \right). \quad (2.15)$$

The NFW profile was introduced by Navarro et al. (1996) to describe the haloes resulting from simulations, taking a cold dark matter cosmology into ac-

count. This profile has a central cusp, in contrast to the pseudo-isothermal sphere which is core-dominated. Its density profile is given by

$$\rho(r) = \frac{\rho_s}{r/r_s(1+r/r_s)^2}, \quad (2.16)$$

with  $\rho_s$  the characteristic density of the halo and  $r_s$  a characteristic radius. The velocity curve of the NFW halo is given by

$$V_c^2(r) = V_{200}^2 \frac{\ln(1+cx) - cx/(1+cx)}{x[\ln(1+cx) - c/(1+c)]}, \quad (2.17)$$

where  $x = r/r_{200}$  and  $c$  the concentration parameter defined by  $c = r_{200}/r_s$ .  $r_{200}$  is defined such that within this radius the mean density is 200 times the critical density  $\rho_{\text{crit}}$ , and  $V_{200}$  is the circular velocity at that radius. These parameters depend on the assumed cosmology.

We construct mass models of NGC 2974 including a dark matter halo with the observed stellar and gaseous mass. We then calculate the circular velocity resulting from our models, by adding the circular velocities resulting from the separate components:

$$V_c^2(r) = V_{c,\text{halo}}^2 + V_{c,\text{stars}}^2 + V_{c,\text{gas}}^2, \quad (2.18)$$

and fit these to our observed rotation curve. The inner  $25''$  of our model rotation curve, which are based on the SAURON ionised gas measurements, are convolved with a kernel to take seeing and sampling into account, as described in § 2.4.1.

For both profiles, we found that we could not constrain the stellar mass-to-light ratio in our models because of degeneracies: for each  $M_*/L_I$  below the maximal disc value of  $3.8 M_\odot/L_{\odot,I}$  we could get a decent fit. We therefore show two fits for each model, with  $M_*/L$  values that are justified by either linestrength measurements and single stellar population models ( $M_*/L_I = 2.34 M_\odot/L_{\odot,I}$ ) or the observed rotation curve itself ( $M_*/L_I = 3.8 M_\odot/L_{\odot,I}$ ). This last case would be a model requiring a minimal halo.

The best fit models for a dark halo described by a pseudo-isothermal sphere is shown in Figure 2.17. The model in the top panel has a fixed  $M_*/L_I = 2.34 M_\odot/L_{\odot,I}$ , while the bottom panel shows the model with  $M_*/L_I = 3.8 M_\odot/L_{\odot,I}$ . The first model fits the SAURON measurement of the rotation curve well, but has a small slope at the outer part, where the observations show a flat rotation curve. Nevertheless, this model provides a good fit, with a minimal  $\chi^2 = 27$  for  $27 - 2 = 25$  degrees of freedom. We find for this model  $\rho_0 = 19 M_\odot \text{pc}^{-3}$  and core radius  $r_c = 2.3'' = 0.23 \text{ kpc}$ . The second model with  $M_*/L_I = 3.8 M_\odot/L_{\odot,I}$

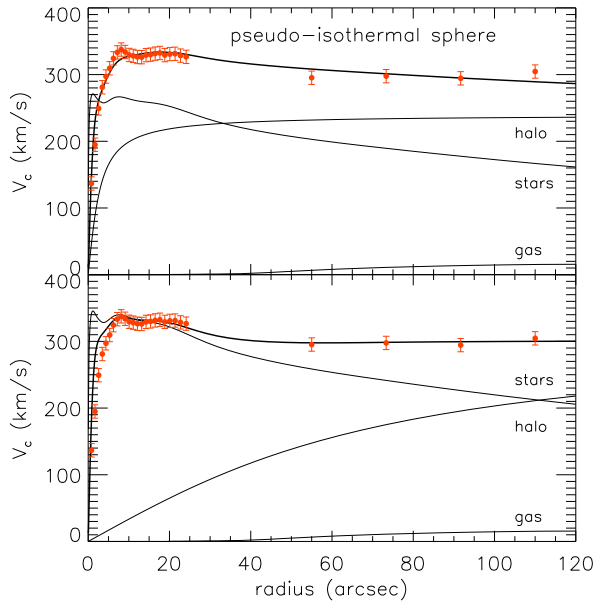


**Figure 2.17** — Best fit models of a dark halo represented by a pseudo-isothermal sphere. The top panel has a stellar  $M_*/L_I$  of  $2.34 M_\odot/L_{\odot,I}$  from stellar population models, and the bottom panel has  $M_*/L_I = 3.8 M_\odot/L_{\odot,I}$  from the maximal disc model. The grey dots are our observations from the ionised gas (asymmetric drift corrected) and H I gas. The rotation curves resulting from the potentials of the halo, stars and gas are plotted separately, where the first two are unconvolved. The bold line denotes the fit to the data, and is the convolved rotation curve resulting from the combined potential of halo, stars and gas.

provides a better fit to the H I measurements, but has problems fitting the central part of the rotation curve. The model has a lower central density  $\rho_0 = 0.06 M_\odot \text{pc}^{-3}$  and larger core radius  $r_c = 54'' = 5.4 \text{ kpc}$ . The fit is worse than for the previous model, with  $\chi^2 = 133$ .

Figure 2.18 shows the best fitting-models with an NFW dark halo. This model fits the data less well than the pseudo-isothermal sphere: for the model with  $M_*/L_I = 2.34 M_\odot/L_{\odot,I}$  (top panel) we find a minimal  $\chi^2 = 44$  for  $27 - 2$  degrees of freedom. The corresponding parameters of the density function are  $\rho_s = 1.1 M_\odot \text{pc}^{-3}$  and  $r_s = 21'' = 2.1 \text{ kpc}$ . For  $M_*/L_I = 3.8 M_\odot/L_{\odot,I}$  the fit is worse ( $\chi^2 = 144$ ) but the outer part of the rotation curve is better fitted. We find  $\rho_s = 1.1 \times 10^{-3} M_\odot \text{pc}^{-3}$  and  $r_s \approx 1300''$ , which corresponds to approximately 130 kpc.

Adopting  $H_0 = 73 \text{ km s}^{-1} \text{ Mpc}^{-1}$ , the critical density is given by  $\rho_{\text{crit}} = 3H_0^2/8\pi G = 1.5 \times 10^{-7} M_\odot \text{pc}^{-3}$ . We calculate the concentration parameter  $c$ ,

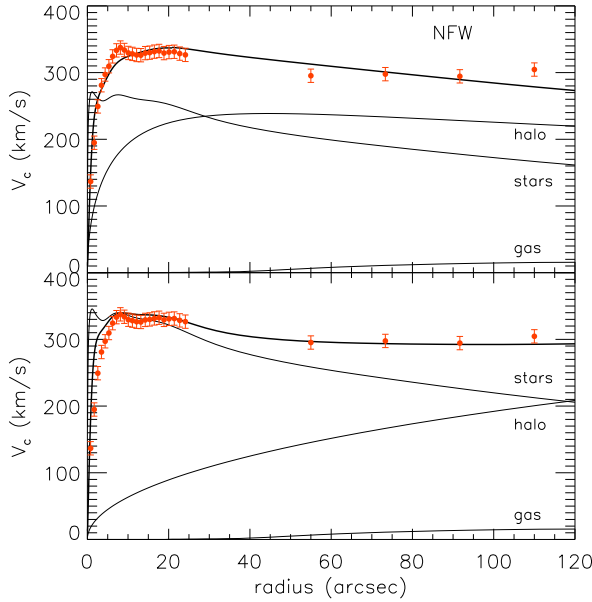


**Figure 2.18** — Same as Figure 2.17, but now with a dark halo contribution given by an NFW profile. The top panel has the stellar  $M_*/L_I$  value from population models ( $2.34 M_\odot/L_{\odot,I}$ ), and the bottom panel from the maximal disc model ( $3.8 M_\odot/L_{\odot,I}$ ).

given that

$$\frac{\rho_s}{\rho_{\text{crit}}} = \frac{200}{3} \frac{c^3}{\ln(1+c) - c/(1+c)}, \quad (2.19)$$

and find  $c = 71$  and  $c = 4.7$  for the NFW profiles in the  $M_*/L_I = 2.34 M_\odot/L_{\odot,I}$  and  $M_*/L_I = 3.8 M_\odot/L_{\odot,I}$  models, respectively. These values are quite deviant from the value that is expected from cosmological simulations ( $c \sim 10$ , Bullock et al. 2001). When fixing  $c = 10$  and fitting again an NFW halo to our observations with  $M_*/L_I$  and the scale radius as free parameters, we arrive at the model shown in Figure 2.19. We find  $M_*/L_I = 3.3 M_\odot/L_{\odot,I}$  and  $r_s \approx 380'' \approx 38$  kpc, with a minimal  $\chi^2$  value of 87 for  $27 - 2$  degrees of freedom. We regard this model as more realistic than the two other NFW profiles mentioned above, but since also here the fit is not perfect, we cannot conclude that therefore  $M_*/L_I = 3.3 M_\odot/L_{\odot,I}$  is a better estimate for the stellar mass-to-light ratio in NGC 2974, than the value from the stellar population models.

The results of the halo models discussed above are summarized in Table 2.4.

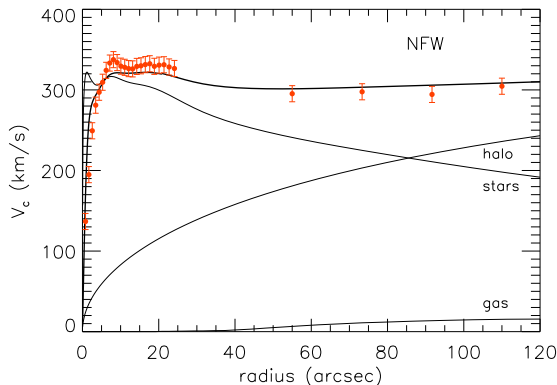


**Figure 2.19** — Best fit model of a dark halo with an NFW profile, with a concentration parameter  $c = 10$  as indicated by cosmological simulation. This model has a stellar  $M/L$  of  $3.3 M_{\odot}/L_{\odot,I}$ . The red dots are the observations, and the black bold line the fit to these observations. The contributions of halo, stars and gas are plotted separately, where the first two curves are unconvolved.

## 2.5.6 MOND

An alternative to including a dark matter halo in a galaxy to explain its rotation curve at large radii, is provided by Modified Newtonian Dynamics (MOND, Milgrom 1983). In this theory, Newtonian dynamics is no longer valid for small accelerations ( $a \ll a_0$ ), but instead the acceleration  $a$  in a gravitational field is given by

$$a\mu(a/a_0) = a_N, \quad (2.20)$$

where  $a_N$  is the Newtonian acceleration and  $\mu$  is an interpolation function, such that  $\mu(x) = 1$  for  $x \gg 1$  and  $\mu(x) = x$  for  $x \ll 1$ . Given the stellar mass-to-light ratio of a galaxy, MOND predicts its rotation curve. An overview of properties and predictions of MOND is offered by Sanders & McGaugh (2002).

We fitted our rotation curve of NGC 2974 with  $M_*/L_I$  as a free parameter. For  $a_0$  we adopted the value of  $1.2 \times 10^{-8} \text{ cm/s}^2$ , which was derived by Begeman, Broeils & Sanders (1991) from a sample of spiral galaxies. The contribution of the neutral gas is included in our model in the same way as described before, as well as a convolution to take seeing and sampling into account.

NGC 2974 is an ideal candidate to study the transition between the Newtonian and MOND regime, since the Newtonian acceleration reaches  $a_0$  at a radius of approximately  $95''$  if we adopt a stellar mass-to-light ratio of  $2.34 M_{\odot}/L_{\odot,I}$ .

Halo profile	$M_*/L_I$ ( $M_\odot/L_{\odot,I}$ )	$\rho_0, \rho_s$ ( $M_\odot \text{ pc}^{-3}$ )	$r_c, r_s$ (kpc)	$c$	$\chi^2$
Pseudo-isothermal	2.34	19	0.23	-	27
	3.8	0.06	5.4	-	133
NFW	2.34	1.1	2.1	71	44
	3.8	0.0011	130	4.7	144
	3.3	0.0067	38	10	87

**Table 2.4** — Comparison of the best fit models with a dark matter halo, as described in the text.

For larger  $M_*/L_I$ , this radius increases, and for the maximum disc value of  $3.8 M_\odot/L_{\odot,I}$ ,  $a_0$  is reached around  $120''$ . This means that a large part of the observed rotation curve lies in the transition region, and we could therefore use NGC 2974 to discriminate between interpolation function.

We first constructed a model with the standard interpolation function of MOND,

$$\mu(x) = \frac{x}{\sqrt{1+x^2}}. \quad (2.21)$$

The resulting fit is shown as model I in Figure 2.20. This model has the same  $M_*/L_I$  value as the maximal disc model,  $3.8 M_\odot/L_{\odot,I}$ , but does clearly not provide a good fit to the data.

We constructed a second model, with an alternative interpolation function explored by Famaey & Binney (2005),

$$\mu(x) = \frac{x}{1+x}. \quad (2.22)$$

This function makes the transition between the Newtonian and the MOND region less abrupt than the standard interpolation function and requires a lower  $M_*/L_I$ . The fit provided by this model to the data is much better (Model II in Figure 2.20), but formally less good than a model with a dark matter halo. This model requires  $M_*/L_I = 3.6 M_\odot/L_{\odot,I}$ , and the fit yields  $\chi^2 = 98$ , for 27-1 degrees of freedom.

Famaey & Binney (2005) find that their simple interpolation function provides better constraints to the terminal velocity of the Milky Way than the standard function. Famaey et al. (2007) fitted the rotation curves of a sample of galaxies with Hubble types ranging from small irregular dwarf galaxies to large early-type spirals, and report that both interpolating functions fit the data equally well. However, Sanders & Noordermeer (2007) find that for their sample of early-type



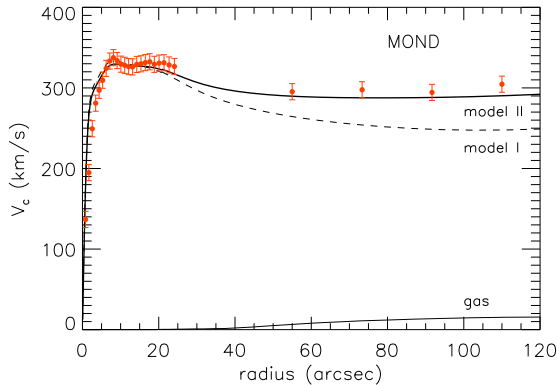


**Figure 2.20** — Observed rotation curve (grey datapoints) and best fitting models with a MOND rotation curve. The dashed line (Model I) is constructed with the standard interpolation function, while the thick line (Model II) uses an alternative simple interpolation function (see text).

disc galaxies the simple interpolation function yields more sensible values for  $M_*/L$  than the standard one.

It would be interesting to see whether there is a preference for the simple interpolation function over the standard one in early-type galaxies. In this scenario, the challenge for MOND would be to provide a universal interpolation function that would fit rotation curves of all galaxy types along the Hubble sequence. So far, mostly spirals and dwarf galaxies have been confronted with MOND, but with more early-type galaxies getting detected in H I and more rotation curves becoming available, the sampling in morphology should become less biased to late-type galaxies.

## 2.6 Summary

We obtained H I observations of the early-type galaxy NGC 2974 and found that the neutral gas resides in a ring. The ring starts around  $50''$ , and extends to  $120''$ , which corresponds to 12 kpc or 5 effective radii. The total mass of the neutral gas is  $5.5 \times 10^8 M_\odot$ .

We compared the velocity field of the H I ring with the kinematics of the ionised gas. We found that both velocity fields are very regular and nicely aligned, indicating that they could form a single disc. A harmonic decomposition of the velocity field showed that at large radii the gravitational potential is consistent with an axisymmetric shape.

We introduced a new way to correct the rotation curve of the ionised gas for asymmetric drift. We found that the correction approaches a constant value and this enabled us to remove the effect of turbulence on the rotation curve, assuming a constant asymmetric drift correction throughout the galaxy. We confirmed that this assumption is valid in NGC 2974, by comparing with the asymmetric drift corrected rotation curve of the stars (which was not affected by turbulence). An interesting question is whether other galaxies show the same behaviour. If this is the case, then with our method we would be able to investigate rotation curves of ionised gas and the effects of turbulence in more detail in other galaxies, and search for connections with e.g. spiral structure and bars. Although in principle we could for NGC 2974 also have used the stellar rotation curve together with the H I to constrain the mass models, this will not be the case for all galaxies. For instance, in low surface brightness galaxies stellar kinematics are not easy to obtain, and even in high surface brightness galaxies, the absorption line kinematics need to be binned to higher signal-to-noise than the emission line kinematics, provided that ionised gas is present.

It is clear from the rotation curve of NGC 2974 that dark matter is required to explain the observed velocities. We found that the total mass-to-light ratio increases from  $4.3 M_{\odot}/L_{\odot,I}$  at  $1 R_e$  to  $8.5 M_{\odot}/L_{\odot,I}$  at  $5 R_e$ . This last value would correspond to  $14 M_{\odot}/L_{\odot,B}$  in *B*-band. Even in the maximal disc model, 55 per cent of the total mass is dark, and an additional dark halo needs to be included.

We constructed mass models of NGC 2974, where we modeled both the stellar and gaseous contribution to the gravitational potential. The latter is negligible compared to the stars ( $M_{\text{gas}} \sim 0.001 M_*$ ), but still included in our models. For the dark halo, we tested two different profiles: the core-dominated pseudo-isothermal sphere and the cuspy NFW profile. We experimented with different values for the stellar mass-to-light ratio, but found that we cannot constrain this value with just the rotation curve: for most  $M_*/L$  smaller than the maximal disc value, we could obtain a decent fit for both the pseudo-isothermal sphere and the NFW profile. If we compare models with  $M_*/L_I$  from single stellar population models ( $2.34 M_{\odot}/L_{\odot,I}$ ) with maximal disc model ( $M_*/L_I = 3.8 M_{\odot}/L_{\odot,I}$ ), then the first provide better fits to the data. Especially the inner datapoints are better reproduced with  $M_*/L_I = 2.34 M_{\odot}/L_{\odot,I}$ , but we note that the H I data points are better fitted in the models with the larger  $M_*/L_I$  value. The pseudo-isothermal sphere fits our data marginally better than the NFW profile, but the difference is not significant. With MOND we can also reproduce the observed rotation curve, but not as well as with models that include a dark matter halo.

The largest uncertainty in our analysis is the stellar mass-to-light ratio. We can

only derive an upper limit on this ratio from the maximal disc model or e.g. from Schwarzschild modeling, since  $M_*/L$  should always be equal to or smaller than the dynamical  $M/L$ . Values for  $M_*/L$  from stellar population synthesis models depend significantly on the model assumptions: we mentioned already that going from a Kroupa to a Salpeter IMF can increase  $M_*/L$  by as much as 40 per cent. Also, even low-level secondary star formation can affect  $M_*/L$  severely. Furthermore, there is no reason why the  $M_*/L$  should remain constant over 5 effective radii, which we assumed when modeling the stellar mass. If the stellar mass-to-light ratio were known, we would be able to determine the dark matter fraction in the galaxy with more accuracy, and either rule out or confirm the maximal disc hypothesis. Also, since  $M_*/L$  is the only free parameter when fitting a rotation curve in MOND, knowing this value would provide us with a rotation curve that can be compared to the data directly, providing a clear test for MOND.

We have shown in this paper that it is possible to combine rotation curves of neutral and ionised gas, correcting the latter one for asymmetric drift using the Jeans equations and the higher order velocity moments of the collisionless Boltzmann equations. Our method to correct for the asymmetric drift therefore does not require a cold disc assumption ( $\sigma \ll V_c$ ). With more early-type galaxies getting detected in H I, and more high quality rotation curves becoming available, we can now study the shape of their dark matter haloes.

## Acknowledgements

The authors would like to thank Martin Bureau, Michele Cappellari, Richard McDermid, Marc Sarzi and Scott Tremaine for useful discussions, and Remco van den Bosch for careful reading of the manuscript. We also are grateful to Jesús Falcón-Barroso for making available the MDM image of NGC 2974 prior to publication.

This research was supported by the Netherlands Research School for Astronomy NOVA, and by the Netherlands Organization of Scientific Research (NWO) through grant 614.000.426 (to AW). AW acknowledges The Leids Kerkhoven-Bosscha Fonds for contributing to working visits. GvdV acknowledges support provided by NASA through Hubble Fellowship grant HST-HF-01202.01-A awarded by the Space Telescope Science Institute, which is operated by the Association of Universities for Research in Astronomy, Inc., for NASA, under contract NAS 5-26555.

The Very Large Array is part of the National Radio Astronomy Observatory, which is a facility of the National Science Foundation operated under cooperative

agreement by Associated Universities, Inc. The SAURON observations were obtained at the William Herschel Telescope, operated by the Isaac Newton Group in the Spanish Observatorio del Roque de los Muchachos of the Instituto de Astrofísica de Canarias.

The Digitized Sky Survey was produced at the Space Telescope Science Institute under US Government grant NAG W-2166. Photometric data of NGC 2974 was obtained using the 1.3-m McGraw-Hill Telescope of the MDM Observatory at Kitt Peak. We acknowledge the usage of the HyperLeda data base (<http://leda.univ-lyon1.fr>).

## 2.7 Appendix: Asymmetric drift correction in a thin disc

In this appendix we derive expressions for the asymmetric drift correction in a stationary axisymmetric system, using the velocity moments of the collisionless Boltzmann equation. We then evaluate this expression in a thin disc approximation. Our method does not require that the velocity dispersion should be small compared to the circular velocity ( $\sigma/V_c \ll 1$ ) and is comparable to the “hot disc model”, (see e.g. Häring-Neumayer et al. 2006).

### 2.7.1 The velocity ellipsoid

To derive the asymmetric drift correction we start from the collisionless Boltzmann equation for a stationary axisymmetric galaxy and using cylindrical coordinates  $\vec{r} = (R, \phi, z)$ ,

$$v_R \frac{\partial f}{\partial R} + v_z \frac{\partial f}{\partial z} + \left( \frac{v_\phi^2}{R} - \frac{\partial \Phi}{\partial R} \right) \frac{\partial f}{\partial v_R} - \frac{v_R v_\phi}{R} \frac{\partial f}{\partial v_\phi} - \frac{\partial \Phi}{\partial z} \frac{\partial f}{\partial v_z} = 0, \quad (2.23)$$

with  $f(R, z; v_R, v_\phi, v_z)$  the distribution function,  $\Phi(R, z)$  the underlying potential and  $v(\vec{r})$  the (luminosity) density given by  $\int f(\vec{r}; \vec{v}) d\vec{v}$ . We multiply the above equation by  $v_R$  and subsequently integrate over all velocities. We then obtain the Jeans equation:

$$\frac{\partial(\overline{v v_R^2})}{\partial R} + \frac{\partial(\overline{v v_R v_z})}{\partial z} + \frac{v}{R} \left( \overline{v_R^2} - \overline{v_\phi^2} + R \frac{\partial \Phi}{\partial R} \right) = 0. \quad (2.24)$$

Since our system is axisymmetric, we set  $\partial v / \partial z = 0$  by symmetry. Substituting the circular velocity  $V_c^2 = R(\partial \Phi / \partial R)$ , we arrive at Equation (4-227) of Binney &

Tremaine (2008):

$$V_c^2 = \overline{v_\phi^2} - \sigma_R^2 \left[ \frac{\partial \ln v}{\partial \ln R} + \frac{\partial \ln \sigma_R^2}{\partial \ln R} + 1 - \frac{\sigma_\phi^2}{\sigma_R^2} + \frac{R}{\sigma_R^2} \frac{\partial (\overline{v_R v_z})}{\partial z} \right], \quad (2.25)$$

with  $\sigma_\phi^2 = \overline{v_\phi^2} - \overline{v_\phi}^2$ ,  $\sigma_R^2 = \overline{v_R^2}$  and  $\sigma_z^2 = \overline{v_z^2}$ . The observed velocity field gives  $\overline{v_\phi}$ , and the remaining terms in Equation (2.25) form the asymmetric drift correction.

The last term in the asymmetric drift correction depends on the alignment of the velocity ellipsoid. In case of alignment with the cylindrical coordinate system  $(R, \phi, z)$  we have  $\overline{v_R v_z} = 0$ , while in case of alignment with the spherical coordinate system  $(r, \theta, \phi)$  we have  $\overline{v_R v_z} = (\sigma_R^2 - \sigma_z^2)(z/R)/[1 - (z/R)^2]$ , which becomes proportional to  $z/R$  close to the disc plane. These are two extreme situations, and we introduce the parameter  $\kappa$  to find a compromise:

$$\overline{v_R v_z} = \kappa (\sigma_R^2 - \sigma_z^2) \frac{z/R}{1 - (z/R)^2}, \quad 0 \leq \kappa \leq 1, \quad (2.26)$$

where a typical value for  $\kappa$  is 0.5 for disc galaxies (e.g. Kent & de Zeeuw 1991).

To evaluate the asymmetric drift correction, we need expressions for  $\sigma_\phi/\sigma_R$  and  $\sigma_z/\sigma_R$ . We use higher order velocity moments of the collisionless Boltzmann equation to derive these expressions.

Starting again from Equation (2.23), we multiply by  $v_R v_\phi$  and integrate over all velocities:

$$\frac{\partial (\overline{v v_R^2 v_\phi})}{\partial R} + \frac{\partial (\overline{v v_R v_z v_\phi})}{\partial z} + \frac{v}{R} \left( 2 \overline{v_R^2 v_\phi} - \overline{v_\phi^3} - \overline{v_\phi} R \frac{\partial \Phi}{\partial R} \right) = 0. \quad (2.27)$$

Aligning the velocity ellipsoid in the azimuthal direction we have  $\overline{v_R^2 (v_\phi - \overline{v_\phi})} = 0$  and  $\overline{v_R v_z (v_\phi - \overline{v_\phi})} = 0$ , so that  $\overline{v_R^2 v_\phi} = \sigma_R^2 \overline{v_\phi}$  and  $\overline{v_R v_z v_\phi} = \overline{v_R v_z} \overline{v_\phi}$ . We substitute these relations in Equation (2.27), and subtract  $\overline{v_\phi}$  times the Jeans equation (2.24):

$$v \sigma_R^2 \frac{\partial \overline{v_\phi}}{\partial R} + v \overline{v_R v_z} \frac{\partial \overline{v_\phi}}{\partial z} + \frac{v}{R} \left[ \sigma_R^2 \overline{v_\phi} - (\overline{v_\phi^3} - \overline{v_\phi^2} \overline{v_\phi}) \right] = 0. \quad (2.28)$$

We substitute  $\overline{v_\phi^3} - \overline{v_\phi^2} \overline{v_\phi} = 2 \sigma_\phi^2 \overline{v_\phi} + \overline{(v_\phi - \overline{v_\phi})^3}$  and  $\overline{v_R v_z}$  from Equation(2.26) to arrive at

$$\frac{\sigma_\phi^2}{\sigma_R^2} = \frac{1}{2} \left( 1 + \alpha_R + \kappa \frac{1 - \sigma_z^2/\sigma_R^2}{1 - (z/R)^2} \alpha_z - \frac{\overline{(v_\phi - \overline{v_\phi})^3}}{\sigma_R^2 \overline{v_\phi}} \right), \quad (2.29)$$

where we have introduced the logarithmic slopes

$$\alpha_R = \frac{\partial \ln \bar{v}_\phi}{\partial \ln R}, \quad \text{and} \quad \alpha_z = \frac{\partial \ln \bar{v}_\phi}{\partial \ln z}. \quad (2.30)$$

To obtain an expression for  $\sigma_z/\sigma_R$  we again start with the collisionless Boltzmann equation, but now multiply with  $v_z(v_\phi - \bar{v}_\phi)$  before integrating over all velocities:

$$v \bar{v}_R v_z \frac{z}{R} \left( 1 + \frac{\partial \ln \bar{v}_\phi}{\partial \ln R} \right) + v \sigma_z^2 \frac{\partial \ln \bar{v}_\phi}{\partial \ln z} = 0. \quad (2.31)$$

Substituting Equation (2.26) we find

$$\frac{\sigma_z^2}{\sigma_R^2} = \frac{\kappa z^2 (1 + \alpha_R)}{\kappa z^2 (1 + \alpha_R) - (R^2 - z^2) \alpha_z}, \quad (2.32)$$

The above expressions can be inserted into Equation (2.25) to obtain the asymmetric drift correction and therefore the true circular velocity. In practice, we often apply the asymmetric drift correction in the thin disc approximation, because from observations the  $z$ -dependence is not straightforward to derive.

In the thin disc approximation, we have  $z \ll R$ , and therefore we can write Equation (2.26) as

$$\bar{v}_R v_z = \kappa (\sigma_R^2 - \sigma_z^2) \frac{z}{R}. \quad (2.33)$$

and following the same reasoning as before, we see that the expressions in Equations (2.29) and (2.32) simplify slightly: in the first expression the one-to-last term disappears, and for the second one,  $(R^2 - z^2)$  gets replaced by  $R^2$  in the nominator of the expression. Furthermore, the derivative of  $\bar{v}_R v_z$  simplifies considerably.

We find the following expression for the asymmetric drift correction in the thin disc approximation, after substitution in Equation (2.25):

$$V_c^2 = \bar{v}_\phi^2 - \sigma_R^2 \left[ \frac{\partial \ln v}{\partial \ln R} + \frac{\partial \ln \sigma_R^2}{\partial \ln R} + \frac{1}{2} (1 - \alpha_R) + \frac{1}{2} \frac{(v_\phi - \bar{v}_\phi)^3}{\sigma_R^2 \bar{v}_\phi} - \frac{\kappa R^2 \alpha_z}{\kappa z^2 (1 + \alpha_R) - R^2 \alpha_z} \right]. \quad (2.34)$$

The one-to-last term vanishes in the case of a velocity ellipsoid symmetric around  $v_\phi = \bar{v}_\phi$ . This need not necessarily be the case, and the exact form of  $(v_\phi - \bar{v}_\phi)^3$  depends on the underlying distribution function, which in general cannot be constrained easily (e.g. Kuijken & Tremaine 1991). However, since this term is a factor  $\sigma_R^2$  smaller than the other terms, it can be safely ignored for most purposes.

### 2.7.2 Observables

Here we investigate how in the thin disc approximation we can correct our observed velocity field for asymmetric drift, to obtain the true circular velocity  $V_c$ . This quantity traces the potential and therefore the mass of the galaxy.

In a thin disc, we can replace  $\partial \ln v / \partial \ln R$  by the slope of the surface brightness  $\partial \ln \Sigma / \partial \ln R$ . This slope can be obtained directly from observations.

The observed velocity and velocity dispersion of an axisymmetric thin disc seen under an inclination  $i$  is given by:

$$\begin{aligned} V &= v_{\text{sys}} + \overline{v_\phi} \cos \phi \sin i, \\ \sigma^2 &= \sigma_R^2 \sin^2 \phi \sin^2 i + \sigma_\phi^2 \cos^2 \phi \sin^2 i + \sigma_z^2 \cos^2 i \\ &\quad - \overline{v_R v_z} \sin \phi \sin 2i. \end{aligned} \quad (2.35)$$

It is straightforward to obtain  $\overline{v_\phi}$  from the observed velocity field, and though  $\alpha_R$  can be estimated rather well,  $\alpha_z$  is less easy to constrain. Therefore, we fit to  $\overline{v_\phi}$  the prescription of Evans & de Zeeuw (1994) for power-law models:

$$v_{\text{mod}} \propto \frac{R}{(R_c^2 + R^2 + z^2/q_\Phi^2)^{1/2 + \beta/4}}, \quad (2.36)$$

where  $R_c$  is the core radius,  $q_\Phi$  the flattening of the potential and  $\beta$  the logarithmic slope of the rotation curve at large radii (such that  $\beta = 0$  implies a flat rotation curve).

For the slopes of  $\overline{v_\phi}$  we find that:

$$\begin{aligned} \alpha_R &= 1 - \frac{(1 + \beta/2)R^2}{R_c^2 + R^2 + z^2/q_\Phi^2} \\ \alpha_z &= -\frac{(1 + \beta/2)z^2/q_\Phi^2}{R_c^2 + R^2 + z^2/q_\Phi^2} = -\frac{z^2}{q_\Phi^2 R^2} (1 - \alpha_R), \end{aligned} \quad (2.37)$$

so that with  $\overline{v_R v_z} = 0$  in the disc plane, we obtain:

$$\begin{aligned} \sigma^2 &= \sigma_R^2 \left[ 1 - \frac{1}{2} (1 - \alpha_R) \cos^2 \phi \sin^2 i - \right. \\ &\quad \left. \frac{(1 + \beta/2)R^2}{\kappa q_\Phi^2 (R_c^2 + R^2)(1 + \alpha_R) + (1 + \beta/2)R^2} \cos^2 i \right]. \end{aligned} \quad (2.38)$$

When evaluated along the major axis,  $\cos^2 \phi = 1$ .

Assuming that the velocity ellipsoid is symmetric around  $v_\phi = \overline{v_\phi}$  the corresponding term in Equation (2.34) vanishes. Inserting the relations obtained from

the power-law model, we arrive at the following expression for the circular velocity:

$$V_c^2 = \bar{v}_\phi^2 - \sigma_R^2 \left[ \frac{\partial \ln \Sigma}{\partial \ln R} + \frac{\partial \ln \sigma_R^2}{\partial \ln R} + \frac{1}{2}(1 - \alpha_R) + \frac{\kappa(1 - \alpha_R)}{\kappa(2R_c^2 - R^2) + R^2} \right]. \quad (2.39)$$



---

## Chapter 3

---

# Stellar velocity profiles and line strengths out to four effective radii in the early-type galaxies NGC 3379 and NGC 821

We use the integral-field spectrograph SAURON to measure the stellar line-of-sight velocity distribution and absorption line strengths out to four effective radii ( $R_e$ ) in the early-type galaxies NGC 3379 and NGC 821. With our newly developed observing technique we can now probe these faint regions in galaxies that were previously not accessible with traditional long-slit spectroscopy. We make optimal use of the large field-of-view and high throughput of the spectrograph: by adding the signal of all  $\sim 1400$  lenslets into one spectrum, we obtain sufficient signal-to-noise in a few hours of observing time to reliably measure the absorption line kinematics and line strengths out to large radius.

We find that the line strength gradients observed within  $1 R_e$  remain constant out to at least  $4 R_e$ , which puts constraints on the merger histories of these galaxies. The stellar halo populations are old and metal-poor. By constructing orbit-based Schwarzschild dynamical models we find that dark matter is needed to explain the observed kinematics in NGC 3379 and NGC 821, with 30 - 50% of the total matter being dark within  $4 R_e$ . The radial anisotropy in our best-fit halo models is less than in our models without halo, due to differences in orbital structure. The halo also has an effect on the  $Mg\ b - V_{esc}$  relation: its slope is steeper when a dark halo is added to the model.

Anne-Marie Weijmans, Michele Cappellari, Roland Bacon, P. Tim de Zeeuw,  
Eric Emsellem, Jesús Falcón-Barroso, Harald Kuntschner, Richard M. McDermid,  
Remco C. E. van den Bosch & Glenn van de Ven  
*Monthly Notices of the Royal Astronomical Society*, in press (2009)

### 3.1 Introduction

According to the current galaxy formation paradigm, galaxies should be embedded in massive dark matter haloes (e.g. Kauffmann & van den Bosch 2002; Springel et al. 2005). For spiral galaxies, these haloes have indeed been observationally confirmed, by determining their influence on the kinematics of the H I discs that surround most of these galaxies (see e.g. van Albada et al. 1985). Early-type galaxies often lack these large gas discs, and therefore their dark matter haloes are more difficult to probe. Although some early-type galaxies do have regular H I structures that have been used to identify a dark matter halo (e.g. Bertola et al. 1993; Franx, van Gorkom & de Zeeuw 1994; Oosterloo et al. 2002; Weijmans et al. 2008) and recent sensitive radio observations have shown that H I in these galaxies is more common than previously thought (e.g. Morganti et al. 2006), for the majority of early-type galaxies we need to employ other tracers to determine the dark matter content.

Stellar kinematics are a reliable tracer of the gravitational potential in galaxies. Unfortunately, traditional long-slit spectroscopy seldom reaches beyond two half-light or effective radii ( $R_e$ ), because the necessary signal-to-noise ratio ( $S/N$ ) is difficult to achieve in this regime. In the central parts of galaxies this is not an issue, and it has been shown by various studies that in early-type galaxies within one  $R_e$  the luminous matter still dominates over the dark matter: only 10 - 50 per cent of the total mass is dark (Gerhard et al. 2001; Cappellari et al. 2006; Thomas et al. 2007). These data however do not cover the outer regions of galaxies, where the dark matter is supposed to dominate. Models of early-type galaxies based on long-slit stellar kinematics extending to larger radii are not always conclusive, but indicate that a dark halo is required in some individual cases (e.g. Carollo et al. 1995; Rix et al. 1997).

To probe the gravitational potential at larger radii (outside one  $R_e$ ), we can resort to gravitational lensing (e.g. Koopmans et al. 2006; Gavazzi et al. 2007), X-ray emission (e.g. O'Sullivan & Ponman 2004; Humphrey et al. 2006) or discrete tracers such as globular clusters (e.g. Côté et al. 2003; Bridges et al. 2006) or planetary nebulae (e.g. Romanowsky et al. 2003; Douglas et al. 2007; Napolitano et al. 2009). Interestingly, Romanowsky et al. (2003) found that models of their sample of three intermediate luminosity early-type galaxies only required a small amount of dark matter, if any at all. Dekel et al. (2005) subsequently argued that the observed kinematics of the planetary nebulae (PNe) could also be explained by invoking radial anisotropy, and therefore do not exclude a dark halo (see also Binney & Mamon 1982). Douglas et al. (2007) presented newly reduced PNe kinematics for one of the galaxies of the Romanowsky et al. sample

Parameter	NGC 821	NGC 3379
Morphological Type	E6?	E1
$M_B$ (mag)	-20.74	-20.57
Effective $B - V$ (mag)	0.87	0.93
Photometric PA ( $^\circ$ )	32	68
Distance modulus (mag)	31.85	30.06
Distance (Mpc)	23.4	10.3
Distance scale (pc arcsec $^{-1}$ )	114	50
Effective radius (arcsec)	39	42
Systemic velocity (km/s)	1726	930

**Table 3.1** — Properties of NGC 821 and NGC 3379. Magnitude and colour are taken from the Lyon/Meudon Extra galactic Database (LEDa). The distance modulus was derived from surface brightness fluctuation measurements by Tonry et al. (2001). Note that 0.06 mag is subtracted to adjust to the Cepheid zeropoint of Freedman et al. (2001); see Mei et al. (2005), section 3.3, for a discussion. The effective radius and position angle are taken from Cappellari et al. (2007).

(NGC 3379) and found the dark matter fraction within  $5 R_e$  to be less than 40 per cent, which is significantly lower than what is predicted by  $\Lambda$ CDM models. Napolitano et al. (2009) reached similar conclusions modeling PNe kinematics in the elliptical galaxy NGC 4494 and suggested that intermediate-luminosity galaxies are surrounded by low concentration haloes, while some high-mass ellipticals could have more strongly concentrated haloes. De Lorenzi et al. (2009) presented mass models of NGC 3379 based on the PNe kinematics of Douglas et al. (2007), combined with long-slit and central SAURON integral-field data, and concluded that they can fit the data with a range of mass distributions, depending on the anisotropy. They did not exclude a dark matter halo with a strong radially anisotropic outer envelope, that is still consistent with merger models within the  $\Lambda$ CDM paradigm.

We observed two of the galaxies of the Romanowsky et al. (2003) sample, NGC 3379 and NGC 821, with the SAURON integral-field unit (IFU), to measure the line-of-sight velocity distribution (LOSVD) at large radii (3-4  $R_e$ ). We took advantage of the high throughput and large field-of-view of SAURON ( $41 \times 33$  arcsec $^2$ ) and used the IFU as a “photon collector”: for each observation we co-added all spectra within one field to acquire enough  $S/N$  to measure the LOSVD up to the fourth Gauss-Hermite moment  $h_4$ . These higher order moments are key to breaking the mass-anisotropy degeneracy when constructing mass models and determining the dark matter content of galaxies (e.g. Gerhard 1993). Apart from

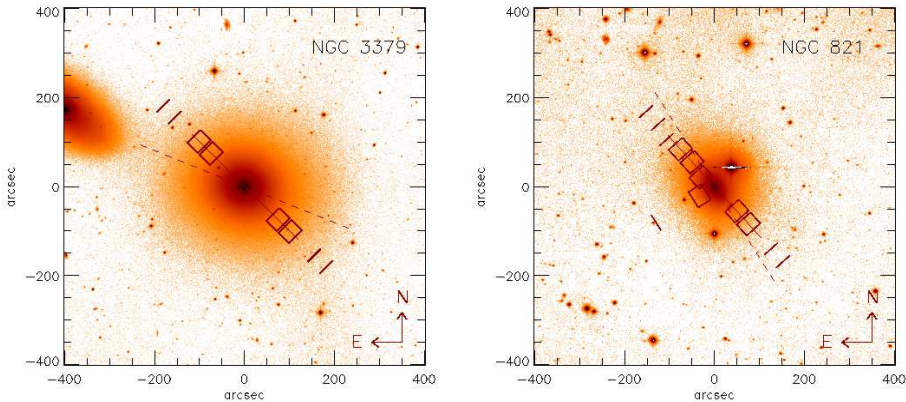


**Figure 3.1** — Positions of our observed fields in NGC 3379 (left) and NGC 821 (right). The red boxes denote each SAURON field of view. The skylenslets (red short thick lines) are aligned with the long side of the SAURON field, at a distance of two arcminutes. SAURON was orientated such that the skylenslets pointed away from the galaxy nucleus. The fields are not exactly aligned with the major axis of the galaxy (denoted by the dashed line) to minimize the contamination of foreground stars and neighbouring galaxies. The underlying images were obtained with the 1.3-m McGraw-Hill Telescope at MDM Observatory.

the LOSVD, we also obtained line strengths from our spectra, allowing us to study line strength gradients out to large radii and constraining the properties of the stellar halo populations. Both NGC 3379 and NGC 821 are well studied galaxies, and some of their properties are summarized in Table 3.1. Their central regions have been observed as part of the SAURON survey (de Zeeuw et al. 2002). They are classified as fast rotators (Emsellem et al. 2007) and display regular stellar kinematics.

In section 3.2, we describe our observations and data reduction. We present our spectra and discuss the resulting LOSVD in section 3.3. Section 3.4 is devoted to measuring line strengths and we investigate gradients and the properties of the stellar populations at large radii. In section 3.5 we present our mass models of NGC 3379 and NGC 821 (including a dark matter halo) and connect the dynamical properties with stellar populations by constructing the  $Mgb - V_{\text{esc}}$  relation. Section 3.6 summarizes and discusses our results.

## 3.2 Observations and data reduction

We observed four fields in NGC 3379 with SAURON at the William Herschel Telescope at La Palma, Spain, in March 2005. The fields were centred at 2.6 and 3.5  $R_e$ , on opposite sides of the nucleus to allow for an evaluation of the systemic velocity of the system. They were not placed on the major axis of the galaxy but instead on an axis that deviates by  $23^\circ$ . This was done to avoid contamination in our outer field by the neighbouring galaxy NGC 3384. The positions of the fields were chosen such that most of them did not contain foreground stars, and they were oriented such that the skylenslets of SAURON pointed away from the galaxy nucleus, obtaining skyspectra 2 arcminutes away from the SAURON field.

We used a similar strategy to observe six fields in NGC 821 in September 2006. One field was situated on the minor axis, one field at 1  $R_e$ , two fields at opposite sides of the galaxy nucleus at 2  $R_e$  and the last two fields on opposite sides of the nucleus at 3  $R_e$ . Figure 3.1 shows the observed fields in NGC 3379 and NGC 821, and Table 3.2 summarizes their exposure times and exact positions.

The data were reduced using the dedicated XSAURON software (Bacon et al. 2001). The shutter of SAURON malfunctioned during the observing run of NGC 821, and did not close during read-out of the CCD. This did not affect our science frames, whose exposure times of 1800 seconds are long compared to the typical read-out time of the CCD ( $\sim 30$  seconds). However, our calibration frames have shorter exposure times (15 - 60 seconds) and were badly contaminated by light hitting the CCD during read-out. We could therefore not rely on these calibration frames. Instead, we took the calibration frames obtained during the observing run of NGC 3379 and rotated and translated them so that they coincided with the contaminated frames that they would replace. The spectra of NGC 821 were then extracted and flat-fielded using these frames.

We checked that the extraction of the spectra was done accurately, but we found residuals in the frames after flat-fielding. This was to be expected: although the extraction mask is rather stable between observing runs, the flat-field is not. We therefore constructed a superflat by combining our six empty frames with 30 frames of a Lyman  $\alpha$  emitting halo, taken during the same run (see Weijmans et al. 2009b for details). Since these 36 frames contain (mostly) empty sky and are offset with respect to each other, their median, smoothed in the spectral direction, proved to be a suitable superflat (see also Bower et al. 2004). Dividing our already flat-fielded spectra by this superflat removed most of the residuals. Coincidentally, we could also construct a superflat for our NGC 3379 dataset: immediately after our observing run SAURON was used in the same setup to observe Lyman  $\alpha$  emission around high redshift submillimeter galaxies. These frames also consist

Galaxy	Field	$R/R_e$	$T_{\text{exp}}$ (hr)	$\mu_V$ (mag/arcsec <sup>2</sup> )	$S/N$	galaxy contr. (per cent)	Comments
NGC 3379	3N	2.6	2.0	23.0	-	-	cloudy conditions, no signal
	3S	2.6	2.5	23.0	29	15	
	4N	3.5	7.5	23.7	16	5	cloudy conditions
	4S	3.5	2.0	23.7	21	13	
NGC 821	minor	1.0	1.5	23.0	58	28	
	1N	0.9	1.5	21.7	57	24	
	2N	1.9	1.5	23.3	12	7	cloudy conditions
	2S	1.9	0.5	23.3	-	-	cloudy conditions, no signal
	3N	2.9	4.0	24.5	-	-	cloudy conditions, no signal
	3S	2.9	4.0	24.5	9	4	

**Table 3.2** — Properties of our observed fields in NGC 3379 and NGC 821. The fields are named according to their distance and orientation with respect to the galaxy centre, see Figure 3.1. The surface brightness  $\mu_V$  is calculated from the MDM images, and can be compared to the sky surface brightness, which in  $V$ -band is about 21.7 mag/arcsec<sup>2</sup> in optimal conditions at our observed fields (Benn & Ellison 1998).

mostly of empty sky, and 19 of them were used to create a superflat for NGC 3379.

After superflat-fielding, both datasets were reduced in the standard manner, except that we did not subtract the sky from the spectra. We will take the contribution of the sky into account when fitting the spectra to extract the stellar kinematics (see Section 3.3).

### 3.3 Stellar kinematics

To extract the stellar kinematics from our spectra, we used the penalized pixel fitting method (pPXF)<sup>1</sup> of Cappellari & Emsellem (2004). This method fits a stellar template spectrum, convolved with a line-of-sight velocity distribution (LOSVD), to the observed galaxy spectrum in pixel space (i.e. logarithmically binned in wavelength). If apart from the mean velocity  $V$  and velocity dispersion  $\sigma$  also the Gauss-Hermite moments  $h_3$  and  $h_4$  are fitted, then the solution is biased towards a Gaussian. The amount of biasing can be controlled, and following the recipe described in Cappellari & Emsellem (2004) we found that a penalization factor of  $\lambda = 0.5$  gives the best results for our dataset and signal-to-noise.

#### 3.3.1 Method

To find a suitable stellar template to fit our spectra, we co-added all the spectra of the central SAURON fields of NGC 821 and NGC 3379, presented in Emsellem et al. (2004). We then determined the optimal template for these high signal-to-noise spectra as a linear superposition from the full MILES library, containing 945 stars (Sánchez-Blázquez et al. 2006). For NGC 3379, a template consisting of 19 stars was created, and for NGC 821 a template of 21 stars. Template mismatch is negligible, as can be seen in Figure 3.2. We used these templates to measure the stellar kinematics in our spectra at large radii in NGC 3379 and NGC 821. Additive polynomials were included in our fit to compensate for changes in line strengths, which are to be expected over the radial range that we cover. We found that varying the stellar templates gave similar results for the kinematics within the errors.

Since our spectra are very skydominated (see Table 3.2), we did not subtract the sky from our spectra, but instead included the skyspectra obtained by co-adding the spectra observed with the  $\sim 170$  skylenslets of SAURON (pointing  $\sim 2$  arcminutes away from the field of view) for each exposure as separate templates into pPXF. While the stellar template was broadened with the LOSVD, at the

<sup>1</sup>available from [www-astro.physics.ox.ac.uk/~mxc/idl/#ppxf](http://www-astro.physics.ox.ac.uk/~mxc/idl/#ppxf)



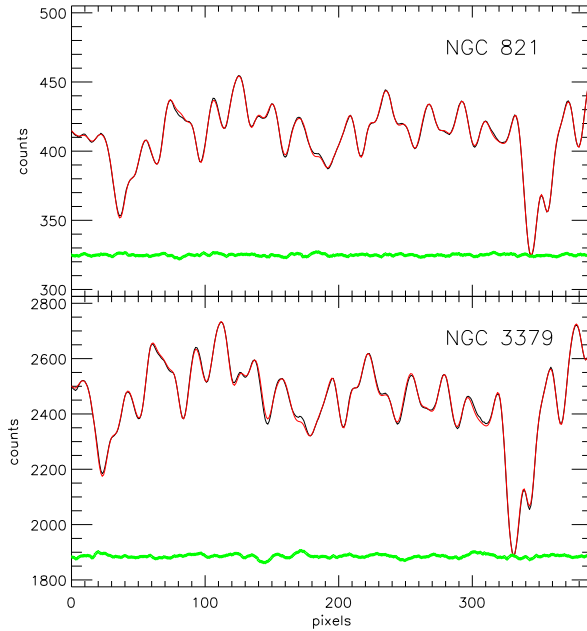


**Figure 3.2** — Co-added spectra of NGC 821 and NGC 3379 (black line) and overplotted their optimal stellar templates broadened with the best-fitting LOSVD (grey line). Residuals (grey small dots, shown with offset for presentation purposes) are small, and due to template mismatch.

same time the sky spectra were scaled to minimize the  $\chi^2$ . The modeled spectrum  $G_{\text{mod}}$ , with  $x$  in pixelspace, is then described by:

$$G_{\text{mod}}(x) = [B \otimes T](x) + \sum_{l=0}^L b_l \mathcal{P}_l(x) + \sum_{n=1}^N w_n S_n(x), \quad (3.1)$$

with  $B(x)$  the broadening function,  $T(x)$  the optimal stellar template,  $\mathcal{P}_l(x)$  the  $L + 1$  additive polynomials of degree  $l$  with coefficients  $b_l$ , and  $S_n(x)$  the  $N$  sky templates, with weight  $w_n \geq 0$  (see also Eq. 3 in Cappellari & Emsellem 2004). By fitting the contribution of the sky in this way instead of subtracting the skyspectra directly, we allow the inclusion of subtle sky variations. We found that especially for the spectra with a low galaxy contribution (see Table 3.2) this improved the fits significantly.

We subtracted the resulting composite skytemplate  $\sum_{n=1}^N w_n S_n(x)$  from the observed spectrum, and ran pPXF again. Errors are estimated by a Monte Carlo method, where we measured the kinematics from many realisations of the in-



put spectrum, on which we added noise. The noise spectrum was obtained from the difference between our observed spectrum and the best-fit modeled spectrum ( $G_{\text{mod}}$ ). We found that varying the amount of subtracted sky by up to 10 per cent does not affect our measured LOSVD. This shows that our LOSVD parameters are robust to errors in our sky subtraction. We also checked that the measured LOSVD is indeed the LOSVD of the galaxy and not an imprint of the solar spectrum from e.g. zodiacal light: when measuring the LOSVD of the sky templates themselves we measured a velocity offset with respect to the galaxy comparable to the systemic velocity of the system, and a much smaller broadening.

We found that the best fits were obtained by including the skyspectra from the skylenslets, taken simultaneously with our galaxy spectra. Providing the sky spectra of our blank skyfields as templates gave worse results, even though these fields covered a larger sky area than the skylenslets and therefore had higher  $S/N$ . This indicates the importance of obtaining simultaneous skyspectra over high  $S/N$ , to avoid mismatch due to the variability of the night sky.

Finally, we tested the influence of subtracting residual galaxy light that could be present in our sky spectra, since the skylenslets were pointing at  $6 - 7 R_e$  in the galaxy. The galaxy light at these distances of the nucleus is however very faint, approximately  $3-4 \text{ mag/arcsec}^2$  fainter than in the regions where we measure our kinematics. We simulated the effect of subtracting such a weak Gaussian absorption line from our observed line and found that the maximal error we can introduce in this way is  $8 \text{ km/s}$  in our measured velocity dispersions. This is well within our error bars, and we conclude that this effect is negligible.

### 3.3.2 NGC 3379

It turned out that one of our fields in NGC 3379, 3N, did not have sufficient signal to measure the LOSVD. The results for the other fields can be found in Figure 3.3 and Table 3.3. The last four columns for Table 3.3 show the results for the LOSVD if we restrict our fit to the first two moments, instead of fitting up to  $h_4$ . The results for both fits agree within the errors.

Correcting for barycentric motion, we find that the systemic velocity  $V_{\text{sys}}$  of the galaxy measured from the central field (presented by Emsellem et al. 2004) is  $930 \pm 2 \text{ km/s}$ . This agrees with  $V_{\text{sys}}$  as determined from the 3S and 3N field pair: although we could not measure the velocity dispersion from the spectrum in 3N, we were able to determine the positions of the absorption lines in the spectrum and therefore the velocity offset with respect to the 3S field, opposite the nucleus. By averaging the two velocities from these field we find  $V_{\text{sys}} = 938 \pm 16 \text{ km/s}$ . However, repeating this exercise for the field pair at  $3.5 R_e$ , which are 4S and 4N,

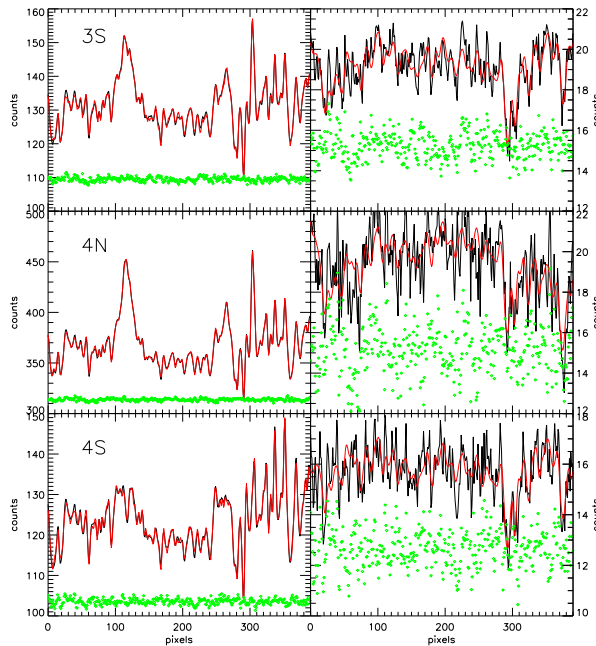


**Figure 3.3** — Spectra of our fields in NGC 3379. The left panels show the observed spectra (not sky-subtracted) in black, with overplotted in grey the best fit from pPXF (combination of stellar template broadened with LOSVD and scaled sky templates). The residuals (diamonds) are offset for presentation purposes. Right: sky-subtracted spectra (black) with the same broadened LOSVD (grey) as in the left panels. Residuals are again shown as diamonds.

we find  $V_{\text{sys}} = 892 \pm 23$  km/s, which seems marginally deviant from our other two measurements, although this is just outside the  $1\text{-}\sigma$  interval. We therefore decided to subtract for each field pair their own corresponding systemic velocity.

In Figure 3.4 we compare our results with the long-slit data of Statler & Smecker-Hane (1999). The radial extent of the absorption line kinematics has been increased by a factor two compared to the long-slit data, and our data show a smooth continuation of kinematics out to larger radii. We see little rotation at large radii, and the dispersion profile remains flat out to  $3.5 R_e$ , although there is a hint that the profile is slightly dropping. We also plot the kinematic profiles of the planetary nebulae, as presented in Coccato et al. (2009). We folded these profiles to negative radii, to allow comparison with our data at large radii also in these ranges. We find a good agreement between the several datasets, although the rotational velocities found by the planetary nebulae seem to be a bit higher ( $\sim 30$  km/s) than our findings.

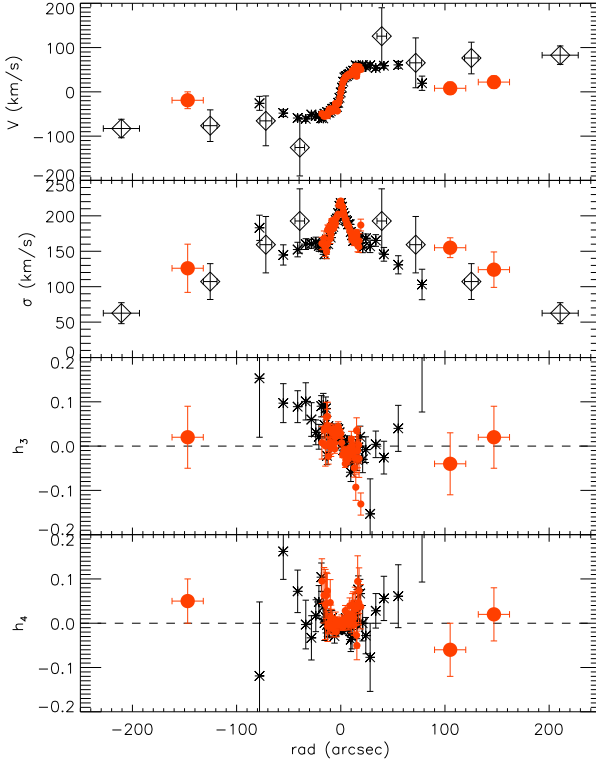


**Figure 3.4** — Kinematic profiles along the major axis of NGC 3379. The small grey dots denote the central SAURON data from the original survey and the big red dots are our data at large radii. For comparison, we also plot the long-slit data of Statler & Smecker-Hane (1999) with black stars and the planetary nebulae profiles as presented by Coccato et al. (2009) with open diamonds. The horizontal error bars for the SAURON data at large radii indicate the width of the SAURON field-of-view (30 arcsec), while the horizontal error bars of the PNE data indicate the radial range containing 68 per cent of the PNE used to calculate the kinematics.

### 3.3.3 NGC 821

The spectra and results for our fields in NGC 821 can be found in Figure 3.5 and Table 3.4. Unfortunately, weather conditions did not allow us to obtain enough signal to measure the LOSVD in all our observed fields, but at each radius one suitable spectrum could be obtained. The systemic velocity from the central kinematics (Emsellem et al. 2004) is  $1726 \pm 2$  km/s (barycentric corrected). This is in agreement with  $V_{\text{sys}}$  measured from our two field pairs at  $1.9 R_e$  (2S and 2N), where we find a value of  $1704 \pm 25$  km/s. Unfortunately, we could not measure  $V_{\text{sys}}$  from our field pair at  $2.9 R_e$  due to lack of signal in field 3N. However, our field at the minor axis of NGC 821 gives an independent determination of  $V_{\text{sys}}$ , assuming axisymmetry so that here the rotational velocity should be zero. We then find  $V_{\text{sys}} = 1710 \pm 7$  km/s and  $V_{\text{sys}} = 1716 \pm 7$  km/s, depending on whether we fit up the LOSVD up to  $h_4$  or only the first two moments, respectively. Since all these measurements of  $V_{\text{sys}}$  agree within the errors, we fixed  $V_{\text{sys}}$  such that the velocity measured on the minor axis is zero.

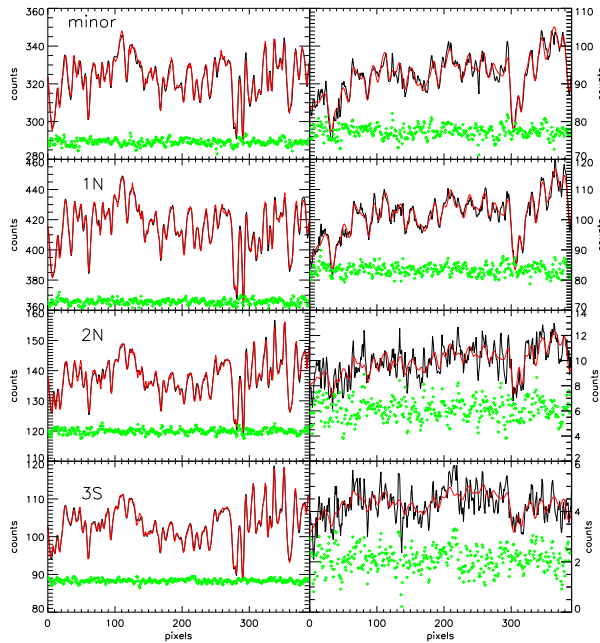


**Figure 3.5** — Same as Figure 3.3, but now for our fields in NGC 821.

Figure 3.6 compares our result with the long-slit data of Forestell & Gebhardt (2008). We note that especially in the centre there seem to be some deviations between this dataset and the SAURON data. Differences in sampling between the two datasets (nearly-round bins for the SAURON data versus long, elongated bins for the long slit data) could in principle result in differently-weighted values, but we expect that this effect is small. The most likely cause for the observed deviations are differences in fitted wavelength interval and stellar templates. Also shown are the results from Coccato et al. (2009), who re-analysed the planetary nebulae data that were previously presented by Romanowsky et al. (2003). These data are in good agreement with our stellar kinematics at large radii.

### 3.4 Line strengths

To measure the absorption line strengths in our spectra, we follow the procedure outlined in Kuntschner et al. (2006). Briefly, we can measure three Lick indices in the SAURON wavelength range:  $H\beta$ ,  $Fe5015$  and  $Mg b$ , defined in Table 2 of Kuntschner et al. (2006). We do not need to remove emission lines from our

Field	$\Delta x$ (arcsec)	$\Delta y$ (arcsec)	$V$ (km/s)	$\delta V$ (km/s)	$\sigma$ (km/s)	$\delta\sigma$ (km/s)	$h_3$	$\delta h_3$	$h_4$	$\delta h_4$	$V_{\text{mean}}$ (km/s)	$\delta V_{\text{mean}}$ (km/s)	$\sigma_{\text{mean}}$ (km/s)	$\delta\sigma_{\text{mean}}$ (km/s)
3S	-77	-77	8	14	155	14	-0.04	0.07	-0.06	0.06	5	11	147	12
4N	104	104	-19	19	126	34	0.02	0.07	0.05	0.05	-16	19	134	35
4S	-104	-104	22	14	124	25	0.02	0.07	0.02	0.06	23	14	127	19

**Table 3.3** — Stellar kinematics at large radii for NGC 3379.  $\Delta x$  and  $\Delta y$  denote the offsets (East and North, respectively) from the nucleus of the galaxy to the centre of our observed fields. The quoted errors are 1- $\sigma$  errors, determined from Monte Carlo simulations.  $V_{\text{mean}}$  and  $\sigma_{\text{mean}}$  are derived by fitting only the first two moments of the LOSVD.

Field	$\Delta x$ (arcsec)	$\Delta y$ (arcsec)	$V$ (km/s)	$\delta V$ (km/s)	$\sigma$ (km/s)	$\delta\sigma$ (km/s)	$h_3$	$\delta h_3$	$h_4$	$\delta h_4$	$V_{\text{mean}}$ (km/s)	$\delta V_{\text{mean}}$ (km/s)	$\sigma_{\text{mean}}$ (km/s)	$\delta\sigma_{\text{mean}}$ (kms/)
minor	33	-21	0	7	171	8	0.07	0.04	0.00	0.04	0	7	168	7
1N	19	30	119	10	174	8	0.00	0.03	-0.04	0.04	112	9	170	7
2N	39	63	72	20	131	22	-0.02	0.07	0.02	0.06	64	18	135	19
3S	-60	-96	-1	28	163	43	-0.02	0.06	0.04	0.06	-8	27	162	38

**Table 3.4** — Stellar kinematics at large radii for NGC 821, similar to Table 3.3.

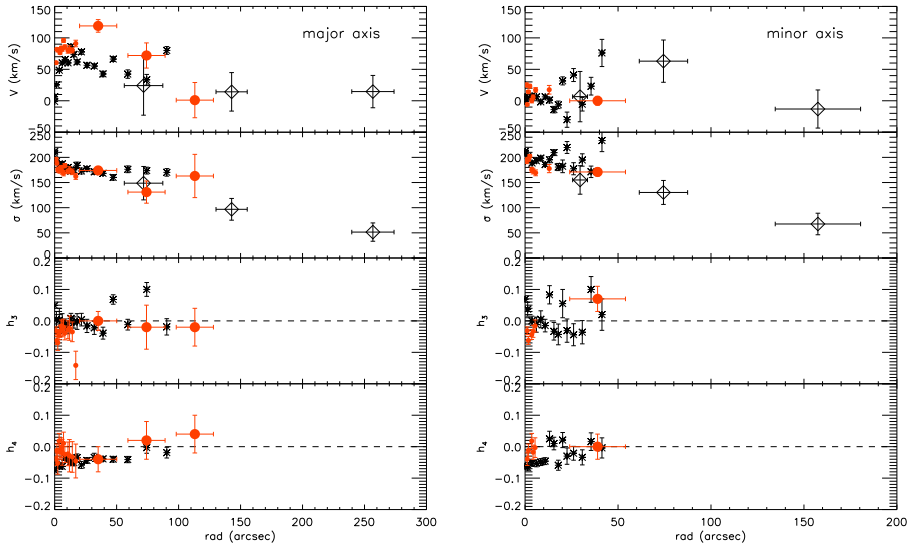


**Figure 3.6** — Kinematic profiles along the major (left) and minor (right) axis of NGC 821. As in Figure 3.4, small grey dots are the central SAURON data of the original survey, big grey dots are our data at large radii and open diamonds denote planetary nebulae kinematics from Coccato et al. (2009). The black stars are long-slit stellar kinematics from Forestell & Gebhardt (2008). Horizontal error bars are as described in Figure 3.4.

spectra, since our galaxies show no sign of ionised gas outside the central regions (Sarzi et al. 2006). To calibrate to the Lick/IDS system, we broaden our spectra to an instrumental resolution of  $\sigma = 212 \text{ km s}^{-1}$ . We correct our measured line strengths for the broadening caused by the LOSVD and we apply the offsets from Table 3 in Kuntschner et al. (2006) to correct for differences in the shape of the continuum, since the Lick/IDS spectra have not been flux calibrated.

We noticed that the continuum shape blue-ward of the  $H\beta$  feature in our spectra was affected by bad flatfielding or wrong sky subtraction. We therefore applied the same continuum correction as was done in Kuntschner et al. (2006) and fitted an 11<sup>th</sup> order multiplicative polynomial together with an optimal stellar template to our spectra. The template had been broadened with the observed LOSVD. We then divided our observed spectrum by this polynomial, before determining the  $H\beta$  index.

Field	H $\beta$ ( $\text{\AA}$ )	error ( $\text{\AA}$ )	Fe5015 ( $\text{\AA}$ )	error ( $\text{\AA}$ )	Mg <i>b</i> ( $\text{\AA}$ )	error ( $\text{\AA}$ )
NGC 821						
minor	1.61	0.22	3.80	0.28	3.13	0.16
1N	1.30	0.20	4.11	0.24	3.45	0.17
2N	1.19	0.81	5.16	1.37	5.47	0.64
3S	0.00	1.19	12.0	1.71	6.43	0.76
NGC 3379						
3S	1.49	0.45	2.45	0.58	3.42	0.26
4N	2.13	0.92	2.66	0.86	3.05	0.45
4S	1.17	0.51	2.46	0.66	3.61	0.43

**Table 3.5** — Line strengths indices in our observed fields in NGC 821 and NGC 3379.

### 3.4.1 Results

We present our results for NGC 3379 and NGC 821 in Table 3.5. Errors are estimated with Monte Carlo simulations, where we add noise to our spectra (defined by the difference between our observed and fitted spectra, see Figures 3.3 and 3.5) and vary the bandpasses of the index and the continuum to take the uncertainty in radial velocity into account.

A possible source of contamination for our line strength measurements is the [O III] emission of planetary nebulae. From the catalog of Douglas et al. (2007), each of our fields in NGC 3379 contains one to two planetary nebulae. Following Sarzi et al. (2005), their Equation 1, we should be sensitive to emission lines with  $\text{EW} > 0.7 \text{ \AA}$ . We carefully checked the individual spectra in each cube, prior to co-adding, and found no evidence for such emission.

We also investigated the effect of sky subtraction on the determinations of line strength. By varying the amount of sky that we subtracted from our spectra, we found that our measurements of H $\beta$  and Fe5015 are quite robust against an error in sky subtraction, even if the sky levels are varied by 10 per cent. Mg *b* is however already severely affected by a sky subtraction error of only two per cent (see Figure 3.7). This may be due to the proximity of the solar Mg *b* absorption feature present in the sky spectrum. Our Fe5015 and Mg *b* indices at 2 and 3  $R_e$  in NGC 821 are unrealistically high, and therefore could be suffering from this problem, although variations in the continuum shape of the spectrum also play a role (see next section). The indices at 1  $R_e$  in this galaxy are less affected, and are in agreement with Proctor et al. (2005). They determined line strengths

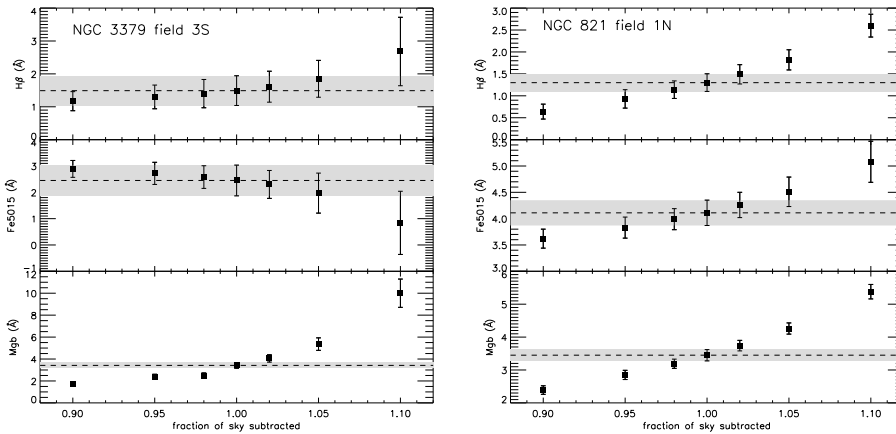


**Figure 3.7** — The effect of sky subtraction on our line strength measurements, for the field 3S in NGC 3379 (left) and the 1N field in NGC 821 (right). The x-axis denotes the fraction of sky subtracted. The dashed line indicates the line index when the sky is totally removed, while the grey box denotes the  $1\text{-}\sigma$  interval.  $H\beta$  and Fe5015 are robust against an error in sky subtraction up to 5 per cent, though oversubtracting is more severe than undersubtracting.  $Mg\ b$  is very sensitive to sky subtraction errors.

from long-slit data in this galaxy out to  $1 R_e$ . We are not aware of studies in the literature where line strengths have been determined outside  $1 R_e$  for these galaxies, to compare our results with.

### 3.4.2 Line strength gradients

Line strength gradients are key instruments to study the formation history of galaxies, since different formation models predict different gradients. Monolithic collapse models (Carlberg 1984) produce steep metallicity gradients and a metal-rich nucleus, while hierarchical models show shallower gradients, as mergers dilute existing line strength gradients (White 1980). However, subsequent starformation induced by gas-rich mergers can steepen the gradients again, at least in the central regions (Hopkins et al. 2009a).

Our measurements allow us to study line strength gradients out to large radii. Many previous studies of galaxy samples (e.g. Davies, Sadler & Peletier 1993; Kuntschner et al. 2006; Sánchez-Blázquez et al. 2007) have been limited to  $\sim 1 R_e$ , but showed that typically for galaxies without contributions from young stellar populations,  $H\beta$  remains flat or increases slightly with radius, while the metal line strengths have negative gradients.



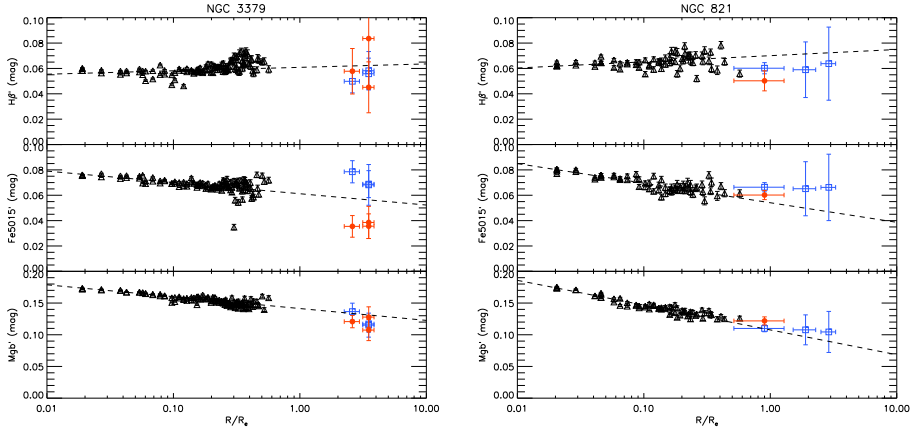


**Figure 3.8** — Line strength indices  $H\beta$ ,  $Fe5015$  and  $Mg\ b$  (in magnitudes) as a function of radius. Left panel: NGC 3379, right panel: NGC 821. Black triangles show indices measured on the SAURON central field, taken from a slit positioned on the major axis of the galaxy, with a width of 2 arcsec. Grey filled dots show our large radii results, and the horizontal error bars denote the size of the SAURON field of view. The points at 2 and 3  $R_e$  in NGC 821 cannot be considered reliable, probably because of continuum shape problems, and therefore are not shown here. The open squares denote our measurements directly from templates of single stellar population models, see text for details. Overplotted is the best fitting linear relation between index and  $\log(\text{radius})$ , determined within  $R_e/4$ .

To calculate the line strength gradients in our two galaxies, we follow Kuntschner et al. (2006) and first convert our indices from  $\text{\AA}$  to magnitudes:

$$\text{index}' = -2.5 \log\left(1 - \frac{\text{index}}{\Delta\lambda}\right), \quad (3.2)$$

with  $\Delta\lambda$  the width of the index bandpass in  $\text{\AA}$ . Indices expressed in magnitudes will from now on be indicated by a prime sign [ $'$ ]. Line strength gradients are then defined as:

$$\Delta \text{index}' = \frac{\delta \text{index}'}{\delta \log(R/R_e)}. \quad (3.3)$$

We show in Figure 3.8 our line strength indices in magnitudes as a function of radius, with red dots. Also plotted are the values for the central SAURON fields (Kuntschner et al. 2006), which fall within a 2 arcsec wide slit positioned along the major axis of the galaxy. We fitted a linear relation between each index and

$\log(\text{radius})$  within  $R_e/4$ , to determine the gradient. These gradients are overplotted in the figure, and are compared to our measurements at large radii.

With our new data, we confirm in NGC 3379 the trends mentioned above, that  $H\beta$  mildly increases and Fe5015 and  $Mg\ b$  decrease with radius. This indicates that the metallicity in the galaxy keeps decreasing linearly with  $\log(\text{radius})$  when going from the centre out to larger radii. The gradients for  $H\beta$  and  $Mg\ b$  seem to remain constant out to  $4 R_e$ , but Fe5015 falls off more steeply. This would imply an unrealistically high  $\alpha$ -enhancement at large radii. To check whether our Fe5015 measurements are affected by continuum shape problems, we did the following test. We remeasured the kinematics in our spectra with pPXF, but this time used the stellar model library of Vazdekis et al. (2007) based on the MILES library ( $-1.68 < Z/H < 0.0$ ;  $1 \text{ Gyr} < \text{age} < 17.78 \text{ Gyr}$ ) and multiplicative instead of additive polynomials, to allow for a varying continuum shape. The resulting kinematics were consistent with our previous finding. The line strengths were then measured on the composite best-fitting stellar template, without the multiplicative polynomials. The results are also shown in Figure 3.8, as blue squares. For  $H\beta$  and  $Mg\ b$  both the direct measurements and the measurements on the stellar templates give similar results, but the values for Fe5015 are higher and consistent with the observed gradient in the central part of the galaxy. We therefore conclude that indeed our measurements for Fe5015 suffer from changes in continuum shape, but that our values for  $H\beta$  and  $Mg\ b$  are robust. For NGC 821 we see a similar effect.

Our observation that the line strength gradients are constant out to large radii provides constraints for the merger and star formation history of the galaxy. After a gas-rich merger, star formation in the central regions of the remnant is expected to steepen the gradients, while at larger radii violent relaxation flattens them, though over time ( $\sim 3 \text{ Gyr}$ ) the steep gradients in the central part get weaker (Hopkins et al. 2009a; Hopkins et al. 2009b).

### 3.4.3 Stellar population models

Using the stellar population models of Thomas, Maraston & Bender (2003) and Schiavon (2007), we explore the single stellar population (SSP) equivalent age and metallicity in NGC 3379 and NGC 821 at large radii. Following the approach of Thomas et al. (2003) we define an abundance ratio insensitive metallicity index similar to their  $[MgFe]'$  index by using the  $Mg\ b$  and Fe5015 indices available

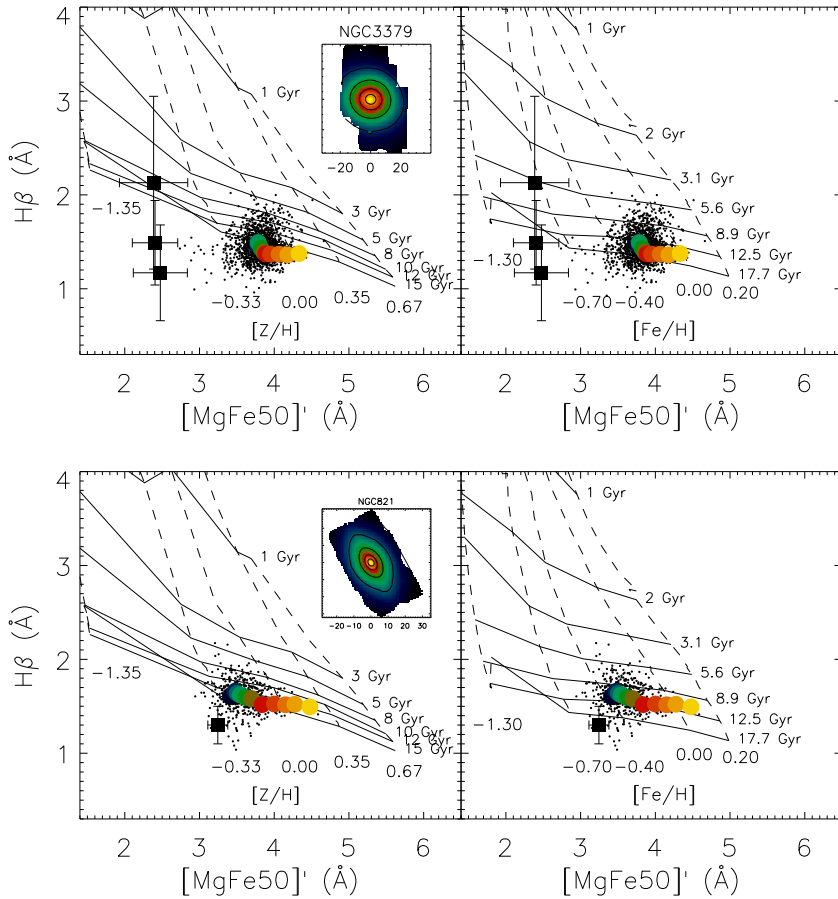


**Figure 3.9** —  $H\beta$  index against  $[MgFe50]'$  (both in Å) in NGC 3379 (top) and NGC 821 (bottom). Left panels show the Thomas et al. (2003) stellar population models (solid and dashed lines) and right panels the Schiavon (2007) models. Black dots indicate measurements from the SAURON central field, while the grey dots are averaged along isophotes (see inset for grey-scale coding). The black filled squares show the data at large radii, revealing an old (12 Gyr) and metal-poor (below 20 per cent solar metallicity) population for both models, though the uncertainties in these values are large. See colour supplement for a colour version of this figure.

from SAURON.  $[\text{MgFe50}]'$  is defined as:

$$[\text{MgFe50}]' = \frac{0.69 \times \text{Mgb} + \text{Fe5015}}{2}. \quad (3.4)$$

The scaling factor for the Mg  $b$  index was optimized such that the mean difference between solar and non-solar ratio model predictions from Thomas et al. (2003) is zero. In Figure 3.9 we plot this index versus  $\text{H}\beta$  and compare with the models. Even though the models of Thomas et al. (2003) and Schiavon (2007) are constructed independently, using different stellar libraries and fitting functions, they give the same results for our data at large radii. For NGC 3379 we find that at 3 - 4  $R_e$ , the stellar population is consistent with an old (12 Gyr) population, and metal-poor, with  $[\text{Z}/\text{H}]$  slightly below 20 per cent of the solar metallicity. We note however that the uncertainty in these values is rather large. For NGC 821, we find that at 1  $R_e$  the stellar population is of the same age and metallicity range as obtained from the outer bins of the SAURON central field ( $\sim 0.6 R_e$ ).

Stellar population models predict a decrease in stellar mass-to-light ratio  $M_*/L$  if the metallicity of the stellar population decreases, since the stars then become bluer and therefore brighter in the optical. For instance, for a change in metallicity from 0.0 to -0.84 at a constant age of 10 Gyr (consistent with our observations),  $M_*/L$  decreases by about 23 per cent in the models of Maraston (2005). However, for increasing stellar age at constant metallicity,  $M_*/L$  also increases. Given this degeneracy and uncertainties, we adopt a constant stellar  $M/L$  while constructing the dynamical mass models that we present in the next section. Furthermore,  $M_*/L$  depends strongly on  $\text{H}\beta$  (see e.g. Cappellari et al. 2006). Since the  $\text{H}\beta$  profiles in our galaxies are nearly flat out to large radii, variations in  $M_*/L$  are most likely small.

### 3.5 Dynamical models

To explore whether our data of NGC 3379 and NGC 821 are consistent with a dark matter halo, we model these galaxies with the triaxial Schwarzschild code presented by van den Bosch et al. (2008). Orbits are calculated within an a priori specified triaxial potential, and a superposition of orbits is determined that best fits the observed kinematics, using the observed surface brightness and self-consistency as constraints. This way, the viewing directions, stellar mass-to-light ratio  $M_*/L$ , central black hole mass  $M_\bullet$  as well as the internal orbital structure can be determined (see also van de Ven, de Zeeuw & van den Bosch 2008; van

den Bosch & van de Ven 2009). Within the limits of the observed photometry and LOSVD, the velocity anisotropy of the galaxy can vary freely.

### 3.5.1 Including a dark halo

We extended the triaxial Schwarzschild code by adding a dark matter halo to the gravitational potential, which already consisted of a stellar contribution inferred from the observed photometry and a Plummer potential for the contribution of the central black hole (see van den Bosch et al. 2008 for more details). We parametrise the dark halo with a spherical NFW profile (Navarro, Frenk & White 1996):

$$\rho(r) = \frac{\rho_s}{r/r_s(1+r/r_s)^2}, \quad (3.5)$$

with  $\rho_s$  the characteristic density of the halo and  $r_s$  a characteristic radius. The potential generated by this density distribution is then given by:

$$\Phi(r) = -4\pi G\rho_s r_s^2 \frac{r}{r_s} \ln\left(1 + \frac{r}{r_s}\right), \quad (3.6)$$

where  $G$  is the gravitational constant.

We are interested in the presence and acceptable mass range of the halo; modeling the shape of the halo in detail is beyond the scope of this paper. We therefore fix the concentration  $c = r_{200}/r_s$  of the halo to 10, as indicated by cosmological simulations (Bullock et al. 2001). Here  $r_{200}$  is the radius of the halo within which the mean density has dropped to 200 times the critical density  $\rho_{\text{crit}}$ . It can be shown that

$$\frac{\rho_s}{\rho_{\text{crit}}} = \frac{200}{3} \frac{c^3}{\ln(1+c) - c/(1+c)}, \quad (3.7)$$

such that  $c$  determines  $\rho_s$  in the potential of Equation 3.6. We vary the halo mass,

$$M_{200} = 4\pi\rho_s r_s^3 \left[ \ln(1+c) - \frac{c}{1+c} \right], \quad (3.8)$$

which is the enclosed mass within  $r_{200}$ , yielding  $r_s$ . We only fit for  $M_{200}$  and keep  $M_*/L$  fixed to the maximum value allowed by the data, therefore fitting a minimal halo or maximal spheroid<sup>2</sup>. The influence of the black hole is negligible at large radii and therefore we also do not fit for  $M_\bullet$ , but keep its value fixed.

<sup>2</sup>Comparable to the maximal disc model that is often invoked when modeling dark haloes of spiral galaxies.

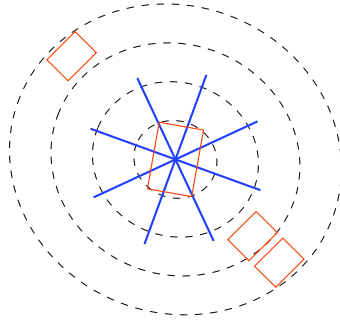


**Figure 3.10** — Overview of the datasets included in our dynamical model of NGC 3379. The dotted lines denote isophotes of the galaxy at 1, 2, 3 and  $4 R_e$ . The box in the centre denotes the central SAURON field (Emsellem et al. 2004), while the other boxes show the positions of our data at large radii. The solid lines show the orientation and extent of the long-slit data (Statler & Smecker-Hane 1999).

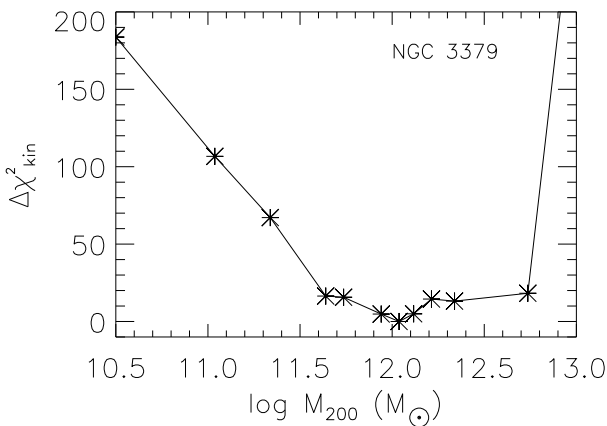


**Figure 3.11** —  $\Delta\chi^2$  levels for the Schwarzschild models we ran for NGC 3379. The only free parameter in these models was  $M_{200}$  (total halo mass). The model without dark halo is relocated at  $3 \times 10^{10} M_\odot$ , to place it within the plot.

### 3.5.2 Modelling NGC 3379 and NGC 821

NGC 3379 has a small kinematic misalignment of  $5 \pm 3^\circ$  (e.g. Statler & Smecker-Hane 1999) and shows signs of a kinematic twist (Krajnović et al. 2008), which indicate that the galaxy is not perfectly axisymmetric (see also Capaccioli et al. 1991; Statler 2001). Van den Bosch & de Zeeuw (2009) therefore constructed triaxial Schwarzschild models of this galaxy. Their best-fitting triaxial model (axis ratios  $p = 0.95$ ,  $q = 0.81$ ) is nearly face-on, with an inclination of  $\sim 40^\circ$ . This model is nearly spherical in the centre and becomes close to oblate at large radii, which is in agreement with Statler (2001) and De Lorenzi et al. (2009).

We adopt the best-fit model of van den Bosch & de Zeeuw (2009) for our halo modeling. The model has a black hole mass of  $M_{\bullet} = 4.0 \times 10^8 M_{\odot}$  and a dynamical mass-to-light ratio  $M/L_I = 2.9 M_{\odot}/L_{I,\odot}$ , which we adopt as the maximally allowed stellar mass-to-light ratio  $M_*/L$ . The stellar potential is represented by a Multi-Gaussian Expansion (MGE, Emsellem, Monnet & Bacon 1994; Cappellari 2002) model based upon *I*-band imaging<sup>3</sup>, presented by Cappellari et al. (2006). We use the same central SAURON kinematics (up to  $h_6$ ) extracted with the MILES library (see Shapiro et al. 2006; Cappellari et al. 2007; van den Bosch & de Zeeuw 2009) to cover the inner  $R_e$  of NGC 3379 and add our measure points at large radii. For extra spatial coverage, we also include the symmetrized data of the four long-slit observations of Statler & Smecker-Hane (1999) (see Figure 3.10). The large mosaic of central SAURON data provides many more kinematic constraints in the central region than the four slits. We therefore exclude the inner 20 arcsec of each slit from the fit. The planetary nebulae measurements are not based on integrated stellar light, as our SAURON and long-slit data, and therefore for consistency not included.

We use a similar procedure to construct mass models of NGC 821. This galaxy is a very flattened system (E6) and shows no signs of non-axisymmetry in its central part, even though planetary nebulae kinematics suggest twists at larger radii (Coccatto et al. 2009). Our dataset however provides no constraints on the behaviour of the velocity field at these scales. We therefore deproject this galaxy axisymmetrically, assuming an edge-on view and use the triaxial code in the axisymmetric limit. We adopt the edge-on MGE model of NGC 821 based upon ground-based *R*-band photometry<sup>4</sup> and space-based imaging with HST/WFPC2 in F814W-band, as in McDermid (2002) and Cappellari et al. (2006). We first construct a model without a dark halo, based only on kinematics (up to  $h_6$ ) of the central SAURON dataset, extracted with the MILES library (Cappellari et al. 2007). Our best fit has a stellar mass-to-light ratio of  $2.5 M_{\odot}/L_{I,\odot}$  with a black hole mass of  $M_{\bullet} = 2.1 \times 10^8 M_{\odot}$  from the  $M_{\bullet}$ - $\sigma$  relation. We then add a dark NFW halo to this model, with a fixed concentration of  $c = 10$ . The SAURON central dataset is used to cover the central part of the galaxy, while our four measurepoints at large radii are included to cover the outerparts. To avoid a possible conflict between the central SAURON data and the long-slit data of Forestell & Gebhardt (2008), we decided to not include the latter in our model, as there seem to be some deviations between the two datasets (see Figure 3.6).

<sup>3</sup>Obtained with the 1.3-m McGraw-Gill Telescope of the MDM Observatory, Kitt Peak, US.

<sup>4</sup>Obtained with the 0.9-m telescope at the Cerro Tololo Inter-American Observatory (CTIO), Chile.

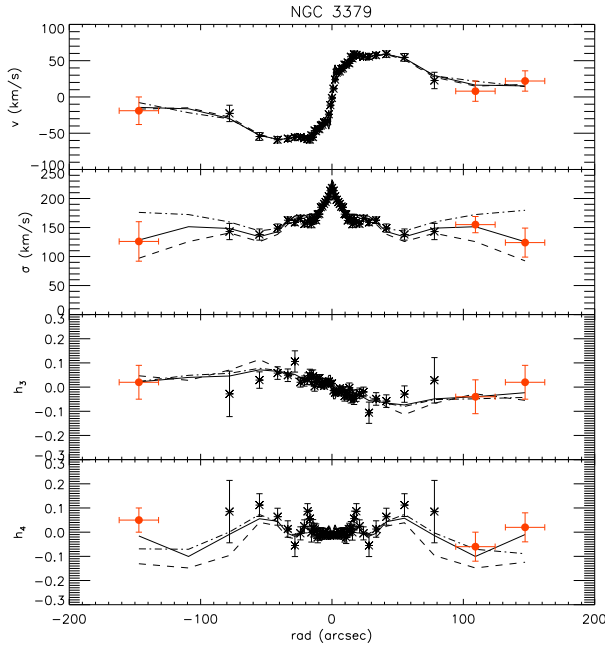


**Figure 3.12** — Best-fit model for NGC 3379 (bold line,  $M_{200} = 1.0 \times 10^{12} M_{\odot}$ ) compared to our datapoints at large radii (grey filled circles) and long-slit data on the major axis (black stars). Also indicated are a model without halo (dashed line) and a model with a heavy halo (dashed-dotted line,  $M_{200} = 5.2 \times 10^{12} M_{\odot}$ ). These models respectively underpredict and overpredict the observed velocity dispersion.

Our best fitting model for NGC 3379 requires a halo mass of  $M_{200} = 1.0 \times 10^{12} M_{\odot}$ , as compared to a total stellar mass of  $1.0 \times 10^{11} M_{\odot}$ . In Figure 3.12 we show the kinematics of our best-fit model compared to our data at large radii and the long-slit kinematics on the major axis. The fit is excellent, even for the higher order moments  $h_3$  and  $h_4$ . A model without dark halo clearly underpredicts the observed velocity dispersion and  $h_4$  outside  $1 R_e$ . For comparison also a model with a halo heavier than our best fit model is shown: here the velocity dispersion is overestimated. In Figure 3.11 we show the  $\chi^2$  values of our best fitting model. We see that with 3- $\sigma$  confidence,  $M_{200} = 1.0^{+0.4}_{-0.3} \times 10^{12} M_{\odot}$  under the assumptions mentioned above, while a model without dark halo is strongly excluded.

We obtain similar results for NGC 821, where we also exclude the absence of a dark halo (see Figure 3.13). The halo mass in our best-fit model is  $M_{200} = 6.5^{+1.0}_{-4.3} \times 10^{11} M_{\odot}$ , while the total stellar mass is  $1.1 \times 10^{11} M_{\odot}$ . The kinematics of the fit compared to the observed kinematics are shown in Figure 3.14, where for



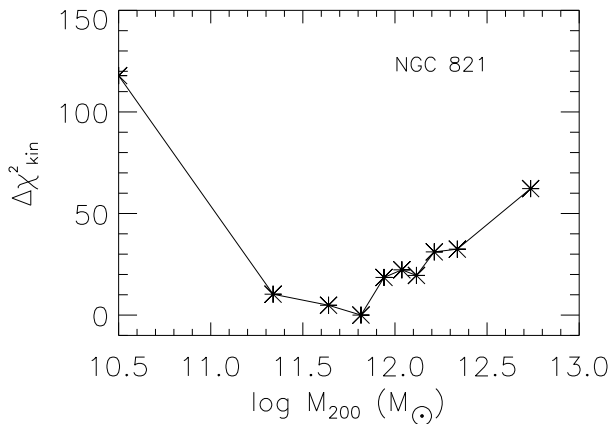


**Figure 3.13** — Same as Figure 3.11, but now for NGC 821.

comparison also a model without a dark halo and a model with a too massive halo are shown.

We conclude that dark matter is present both in NGC 3379 and NGC 821. Even within  $1 R_e$  in NGC 3379, 8 per cent of the total mass is dark, while at  $4 R_e$  this fraction has increased to 34 per cent. NGC 821 is more dark matter dominated, with a dark matter fraction of already 18 per cent within  $1 R_e$ , increasing to 49 per cent within  $4 R_e$ . Note however that these values are based on minimal halo assumptions, and therefore should be seen as lower limits. Also, varying halo shape and profile can cause these fractions to change, they therefore should be strictly seen as indicative.

### 3.5.3 Orbital structure

In the top panels of Figure 3.15 we show the orbital anisotropy in our dynamical models of NGC 3379 and NGC 821. We characterize the orbital anisotropy as

$$\beta_r = 1 - \frac{\sigma_\phi^2 + \sigma_\theta^2}{2\sigma_r^2}, \quad (3.9)$$

with  $(r, \theta, \phi)$  standard spherical coordinates. Our best-fit model of NGC 3379 is nearly isotropic within  $2 R_e$ , and at larger radii the radial anisotropy increases. Our best-fit model of NGC 821 is already mildly radially anisotropic in the central regions, but also shows a small increase with radius. Cappellari et al. (2007) presented orbital anisotropy values for both NGC 3379 and NGC 821 from axisymmetric models, based on the same central SAURON data and MGE models

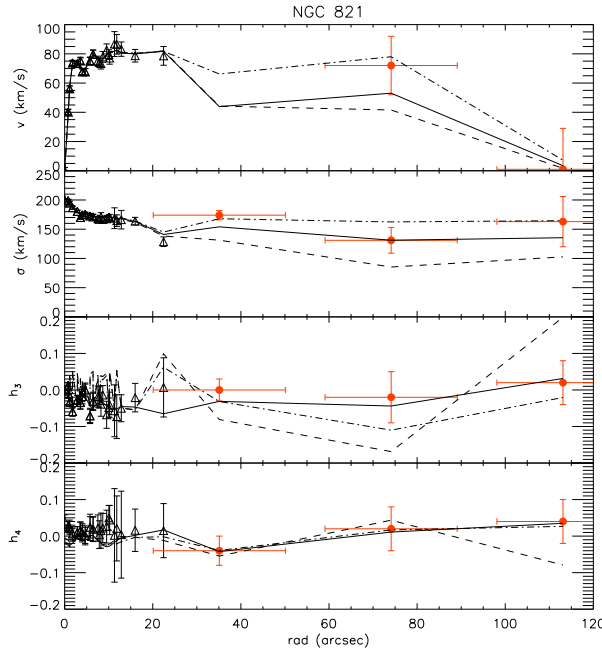


**Figure 3.14** — Best-fit model for NGC 821 (bold line,  $M_{200} = 6.5 \times 10^{11} M_{\odot}$ ) compared to our datapoints at large radii (grey filled circles) and the central SAURON data (open triangles). The dashed line indicates a model without halo and the dashed-dotted line a model with a too heavy halo ( $M_{200} = 5.5 \times 10^{12} M_{\odot}$ ).

as we use in this paper. Our central anisotropy values are consistent with theirs for both galaxies. Since Cappellari et al. (2007) used a different, independent modeling code, this agreement gives confidence in the robustness of the anisotropy parameters presented here.

Within  $1 R_e$ , the orbital anisotropy changes only marginally between our models with and without halo, consistent with the findings of Thomas et al. (2009). At larger radii the radial anisotropy increases, and the increase is smaller for models with heavier haloes. This is contrary to what is seen in spherical models. In order to fit the observed mildly declining or constant velocity dispersion profile without invoking extra dark matter at large radii, the orbits have to be tangentially anisotropic, while adding a dark halo results in more radially anisotropic orbits (e.g. Richstone & Tremaine 1984; Dekel et al. 2005; de Lorenzi et al. 2009).

The detailed kinematics in the inner part of the galaxy together with our observed positive  $h_4$  in the outer parts already tightly constrain the fraction of box and tube orbits in our triaxial potential, and therefore the anisotropy. Box orbits

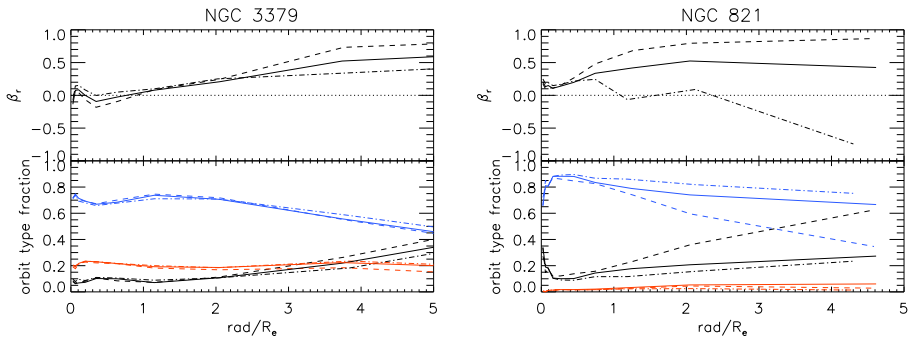


**Figure 3.15** — Orbital structure in NGC 3379 (left) and NGC 821 (right). Top panel: velocity anisotropy  $\beta_r$  as a function of radius (see Equation 3.9). The lines are as in Figures 3.12 and 3.14, with the solid line for our best-fit model, the dashed line for the model without halo and the dashed-dotted line for the model with the too heavy halo. Bottom panel: fraction of orbit types as a function of radius for the models of the top panel. Blue lines denote the fractions of short axis tubes, red the fractions of long axis tubes and black the fractions of box orbits. See the colour supplement for a colour version of this figure.

have no net rotation, and contribute to the radial anisotropy of the system, requiring  $h_4 > 0$ . For tube orbits to reproduce the observed nearly zero mean rotation at large radii, they have to be counter-rotating, increasing the velocity dispersion. However, they would at the same time increase the tangential anisotropy and therefore yield  $h_4 < 0$ . Since we observe a positive  $h_4$  at large radii, box orbits are expected to contribute significantly to the orbital structure in our models without dark matter, as confirmed in Figure 3.15. As a result, the models without dark halo are strongly radial anisotropic at large radii. Adding a spherical dark matter halo to the system makes the gravitational potential less triaxial. This will decrease the phase space volume of box orbits and naturally results in a larger population of tube orbits (Hunter & de Zeeuw 1992). The radial anisotropy of the system will decrease, as is illustrated in Figure 3.15. This decrease is more pronounced in NGC 821 than in NGC 3379, since our best-fit model of NGC 821 is more dark matter dominated than our NGC 3379 model.

### 3.5.4 $Mg\ b - V_{\text{esc}}$ relation

We here investigate the connection between the stellar populations and the mass distribution of the galaxy. Franx & Illingworth (1990) showed that there is a tight relation between the local colour (tracing metallicity) and the local escape velocity  $V_{\text{esc}}$  (tracing the gravitational potential  $\Phi$ ) in early-type galaxies, with  $V_{\text{esc}}$  given

by:

$$V_{\text{esc}} = \sqrt{2|\Phi|}. \quad (3.10)$$

This relation was confirmed by Davies et al. (1993), who used Mg 2 as a tracer for metallicity. Scott et al. (2009) find correlations between line strength indices and  $V_{\text{esc}}$  for the early-type galaxies in the SAURON sample, based on measurements within  $\sim 1 R_e$ . They also show that for Mg  $b$  this relation does not only hold locally in one galaxy, but is also a global relation between different galaxies.

With our data at large radii we can now investigate the behaviour of this relation out to  $4 R_e$ . We determine for our best-fit model of NGC 3379 the contribution to the gravitational potential of the dark halo using Equation 3.6. The contribution of the stellar mass is inferred from the MGE model, following the formularium in the appendix of Cappellari et al. (2002) and the black hole is included as a Plummer potential. We plot our result in Figure 3.16, and find that the observed relation within  $1 R_e$  continues out to at least  $4 R_e$ . The influence of the dark halo on the Mg  $b$  -  $V_{\text{esc}}$  relation becomes clear when comparing our results to a model without a dark halo, where the only contribution to the potential comes from the MGE model and the black hole (open symbols in Figure 3.16). Not only is there an offset in  $V_{\text{esc}}$  with respect to the model with the dark halo, but also the slope changes, an effect which was also noted by Franx & Illingworth (1990). The addition of extra mass at larger radii by the dark halo deepens the potential well, which means that even particles in the centre of the galaxy will need a larger  $V_{\text{esc}}$  to climb out of this well, causing a shift in  $V_{\text{esc}}$  at all radii. However, particles in the outskirts of the galaxy are relatively more affected by the addition of the dark halo than particles in the more central regions: if the halo had not been present, escaping from the potential well at large radii would have been relatively easy. Therefore, the shift in  $V_{\text{esc}}$  is larger at larger radii, something that is also illustrated by Figure 3.16. The net result is a change in slope. We find that the slope of the Mg  $b$  -  $V_{\text{esc}}$  relation in NGC 3379 changes in logscale from 0.31 to 0.46, when taking the dark halo into account. If instead of considering the infinite halo mass of the NFW profile we only take the contribution of the halo within  $r_{200}$  into account when calculating the gravitational potential, the slope becomes 0.43 in logscale.

We note that in both the models with and without halo, there is a *local* relation between Mg  $b$  and  $V_{\text{esc}}$ . However, when looking at a larger sample of galaxies and studying the *global* Mg  $b$  -  $V_{\text{esc}}$  relation the contribution of the halo to the potential should be taken into account to interpret the slopes, since the relative contribution

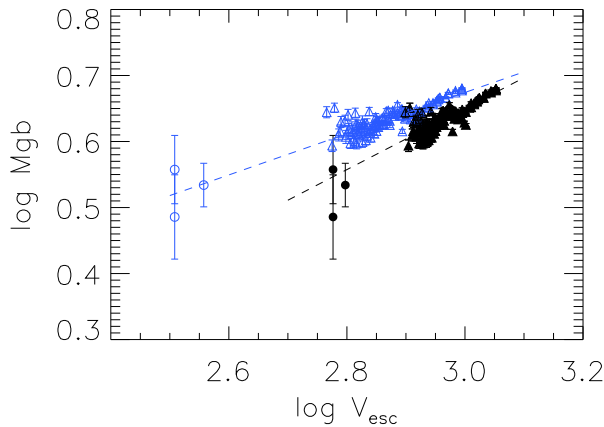


**Figure 3.16** —  $\text{Mg } b$  (in  $\text{\AA}$ ) versus local escape velocity  $V_{\text{esc}}$  (km/s) in NGC 3379. Black filled triangles denote points from the central SAURON data, while the black filled dots are our large radii data. Overplotted is the gradient fitted to the central dataset. With open symbols (in grey) we show the  $\text{Mg } b - V_{\text{esc}}$  relation calculated from our model without a halo. This relation is offset from our best-fit model and also has a different slope, illustrating the influence of the dark matter.

of the dark matter to the potential compared to the luminous one may vary from galaxy to galaxy, e.g. depending on galaxy mass or environment.

### 3.6 Summary and conclusion

We used the SAURON IFU as a “photon collector” to obtain stellar absorption line kinematics and line strengths out to four effective radii in the early-type galaxies NGC 3379 and NGC 821. By co-adding the individual spectra of each lenslet into one spectrum for each observed field, we were able to obtain sufficient signal-to-noise in the outskirts of these galaxies, which are too faint to observe with traditional long-slit spectroscopy. The stellar velocity profiles are measured up to the fourth Gauss-Hermite moment ( $h_4$ ), which allows us to break the mass-anisotropy degeneracy when constructing dynamical models of our galaxies. The kinematics show a smooth continuation of the profiles measured within 1-2  $R_e$  with SAURON and long-slit spectroscopy, and are consistent with planetary nebulae kinematics. The line strengths also show a continuation of the gradients observed within 1  $R_e$ , although our Fe5015 measurements probably suffer from variations in the continuum shape. The stellar halo population is old and metal-poor. The continuation of the line strength gradients and the  $\text{Mg } b - V_{\text{esc}}$  relation out to at least 4  $R_e$  provides constraints for the star formation and merger history of early-type galaxies (e.g.

Hopkins et al. 2009a; Hopkins et al. 2009b; Spolaor et al. 2009).

Constructing dynamical orbit-based models, we show that even assuming a maximal stellar contribution, both NGC 3379 and NGC 821 require a dark halo to fit the observed kinematics. We parametrised the halo contribution with a spherical NFW profile, fixing the concentration to  $c = 10$ . We therefore cannot give a definite number for the precise mass content, shape and anisotropy of the halo. Varying  $c$  in our halo profile does not have a large effect on the fitted dark matter content, as an increase of  $c$  will be accompanied by a decrease in  $M_{200}$ , as the dynamical models constrain the density inside the region for which kinematics are available. Only with data at even larger radii (preferably out to  $\sim 100 R_e$ , accessible with e.g. weak gravitational lensing or satellites) we would be able to break the degeneracy between  $c$  and  $M_{200}$ . In that sense, our results should be viewed as an estimate of the minimal contribution of the dark halo to the total mass budget in the galaxy, and we then see that even at small radii (within  $1 R_e$ ), the dark matter is already responsible for 10 - 20 per cent of the total mass. These percentages will increase if we relax the minimal halo assumption, but we then need reliable measurements of the stellar mass-to-light ratio and its potential variation with radius. With better spatial coverage of the galaxy, either by mosaicing or by employing larger IFUs (such as VIRUS-P and in the future MUSE) and combining the so-obtained stellar kinematics with other datasets tracing dark matter at different regimes (e.g. H I discs or rings, hot gas, gravitational lensing and/or discrete tracers such as planetary nebulae) we will be able to build more sophisticated dynamical models, to explore the shape and mass of the dark haloes around early-type galaxies.

## Acknowledgements

It is a pleasure to thank Eveline van Scherpenzeel, Chris Benn and the ING staff for support on La Palma. We gratefully acknowledge Koen Kuijken, Aaron Romanowsky and Marc Sarzi for fruitful discussions. We also thank Richard Wilman for supplying us with the data necessary to make the superflat for NGC 3379 and Lodovico Coccato for sending us the planetary nebulae kinematic profiles of NGC 821 and NGC 3379. We are grateful to the referee, Elena Terlevich, for constructive comments which improved the presentation of the paper.

This research was supported by the Netherlands Organization of Scientific Research (NWO) through grants 614.000.426 and 614.000.301. AW acknowledges The Leids Kerkhoven-Bosscha Fonds for contributing to working visits, as well as the hospitality of ESO, the University of Oxford, l'Observatoire de Lyon and

---

the Institute for Advanced Study. MC acknowledges support from a PPARC Advanced Fellowship (PP/D005574/1). GvdV acknowledges support through Hubble Fellowship grant HST-HF-01202.01-A awarded by the Space Telescope Science Institute, which is operated by the Association of Universities for Research in Astronomy, Inc., for NASA, under contract NAS 5-26555.

The SAURON observations were obtained at the William Herschel Telescope, operated by the Isaac Newton Group in the Spanish Observatorio del Roque de los Muchachos of the Instituto de Astrofísica de Canarias.





---

## Chapter 4

---

# Spectroscopic mapping of the stellar and dark halo of the early-type galaxy NGC 2549

We obtain the stellar line-of-sight velocity distribution and absorption line strengths in the early-type edge-on galaxy NGC 2549 with the integral-field spectrograph PPAK. Combining four observed fields, we obtain a map out to more than four effective radii, probing the faint outskirts of this galaxy.

We find that NGC 2549 continues to rotate in a disc-like structure out to the edge of our observed field. From the kinematics and dynamical modeling, we infer that a second disc-like component is present, embedded in a larger, thicker disc. We use stellar population models to obtain age, metallicity and stellar mass-to-light ratios, based on stellar absorption line strength measurements. For the first time we map all these three quantities over the total field-of-view, finding again evidence for a flattened, young metal-rich component in the central part of the galaxy. The stellar halo population has an age of  $\sim 9$  Gyr, and we observe a change in metallicity from  $[Z/H] = 0.2$  to  $[Z/H] = -0.4$  from the centre to the edge of the observed field.

Schwarzschild dynamical models indicate that NGC 2549 is surrounded by a dark matter halo. Within one  $R_e$ , at least 16 per cent of the total mass is dark. At  $5 R_e$ , this fraction has increased to 63 per cent. Applying anisotropic Jeans modeling to the observed kinematics supports this conclusion. We note however that these fractions are lower limits. If we incorporate in our models the stellar mass-to-light ratio resulting from stellar population modeling, the dark matter fraction within  $1 R_e$  is already 65 per cent, and increases to 95 per cent at  $5 R_e$ .

Anne-Marie Weijmans, Joris Gerssen, Michele Cappellari, P. Tim de Zeeuw,  
Jesús Falcón-Barroso, Harald Kuntschner & Remco C.E. van den Bosch  
To be submitted to *Monthly Notices of the Royal Astronomical Society*

## 4.1 Introduction

The outskirts of galaxies are still mostly unexplored territory, yet they harbour important clues for the formation history of these objects. Outside a few half-light or effective radii ( $R_e$ ), dark matter starts to dominate over the luminous content of the galaxy. Dark haloes formed the gravitational potential wells in which gas could cool and form stars (e.g. Springel et al. 2005). Their mass and shape, together with stellar populations and their change in e.g. age and metallicity over large radii, constrain the starformation and assembly history of galaxies (e.g. Hopkins et al. 2009b). In addition, outer stellar substructures, such as tails, are tracers of past merger events (e.g. Schweizer 1986), and numerical simulations needed to interpret these features are generally more robust and less resolution dependent for large scale outer structures, than for central, smaller components.

It was recently shown by Weijmans et al. (2009a) that using integral-field units (IFUs) as photon collectors, it is possible to observe the stellar light in the faint outskirts of galaxies. The authors used the SAURON IFU (Bacon et al. 2001) to obtain stellar velocity profiles and absorption line strengths out to 3-4  $R_e$  in two early-type galaxies. Because of the large collecting area of the IFU compared to traditional long-slit spectrography, and the relatively high throughput, the line-of-sight velocity dispersion (LOSVD) could be measured up to the fourth Gauss-Hermite moment  $h_4$ . This allowed breaking the mass-anisotropy degeneracy by means of constructing mass models. These models showed that dark matter haloes surround their observed galaxies, which out to 4  $R_e$  make up 30 - 50 per cent of the total mass. In addition, they found that the line strength gradients observed in the central  $R_e$  of the galaxy (e.g. Kuntschner et al. 2006), continue out to at least 4  $R_e$ . The same behaviour was seen for the well-studied  $Mg\ b$ - $V_{\text{esc}}$  relation (e.g. Davies, Sadler & Peletier 1993; Scott et al. 2009). The stellar halo population was found to be old and metal-poor.

Because Weijmans et al. (2009a) could only sample the major axis of their targets, they did not construct fully general mass models, but assumed spherical dark haloes and maximal spheroids<sup>1</sup>. To allow modeling of more general halo profiles, more spatial coverage would be needed, while to relax the assumption of a maximal spheroid, a better handle of the stellar mass-to-light ratio ( $M_*/L$ ) is required. We therefore turned to the PPAK integral-field unit (Kelz et al. 2006), which has a three times larger field-of-view and a longer wavelength coverage than SAURON. This last property allows for the measurement of more line

---

<sup>1</sup>Comparable to the maximal disc model that is often invoked for spiral galaxies, adopting the maximal  $M_*/L$  allowed by the data.

Morphological Type	S0
$M_B$ (mag)	-19.44
Effective $B - V$ (mag)	0.95
Photometric PA ( $^\circ$ )	1
Distance modulus (mag)	30.45
Distance (Mpc)	12.3
Distance scale (pc arcsec $^{-1}$ )	60
Effective radius (arcsec)	20
Systemic velocity (km/s)	1070

**Table 4.1** — Properties of NGC 2549. Magnitude and colour are taken from the Lyon/Meudon Extra galactic Database (LEDA). The distance modulus was derived from surface brightness fluctuation measurements by Tonry et al. (2001). Note that 0.06 mag is subtracted to adjust to the Cepheid zeropoint of Freedman et al. (2001); see Mei et al. (2005), section 3.3, for a discussion. The effective radius and position angle are taken from Cappellari et al. (2007).

strength indices, needed for an accurate determination of  $M_*/L$  as a function of radius. Although the spaxel size of PPAK is larger than that of SAURON (2.7 arcsec versus 0.94 arcsec), this loss in spatial resolution is not important when observing the outer parts of galaxies, where binning of spaxels is needed to obtain sufficient signal-to-noise ( $S/N$ ) to measure kinematics and line strengths. For these faint observations it even helps to have large apertures, as the readnoise per collecting area is smaller.

We chose to observe the early-type field galaxy NGC 2549 out to  $5 R_e$  with the PPAK IFU, to obtain the properties of its halo and stellar halo population. This isolated galaxy shows no signs of interactions and has an edge-on orientation, which simplifies mass modeling. NGC 2549 was also observed out to  $\sim 1 R_e$  as part of the SAURON survey (de Zeeuw et al. 2002), so that in the central part of our mass models, the PPAK data can be replaced by the higher resolution SAURON data. SAURON maps of the stellar kinematics, ionised gas, as well as line strengths were presented by Emsellem et al. (2004), Sarzi et al. (2006) and Kuntschner et al. (2006), respectively. Based on its stellar kinematic maps, NGC 2549 was classified as a fast rotator (Emsellem et al. 2007). Recently, Krajinović et al. (2009) modeled this galaxy combining SAURON and  $K$ -band NIFS integral-field kinematics, to measure the mass of the supermassive black hole residing in the centre of NGC 2549. This galaxy was not detected in atomic gas ( $M_{\text{HI}} < 2.0 \times 10^6 M_\odot$ , Morganti et al. 2006) and kinematics of globular clusters or planetary nebulae have not been observed. This makes our observations of the

Field-of-view (arcsec $\times$ arcsec)	74 $\times$ 64
Fiber diameter (arcsec)	2.7
Number of science fibers	331
Number of sky fibers	36
Number of calibration fibers	15
Filling factor (per cent)	60

**Table 4.2** — Properties of the PMASS PPAK spectrograph at the 3.5-m telescope at Calar Alto (see also Kelz et al. 2006).

stellar kinematics at large radii even more crucial, as no other tracer is available to constrain the dark halo. Some basic properties of NGC 2549 are summarized in Table 4.1.

We present our observations and data reduction in section 4.2. In section 4.3 we describe the extraction of the stellar and ionised gas kinematics, as well as the line strength measurements. Section 4.4 is devoted to interpretation of the line strength gradients and modeling of the stellar halo population. In section 4.5 we construct mass models of NGC 2549 and determine the properties of its dark halo. Finally, in section 4.6 we summarize and discuss our results.

## 4.2 Observations and data reduction

We observed the early-type galaxy NGC 2549 with the wide integral-field unit PPAK at the 3.5-m telescope at Calar Alto (Kelz et al. 2006, see also Table 4.2) in service mode. We used the V600 grating with a rotation of +144.4 degrees, so that it was centred on the Mg *b* absorption feature around 5200 Å. The hexagonal field-of-view (FoV) of PPAK was centred at 1.0 and at 3.2  $R_e$  on the major axis of the galaxy, on opposite sides of the nucleus (see Figure 4.1). The FoV however has dimensions of 74 arcsec  $\times$  64 arcsec, and therefore the outer observations reach out to 5  $R_e$ , probing the presumably dark matter dominated outskirts of the galaxy.

The observations were split in 1800 second individual exposures. Each exposure was bracketed by a calibration arc (HeHg + ThAr) and a trace continuum exposure (cont+cont). In addition we took a total of 28 blank sky exposures of 900 seconds, before or after each galaxy exposure<sup>2</sup>. These sky fields were used for sky subtraction, which is a critical aspect in our analysis: because we observe at

<sup>2</sup>In practice, this resulted in an observing sequence of sky - galaxy -galaxy -sky etc., such that each galaxy exposure borders at least one sky exposure.

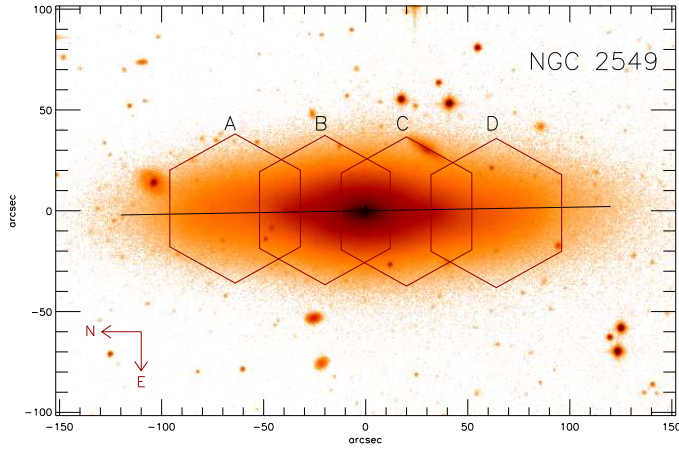


**Figure 4.1** — Positions of our observed fields in NGC 2549 (red hexagonals), placed on the major axis of the galaxy (black line). The underlying  $V$ -band image was obtained with the 1.3-m McGraw-Hill Telescope at MDM Observatory.

very low surface brightness, our spectra are skydominated (see also Figure 4.2). PPAKs skyfibers are placed around the main fields at a distance of 1.2 arcmin from the central fiber and consequently they still observe faint galaxy light, and therefore do not provide an accurate enough sky subtraction for our observations. Also, the skyfields can be combined in a so-called superflat, to allow accurate flatfielding. A summary of our observations can be found in Table 4.3.

The data were reduced in IDL using the reduction package P3D (Sandin et al. 2009). This package performs the following steps. It creates and subtracts a master bias frame. It traces the location of each spectrum on the detector using the trace continuum exposures. The spectra in all science exposures are extracted by collapsing cross-dispersion profiles, centred on each trace position, to 1D spectra. As the spectra are fairly well separated on the detector (Kelz et al. 2006), the level of cross-talk between adjacent spectra is a few percent only. Hence we make no attempt to correct for cross-talk and simply apply a tophat weighting scheme when collapsing the spectra to 1D. Stacking of spectra to increase the  $S/N$  level in our subsequent analysis renders painstaking cross-talk correction unnecessary.

The continuum trace exposures and arclamp exposure are extracted similarly to the science exposures. The summed fluxes along each extracted trace spectrum are used to make a correction for the relative fiber-to-fiber throughput. In the extracted arclamp spectra the measured centroids of seven or eight He and Hg lines are fitted with a low order polynomial as a function of intrinsic wavelength

Field	$R/R_e$	$T_{\text{exp}}$ (hr)	$\mu_V$ (mag/arcsec <sup>2</sup> )
A	3.2	5.5	22.8
B	1.0	4.0	20.2
C	1.0	3.5	20.2
D	3.2	4.0	22.8

**Table 4.3** — Properties of our observed fields in NGC 2549 (see Figure 4.1). The surface brightness  $\mu_V$  in the centre of the pointing is calculated from the MDM images, and can be compared to the sky surface brightness, which at Calar Alto in  $V$ -band is about 22.0 mag/arcsec<sup>2</sup> in optimal conditions (Sánchez et al. 2007).

to derive the dispersion solution. All science spectra are rebinned onto the same wavelength scale using their individual, best-fit dispersion solutions.

We correct the different sky levels between exposures by normalising them using a ‘superflat’ field. The superflat is created by first median combining our 27 blank sky exposures into a single frame. A median sky spectrum is generated from the combined frame and smoothed by fitting it with a 4th order polynomial. The combined frame is divided by the smoothed sky spectrum to create the superflat.

After superflat fielding, the datacubes were imported in the XSAURON datareduction package, that was developed for the SAURON project (Bacon et al. 2001). We used this software to remove cosmic rays and to flux calibrate the spectra. For this last step, we used nightly observed spectra of the standard fluxstar G191-B2B. The spectra of the individual cubes were then resampled and interpolated on a rectangular grid and merged in a final datacube. We set the spatial resolution to 3 arcsec, which roughly corresponds to the distance between fiber centra. During the datareduction, the sky was not subtracted from the galaxy spectra, but was removed in a later stage, when extracting the stellar kinematics (see Section 4.3.1).

### 4.3 Extraction of kinematics and line strengths

To study the dark and stellar content of the halo of NGC 2549, we need to extract the stellar kinematics and line strengths from the spectra. To ensure that we have sufficient signal in each spectrum to reliably measure the LOSVD up to at least the fourth Gauss-Hermite moment  $h_4$ , we binned the PPAK spectra, using a Voronoi tessellation method (Cappellari & Copin 2003). We aimed for a minimal  $S/N$  of 50 for each bin. However, since the sky was not subtracted from our spectra, estimating a priori the  $S/N$  in the galaxy for each spectrum was not possible. We therefore prepared a second cube of PPAK spectra, extracted and reduced in exactly the same way as the original cube, except that we subtracted the sky based on the skyfibers that were positioned east and west of the main FoV, avoiding the skyfibers that fell directly in the galaxy. We binned the spectra based on the

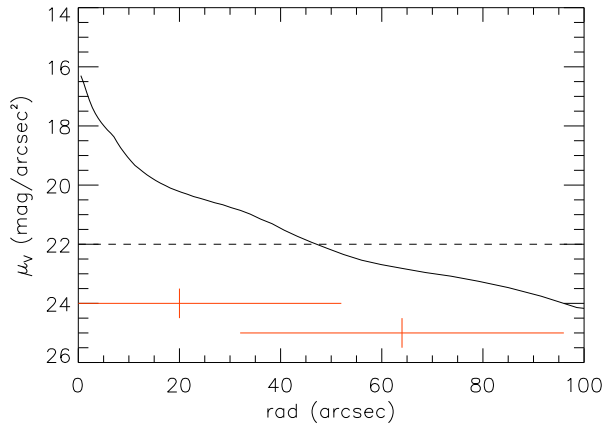


**Figure 4.2** — Surface brightness in  $V$ -band as a function of radius in NGC 2549. The profile is obtained from MDM  $V$ -band imaging. The two solid horizontal lines indicate the extent of the PPAK FoV for our pointings (see also Figure 4.1), with the inner one centred at  $1 R_e$  (fields B+C) and the outer one at  $3.2 R_e$  (fields A+D). The dashed line indicates the surface brightness of the sky.

flux in this skysubtracted datacube, and continued our analysis with the original cube that still contained the sky. After extracting the kinematics, we checked that indeed the required minimal  $S/N$  was reached.

### 4.3.1 Stellar kinematics

We used the penalized Pixel Fitting<sup>3</sup> (pPXF) routine of Cappellari & Emsellem (2004) to extract the stellar kinematics from our spectra. pPXF convolves an optimal stellar template with the LOSVD, to find the best fit to the observed spectrum. During this fit, emission and sky lines are masked and therefore not included in the fit. The optimal stellar template is composed by pPXF for each bin as a linear combination of stellar spectra from a representative library. For this, we used the MILES library of 945 stars from Sánchez-Blázquez et al. (2006). We first co-added all the PPAK spectra of NGC 2549 together and then fitted this spectrum with pPXF, using the full MILES library to supply templates. The optimal template consisted of 51 MILES stars, and these stars were subsequently fed to pPXF as template library when fitting the binned spectra. We included additive polynomials to allow for changes in line strengths. Errors are obtained by a Monte Carlo simulation, by measuring the kinematics from many realisations of the input spectra, on which we added noise.

<sup>3</sup>available from <http://www-astro.physics.ox.ac.uk/~mxc/idl/#ppxf>



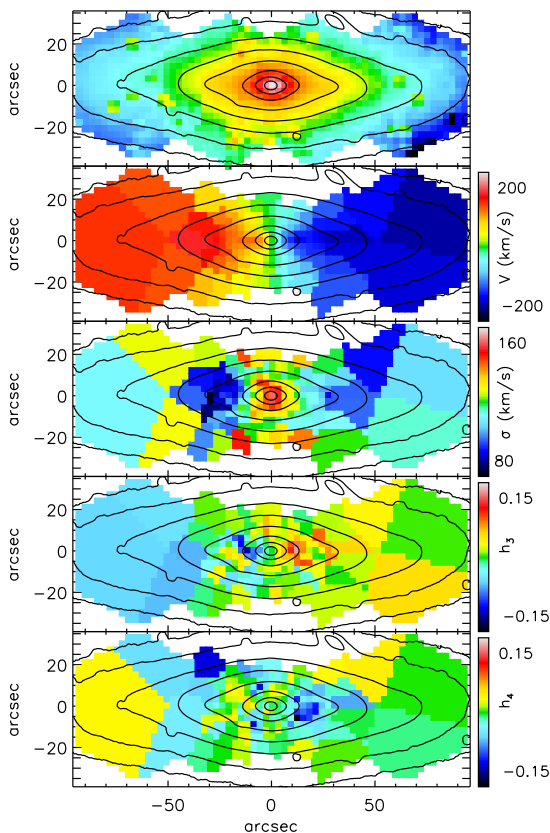


**Figure 4.3** — Stellar kinematics extracted from the PPAK spectra of NGC 2549. From top to bottom: total flux, velocity, velocity dispersion,  $h_3$  and  $h_4$ . The maps are orientated such that North is to the left and East is down. For a colour version of this plot, see the colour supplement.

By coadding the spectra of each blank sky exposure, we obtained sky spectra that we included as templates in pPXF. Since our spectra in the outer parts of the galaxy are very sky dominated, this way we obtain a more accurate sky subtraction, allowing for subtle sky variations. This procedure was introduced in Weijmans et al. (2009a) to fit sky dominated spectra, and we refer the reader to this paper for more details.

The LOSVD, parametrized by mean velocity  $V$ , velocity dispersion  $\sigma$  and the Gauss-Hermite moments  $h_3$  and  $h_4$  is shown in Figure 4.3. The spectra on the minor axis at the edge of the observed field had a somewhat deviant continuum shape around the  $H\beta$  absorption line, and we therefore removed these bins from the maps and forthcoming analysis. We fitted the LOSVD up to the 6th moment, but since  $h_5$  and  $h_6$  consisted mostly of noise, we did not include them in the subsequent analysis and modeling of the stellar kinematics, and therefore they are not shown here. NGC 2549 displays regular, disc-like rotation out to at least  $4 R_e$ ,



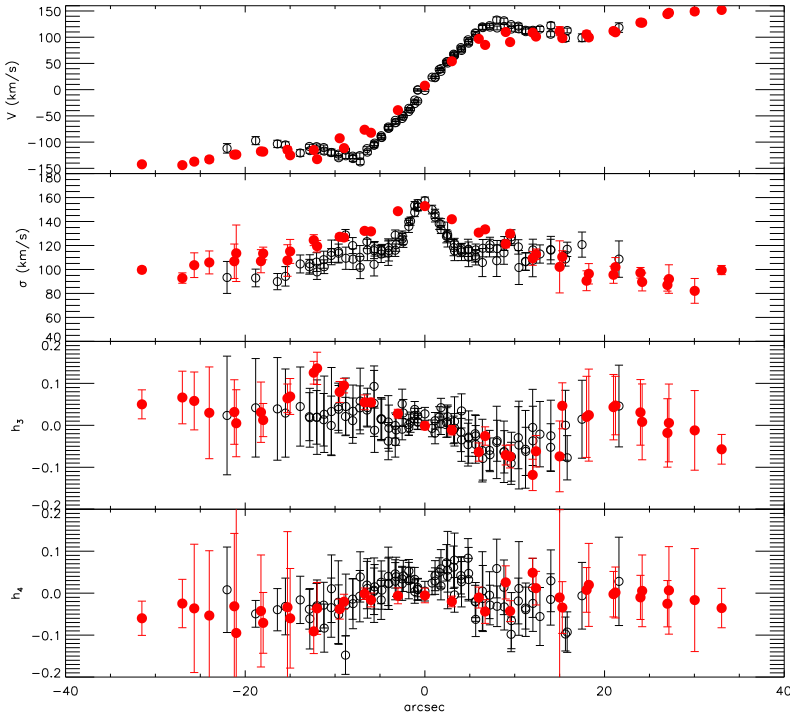


**Figure 4.4** — Comparison between the PPAK (solid black dots) and SAURON (open grey circles) kinematics, along the major axis of NGC 2549. Observed errors in the PPAK data decrease at larger radii, as here more spectra are combined in single bins, to increase the total  $S/N$ .

while the velocity dispersion shows a drop of approximately  $30 \text{ km s}^{-1}$  around 20 arcsec accompanied by a rise around 30 arcsec on the major axis, which could point to a cold disc embedded in a larger disc or bulge. Krajnović et al. (2008) also found two disc-like rotating components in this galaxy based on harmonic decomposition of its SAURON velocity map. They place the second component at 13 arcsec.

In Figure 4.4 we compare the stellar kinematics obtained with PPAK with the higher resolution SAURON kinematics in the central part of the galaxy. The SAURON kinematics of NGC 2549 were originally presented by Emsellem et al. (2004), but re-extracted with the MILES library (see Cappellari et al. 2007; Krajnović et al. 2009). Although the observed velocity,  $h_3$  and  $h_4$  agree between the two datasets, the PPAK data show a slightly higher velocity dispersion than the SAURON data. However, due to differences in sampling and spaxel size it is not straightforward to compare these values directly.

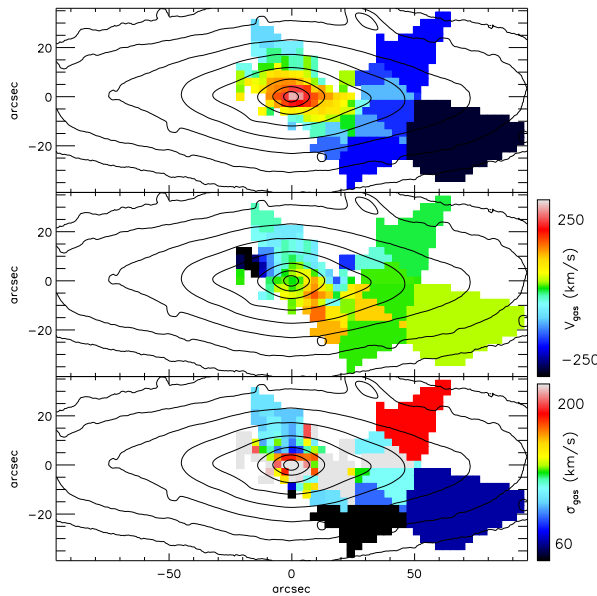


**Figure 4.5** — Gas kinematics of NGC 2549, measured from [O III]. From top to bottom: flux, velocity and velocity dispersion. Only bins with amplitude-to-noise  $A/N > 4$  are shown. Maps are orientated as in Figure 4.3. See the colour supplement for a colour version of this figure.

### 4.3.2 Ionised gas

There is some ionised gas present in NGC 2549, and emission line regions (He II,  $H\beta$ , [O III], [N I]) were masked during the extraction of the stellar kinematics. To determine the gas content and kinematics, we use the Gas AND Absorption Line Fitting<sup>4</sup> (GANDALF) routine described by Sarzi et al. (2006). GANDALF treats the emission lines as additional Gaussian templates and solves for their velocities and dispersion in combination with a stellar template convolved with the best fitting LOSVD found by pPXF. Multiplicative polynomials were included to fit the shape of the continuum. Since [O III] is the strongest emission line, we first fitted this doublet line, while keeping the other lines masked. We subsequently fitted all emission lines simultaneously, but kept their kinematics fixed to the [O III] kinematics. The skylines were masked during this procedure. We found no evidence for He II and [N I] emission, and only a few spurious detections of  $H\beta$ . [O III] was clearly detected in the inner part of the galaxy, and the [O III] gas maps are presented in Figure 4.5. The morphology and kinematics of the [O III] gas agree

<sup>4</sup>available from [http://star-www.herts.ac.uk/~sarzi/PaperV\\_nutshell](http://star-www.herts.ac.uk/~sarzi/PaperV_nutshell)

Index	Central bandpass (Å)	Blue continuum (Å)	Red continuum (Å)	Applied offsets (Å)
Fe4383	4369.125 - 4420.375	4359.125 - 4370.375	4442.875 - 4455.375	0.46 ± 0.05
Ca4455	4452.125 - 4474.625	4445.875 - 4454.625	4477.175 - 4492.125	0.36 ± 0.02
Fe4531	4514.125 - 4559.250	4504.250 - 4514.250	4560.500 - 4579.250	0.07 ± 0.03
C <sub>2</sub> 4668	4634.000 - 4720.250	4611.500 - 4630.250	4742.750 - 4756.500	-0.23 ± 0.05
H $\beta$	4847.875 - 4876.625	4827.875 - 4847.875	4876.625 - 4891.625	-0.09 ± 0.02
Fe5015	4977.750 - 5054.000	4946.500 - 4977.750	5054.000 - 5065.250	0.40 ± 0.04
Mg <i>b</i>	5160.125 - 5192.625	5142.625 - 5161.375	5191.375 - 5206.375	0.03 ± 0.02
Fe5270	5245.650 - 5285.650	5233.150 - 5248.150	5285.650 - 5318.150	0.07 ± 0.02
Fe5335	5312.125 - 5352.125	5304.625 - 5315.875	5353.375 - 5363.375	-0.04 ± 0.02
Fe5406	5387.500 - 5415.000	5376.250 - 5387.500	5415.000 - 5425.000	-0.07 ± 0.02
Fe5709	5696.625 - 5720.375	5672.875 - 5696.625	5722.875 - 5736.625	0.05 ± 0.01

**Table 4.4** — Bandpass definitions of line strength indices (Trager et al. 1998), and offsets to the Lick/IDS spectrum from the MILES library.

with the SAURON results from Sarzi et al. (2006). The gas lies in a wide filament stretching from the Northwest to the Southeast in the galaxy, and is kinematically misaligned from the stellar rotation axis.

### 4.3.3 Line strength measurements

The relatively long wavelength coverage of PPAK (4300 - 5800 Å) allows us to measure a variety of absorption line strengths, such as H $\beta$ , Mg *b* and various Fe indices. These indices are summarized in Table 4.4, with definitions taken from Trager et al. (1998). We adopt the procedure of Kuntschner et al. (2006) to measure the indices. We first removed the observed [O III] gas emission with an amplitude-to-noise ratio  $A/N > 4$  from our spectra, and calibrated to the Lick/IDS system by broadening the spectra to the wavelength-dependent instrumental resolution of the Lick spectra (Worthey & Ottaviani 1997). The observed line strengths were corrected for broadening caused by the LOSVD.

Since the Lick spectra are not flux-calibrated, we need to apply offsets to our measured indices to conform to the Lick/IDS system. To determine these offsets, we had observed 11 different standard stars from the MILES library with PPAK during the same run. Each star was observed 2-3 times. In Figure 4.6, we show the line strength measurements of these stars, compared to the line strengths as measured directly on the spectra from the MILES library. Since both our PPAK spectra and the spectra from the MILES library are flux-calibrated, these offsets should be zero. We find that for most indices this is indeed the case, except for the most blue and most red indices. We therefore suspect that the flux-calibration on these parts of the spectra have not been perfect. We also see large deviations

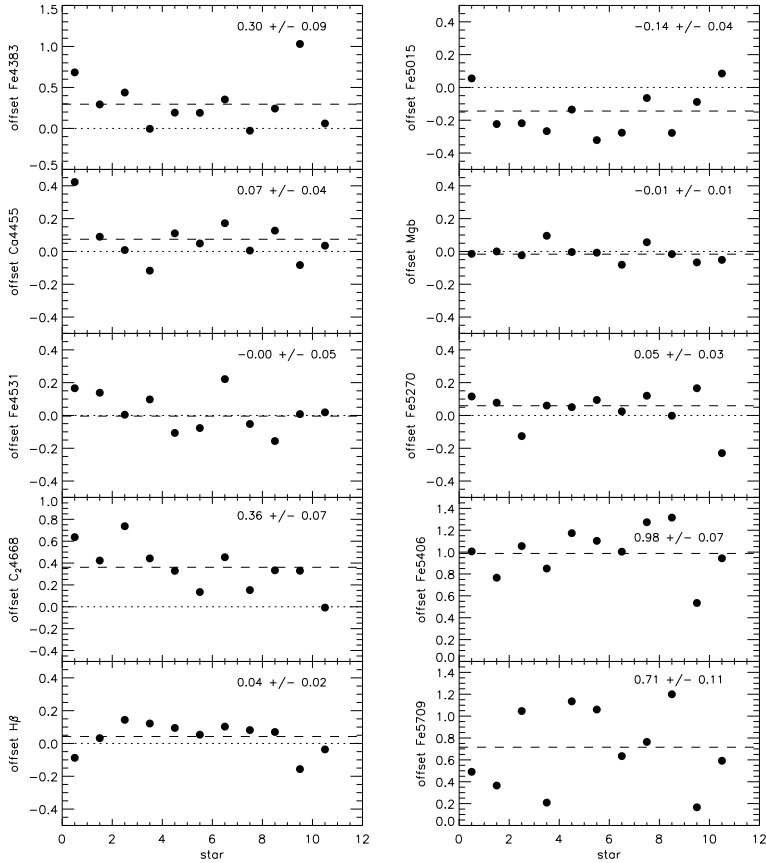


**Figure 4.6** — Offsets in line strength indices as measured from our observed stars and as measured directly from the MILES library. The offsets are defined as MILES - PPAK, and are printed in the upper right corner of each panel. Errors are standard deviations divided by  $\sqrt{N}$ , with  $N$  the number of observed stars (which in this case means  $N = 11$ ). Dashed lines correspond to the mean offset, dotted lines indicate an offset of zero. See text for more details.

for the Fe5335 index, but these are most likely caused by features resulting from a bad column on the CCD around this wavelength range.

Since for most indices our line strength measurements agree with those from the MILES library, we determined offsets to the Lick/IDS system using all the 235 stars in common between the Lick and MILES libraries. These offsets can be found in Table 4.4, and were applied to our data.

We present maps of the measured indices in Figure 4.7. Errors were determined with Monte Carlo simulations, where we took the noise of our observed

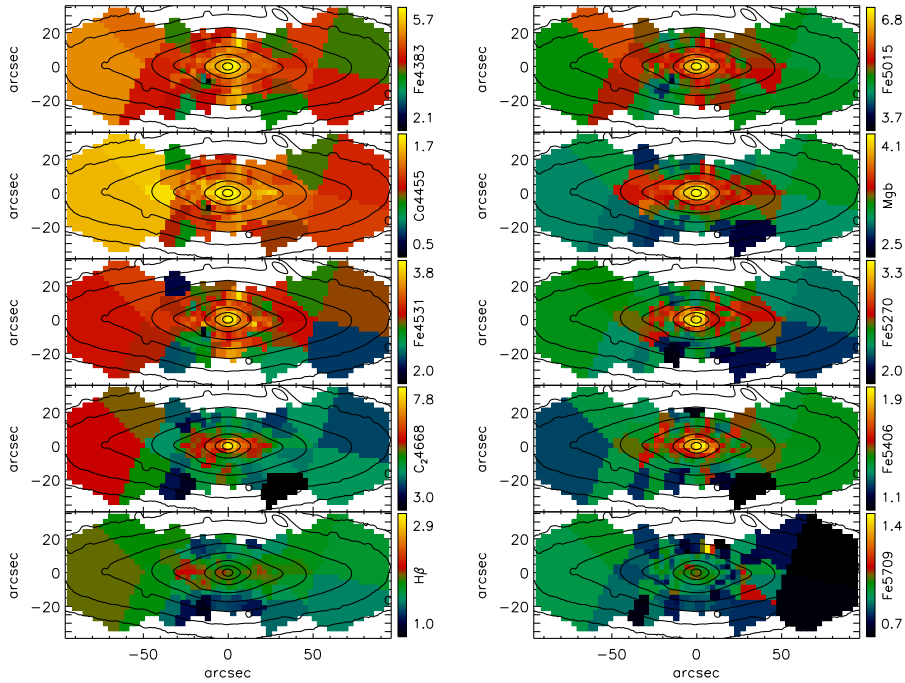


**Figure 4.7** — Line strength maps of NGC 2549. Maps are orientated such that North is to the left and East down. The Fe5335 line strength map has been omitted, as this index was affected by a bad column on the CCD and could therefore not be reliably measured. See the colour supplement for a colour version of this figure.

spectrum and the uncertainty in radial velocity into account.

We compared our line strength measurements of NGC 2549 with those observed with SAURON and presented by Kuntschner et al. (2006) for those line strengths that we have in common (i.e.  $H\beta$ , Fe5015 and  $Mg b$ ). For  $H\beta$  and  $Mg b$  these values agree within the errors introduced by applying different Lick offsets, but for Fe5015 the offset between the two datasets is larger, up to  $0.9\text{\AA}$ . This difference could be caused by a different removal of the [O III] lines from the spectra, as the measurement of this index critically depends on the treatment of this emission line. However, also in literature offsets between different datasets are mentioned (e.g. McDermid et al. 2006), and different values for offsets from flux-calibrated spectra to the Lick system are reported for different instruments (e.g. Kuntschner 2000; Norris, Sharples & Kuntschner 2006; Sánchez-Blázquez et al. 2009).

## 4.4 Stellar population models

We now turn our attention to the properties of the stellar population in NGC 2549. For our analysis we use the  $H\beta$ , Fe5015, Mg *b* and Fe5270 indices, as these indices can be well measured and show the most stable maps and offsets (see Figures 4.6 and 4.7). In order to avoid dependence on  $\alpha$ -enhancement  $[\alpha/\text{Fe}]$ , we couple the iron and Mg *b* indices into the following abundance ratio insensitive indices (Kuntschner et al. in prep):

$$[\text{MgFe50}]' = \frac{0.69 \times \text{Mg}b + \text{Fe5015}}{2}, \quad (4.1)$$

$$[\text{MgFe52}]' = \frac{0.64 \times \text{Mg}b + \text{Fe5270}}{2}. \quad (4.2)$$

Our main goal in this section is to estimate the stellar mass-to-light ratio  $M_*/L$ , as this value is currently one of the main uncertainties when constructing mass models including dark matter. For the first time we are now able to use IFU data to generate  $M_*/L$  maps, based on line strength measurements.

### 4.4.1 Single stellar population modeling

We employ the stellar population models based on the MILES library (Sánchez-Blázquez et al. 2006; Vazdekis et al. in prep.) for our analysis. These models predict line strength indices, colours and stellar mass-to-light ratios ( $M_*/L$ ) for different combinations of age, metallicity and initial mass function (IMF). We fix the IMF to the Kroupa IMF (Kroupa 2001) and find the predicted line strength indices and  $M_*/L$  for a grid uniformly sampled in metallicity and  $\log(\text{age})$ . Since the original models are sparsely sampled in metallicity ( $[Z/H] = -0.71, -0.40, 0.00$  and  $0.22$ ) and not uniformly sampled in  $\log(\text{age})$ , we interpolated the tables generated by the models to construct this uniform grid. Next, we used a maximum likelihood estimator to find the most likely value for  $M_*/L$ , given the observed line strength indices. Errors were determined by 68 per cent confidence intervals in the probability distributions.

We repeated the above analysis for each bin in our PPAK data cube, and thus were able to generate maps of  $M_*/L$ , as well as age and metallicity. These maps are shown in Figure 4.8. We find that both the stellar  $M/L$  and age are reasonably constant over the total FoV, out to  $4 R_e$ . For  $M_*/L$  in *R*-band we find a value of  $2.6 \pm 0.6 M_\odot/L_{\odot,R}$ , while the age of the stellar population is about  $9 \pm 5$  Gyr,

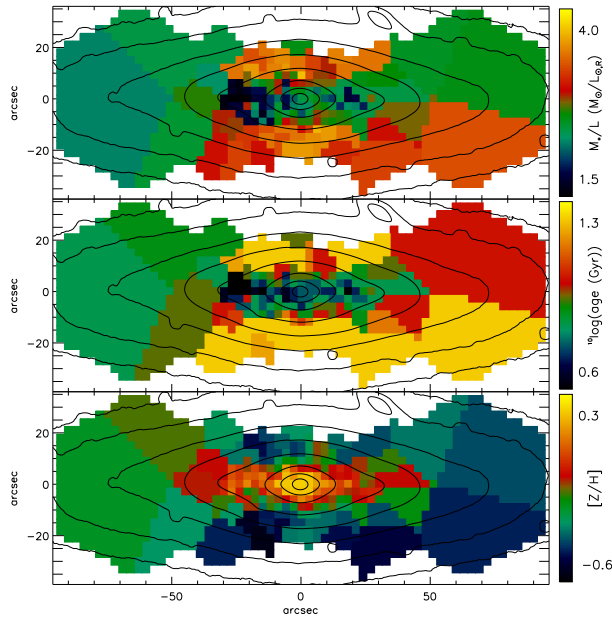


**Figure 4.8** — From top to bottom: stellar mass-to-light ratio ( $M_*/L$ ) in  $R$ -band, age and metallicity ( $[Z/H]$ ) in NGC 2549. Maps are again orientated with North to the left and East down. See the colour supplement for a colour version of this figure.

though younger in the central part of the galaxy. The metallicity is enhanced in the centre, and it drops from  $[Z/H] = 0.2$  in the centre to  $-0.4$  at large radii.

It would be interesting to see how our maps of  $M_*/L$ , age and metallicity compare to maps obtained using colours instead of line indices (see Zibetti, Charlot & Rix 2009 for a demonstration of this method). Since this would require very accurate colours out to large radii and a well-understood calibration between different photometry bands, as well as a correction for galactic extinction, we do not make this comparison here. For future projects it will be fruitful to obtain deep imaging in different optical and near-infrared bands, in addition to deep integral-field spectrography.

#### 4.4.2 Two components in NGC 2549?

In the stellar kinematic maps we see hints for a cold disc, embedded in a thicker disc or bulge. To look for evidence for an embedded disc in the line strengths, we start by plotting the indices as a function of radius, to determine the line strength gradients. The slopes of these gradients provide clues on the formation scenario

of the galaxy, with steep gradients resulting from monolithic collapse (Carlberg 1984), while mergers dilute existent gradients (White 1980). More recent simulations however have shown that depending on the gradients in the parent galaxies, the merger remnant can have either a steeper or a shallower gradient than its progenitors (Di Matteo et al. 2009) and that a combination of monolithic collapse and hierarchical galaxy formation is required to reproduce the gradients that are observed in early-type galaxies (Kobayashi 2004).

Before plotting the gradients, we first transform our observed indices into magnitudes:

$$\text{index}' = -2.5 \log\left(1 - \frac{\text{index}}{\Delta\lambda}\right), \quad (4.3)$$

where  $\Delta\lambda$  is the width of the central bandpass (see Table 4.4), and the index in magnitudes is denoted by a prime [ $'$ ]. Next, we average the indices along the isophotes of the galaxy, taking the flattening of the galaxy into account. We plot our results in Figure 4.9. We find no change in the line strength gradients, in fact: the slopes remain constant from  $0.1 R_e$  out to at least  $4 R_e$ . Hopkins et al. (2009b) sketch a scenario in which a secondary starburst following a major merger steepens the line strength gradients in the inner part of the galaxy, while violent relaxation flattens these gradients at larger radii. We find no support for this scenario, which would be an indication of a second component, although it remains possible that the merger happened sufficiently long ago (more than several Gyr) and that therefore the expected change in line strength slope between the young disc and older bulge has disappeared. We note that the slope of the metallicity gradient seems to flatten in the inner 5 arcseconds of the galaxy, however data with higher spatial resolution is needed to investigate this further.

Norris et al. (2006) used line strength profiles along the major and minor axis to identify a young disc embedded in an old bulge in the lenticular galaxy NGC 3115. Since the disc in this galaxy is more flattened than the bulge, they found a difference in gradient between the major and minor axis. To investigate whether NGC 2549 shows similar behaviour, we select the bins that are located within 3 arcsec from the major and minor axis, and plot their radial profiles (see Figure 4.9). We correct the distance along the minor axis by taking the flattening into account. We find no distinction in line strength behaviour between the major and minor axis on the galaxy. In the metallicity profile however we see a small difference in slope between the minor and major axis, which could indicate that indeed a thin metal-rich disc is present, embedded in a thicker, metal-poorer disc. This view is strengthened by the metallicity map (Figure 4.8), where the



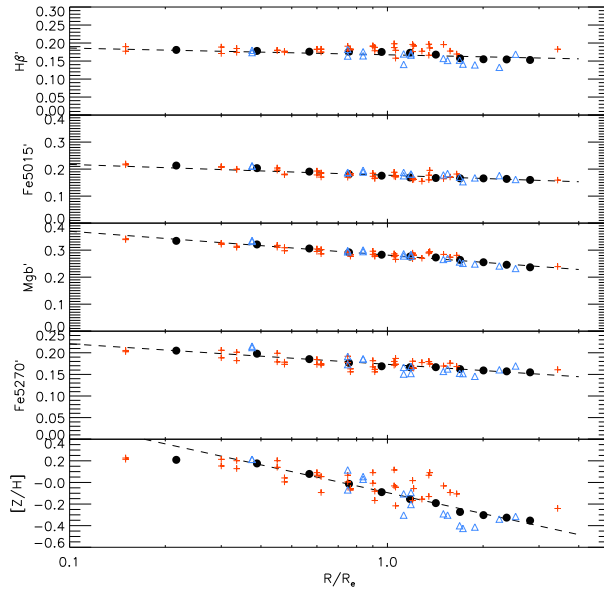


**Figure 4.9** — Line strength indices (from top to bottom  $H\beta$ , Fe5015, Mg  $b$  and Fe5270) in magnitudes, and metallicity  $[Z/H]$ , as a function of radius. Black dots denote averaged line strengths along the isophotes of the galaxy, while the crosses and open triangles denote measurements along the major and minor axis, respectively. The minor axis radii have been corrected for the flattening of the galaxy. Errorbars are comparable to the size of the plotting symbols.

iso-metallicity contours appear more flattened than the isophotes. This effect has been observed in several other fast-rotators (e.g. Kuntschner et al. in prep.).

## 4.5 Dynamical models

In this section we investigate whether a dark matter halo is needed to fit the observed stellar kinematics of NGC 2549, and constrain the amount of dark matter. We use the triaxial Schwarzschild modeling code of van den Bosch et al. (2008), which was extended to allow for the inclusion of a dark matter halo by Weijmans et al. (2009a). Briefly, a mass distribution is constructed by combining a dark halo, black hole and a deprojection of the observed stellar surface brightness. Orbits are then calculated in the potential constructed from the mass distribution. These orbits are then combined into a superposition, that best fits the observed kinematics, while constraining the fit such that it reproduces the stellar mass distribution.

### 4.5.1 Schwarzschild models

NGC 2549 is an edge-on fast rotator (c.q. discy elliptical) that shows no signs of a strong bar and can therefore be reasonably modeled with an oblate axisymmetric mass distribution. Krajnović et al. (2009) presented axisymmetric Schwarzschild models of NGC 2549 and we use their best-fitting model as a starting point. We adopt their inclination of  $88^\circ$ , and (a close to) oblate geometry. We fix the black hole mass to their best-fit value  $M_\bullet = 1.4 \times 10^7 M_\odot$ . We adopt their dynamical  $M/L = 4.7 M_\odot/L_{\odot,R}$  for the stellar  $M/L$  (constructing a maximal spheroid model), as well as their Multi-Gaussian Expansion (MGE, see Emsellem, Monnet & Bacon 1994; Cappellari 2002) mass model. This MGE model is based on HST/WFPC 2 imaging in R-band, complemented with wide-field MDM imaging in V-band, that was scaled to match the WFPC 2 image. We added a spherical halo with a NFW profile to the total potential :

$$\Psi_{\text{halo}}(r) = -4\pi G \rho_s r_s^2 \frac{r}{r_s} \ln\left(1 + \frac{r}{r_s}\right), \quad (4.4)$$

with  $G$  the gravitational constant,  $\rho_s$  a characteristic density and  $r_s$  a characteristic radius. These last two quantities are coupled to the concentration parameter  $c$  of the halo and the halo mass  $M_{200}$ , which is the total mass of the halo within  $r_{200}$ :

$$\frac{\rho_s}{\rho_{\text{crit}}} = \frac{200}{3} \frac{c^3}{\ln(1+c) - c/(1+c)}, \quad (4.5)$$

$$M_{200} = 4\pi \rho_s r_s^3 \left[ \ln(1+c) - \frac{c}{1+c} \right]. \quad (4.6)$$

Here  $r_{200}$  is the radius within which the mean density of the halo has dropped to 200 times the critical density  $\rho_{\text{crit}}$ .

For now, we fix the concentration of the halo to  $c = 10$ , to be consistent with predictions from cosmological simulations (Bullock et al. 2001) and to reduce the parameter space that needs to be searched. We then optimized the models by varying the halo mass  $M_{200}$ , while fitting the PPAK kinematics up to the fourth Gauss-Hermite moment  $h_4$ , as well as the SAURON kinematics (Emsellem et al 2004; Krajnović et al. 2009) up to  $h_6$ , which cover the central  $R_e$  of the galaxy with higher spatial resolution.

The PPAK data shows a somewhat higher velocity dispersion than the SAURON data (see Figure 4.4). Since we combine the two datasets here in one dynamical

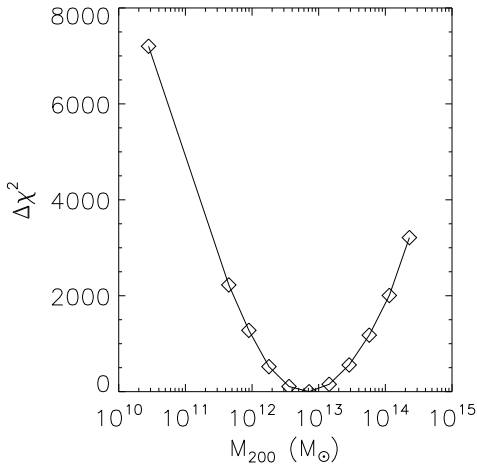


**Figure 4.10** —  $\Delta\chi^2$  levels for the Schwarzschild models of NGC 2549. The only free parameter in these models is  $M_{200}$  (total halo mass). The model without dark halo is relocated at  $3 \times 10^{10}$ , to place it within the plot.

model, a pragmatic solution is to scale the PPAK velocity dispersions to agree with the SAURON ones. After some experimentation we found that a quadratic correction worked best:

$$\sigma_{\text{model}} = \sqrt{\sigma_{\text{PPAK}}^2 + \sigma_{\text{instr}}^2 - \sigma_{\text{corr}}^2}, \quad (4.7)$$

with  $\sigma_{\text{instr}}$  the instrumental resolution ( $103 \text{ km s}^{-1}$ ) and  $\sigma_{\text{corr}}$  a correction term. We found a correction of  $110.5 \text{ km s}^{-1}$  to minimize the differences between the SAURON and the PPAK observations, while taking the different seeing into account. We then applied this correction term to the PPAK dispersion.

In Figure 4.10 we show the  $\chi^2$  for the different halo masses. The amount of dark matter is constrained well, due to the flat rotation curve and the rising dispersion at large radii. The halo has a mass of  $M_{200} = 7 \times 10^{12} M_{\odot}$ . The kinematics of the best-fitting model are shown in Figure 4.11. The model reproduces the mean stellar velocity very well. The dispersion out to 30 arcsecond is also reproduced nicely, but the dispersion rise at larger radii along the major axis can not be reproduced by the spherical NFW halo. Therefore the models also fail to reproduce the higher moments, as they have relatively larger errors. Hopefully, dark haloes with a large central core and a lower stellar  $M/L$  will be able to reproduce the data. Given the large spatial extent of the PPAK data we should be able to constrain the mass distribution of the halo, and this is currently under investigation.

In Figure 4.12 we show the anisotropy of our best-fitting model, compared

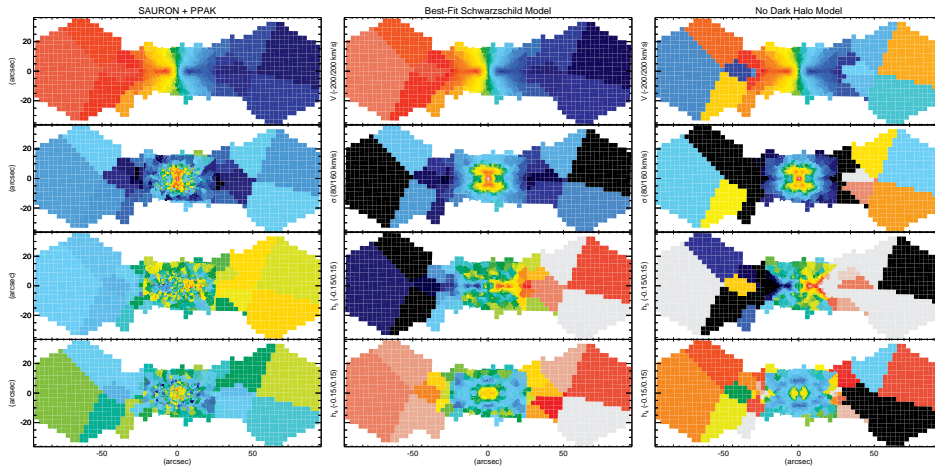


**Figure 4.11** — Point-symmetrized kinematics of the SAURON and PPAK data and the best-fitting model with a spherical NFW halo. The model reproduces the flat rotation curve well, but has trouble reproducing the rising dispersion at radii larger than 40 arcseconds. Consequently, the higher moment at those radii cannot be reproduced either. The model without a dark halo cannot reproduce the observed rotation field, and is overall a poor fit to the data. A larger colour version of this figure can be found in the colour supplement.

to a model without halo and a model with a too heavy halo. We parametrize the anisotropy with

$$\beta_r = 1 - \frac{\sigma_\phi^2 + \sigma_\theta^2}{2\sigma_r^2}, \quad (4.8)$$

where  $(r, \theta, \phi)$  are the standard spherical coordinates. For all models  $\beta_r$  is low, which means that the stellar orbits are strongly tangentially anisotropic. This is a clear signature of a disc-like structure. In contrast to what is seen in spherical or axisymmetric models (e.g. Richstone & Tremaine 1984; Dekel et al. 2005), we do not see an increase of radial anisotropy with increasing halo mass. This behaviour should be investigated in more detail. However, the higher moments are currently not well produced in the model and they typically constrain the amount of anisotropy.

After inspecting the distribution of the orbits in the Schwarzschild model we found that the system is made up out of three distinct components: a compact bulge, a small (inner) thin disc and a large thick disc, similar to what was found by Krajnović et al. (2008). As this disc is (perhaps) also seen in the metallicity map, it would be interesting to look into these separate phase space components

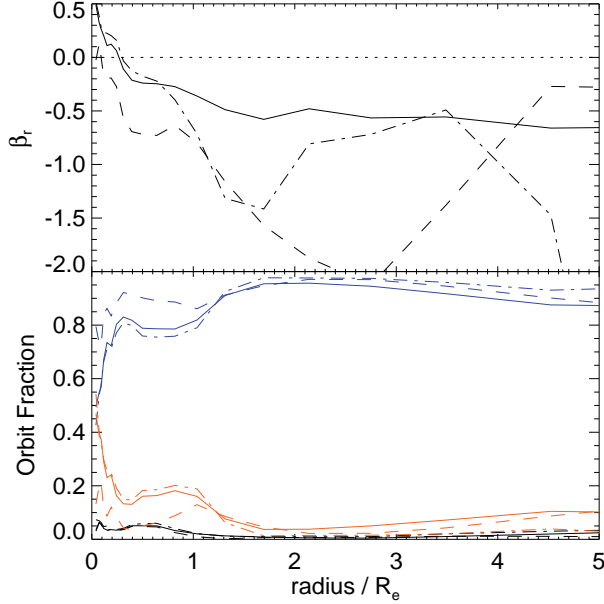


**Figure 4.12** — Orbital structure of NGC 2549. Top panel: velocity anisotropy  $\beta_r$  as a function of radius (see Equation 4.8). The solid line indicates our best-fitting model ( $M_{200} = 7 \times 10^{12} M_{\odot}$ ), the dashed and dashed-dotted line denote the model without halo and the model with a too heavy halo ( $M_{200} = 3 \times 10^{13} M_{\odot}$ ), respectively. Bottom panel: fraction of orbit types as function of radius for the models of the top panel. Blue lines denote fractions of short axis tubes, red lines long axis tubes and black lines the fractions of box orbits. See the colour supplement for a colour version of this figure.

in more detail, at it might allow us to measure the metallicities of the three components individually.

## 4.5.2 Jeans anisotropic models

In addition to Schwarzschild models, we also constructed Jeans anisotropic models of our dataset. These axisymmetric models are based on the second velocity moments, given by:

$$V_{\text{rms}} = \sqrt{V^2 + \sigma^2}, \quad (4.9)$$

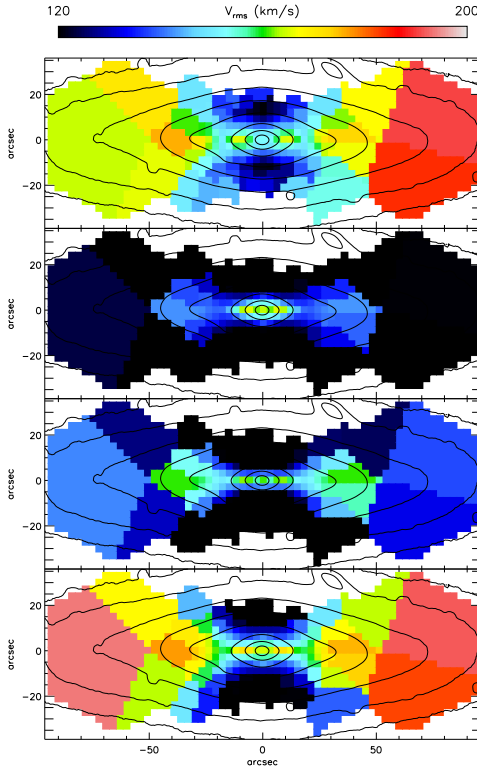


**Figure 4.13** — Jeans anisotropic models of NGC 2549, based on the second velocity moments of the PPAK kinematics. From top to bottom: bi-symmetrized observations, model without dark halo and  $\beta_z = 0.17$ , model without dark halo with  $\beta_z = 0.17$  for  $R < 20$  arcsec and  $\beta_z = -10$  for  $R > 20$  arcsec, and the finally the best-fitting model with an NFW halo and  $\beta_z = 0.17$ . See the colour supplement for a colour version of this figure.

and are characterized by the anisotropy parameter  $\beta_z$ , which is defined as:

$$\beta_z = 1 - \overline{v_z^2} / \overline{v_R^2}. \quad (4.10)$$

This modeling method is explained in detail by Cappellari (2008), who also presented a mass model of NGC 2549 based on the SAURON observations. His best-fitting model is edge-on ( $i = 90^\circ$ ) and has  $\beta_z = 0.17$ . Adopting these values we try to construct a Jeans model to reconstruct the observed PPAK kinematics, but we find that we cannot construct a mass model without extra dark matter, even if we allow for an extreme anisotropy in the outer parts of the galaxy (see Figure 4.13). We therefore add a spherical NFW halo to the model, with  $c = 10$  to be consistent with the Schwarzschild models. The dark halo is included in the fit as a one-dimensional MGE model and we fit for  $M_{200}$  and  $M_*/L$ . We find a

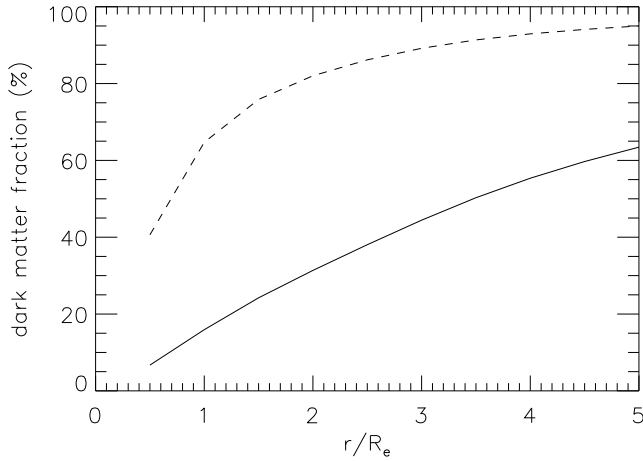


**Figure 4.14** — Enclosed dark matter fraction as a function of radius. The solid line denotes the best-fitting maximum spheroid model with  $M_*/L = 4.7M_\odot/L_{\odot,R}$ , while the dashed line follows the model with  $M_*/L = 2.6M_\odot/L_{\odot,R}$ , consistent with stellar population models.

good fit to the data (see Figure 4.13), with a best-fitting halo mass of  $M_{200} = 1.3 \times 10^{13} M_\odot$ , which is within a factor of two with the best-fitting halo mass found by the Schwarzschild model. This agreement is very encouraging and provides confidence for our results, as these two modeling methods work from different principles. The Jeans models can also reproduce the increase of  $V_{\text{rms}}$  at larger radii. This quantity is mostly dominated by the rotation of the system, which is large compared to the velocity dispersion.

The best-fitting stellar  $M/L$  is  $5.5 M_\odot/L_{\odot,R}$  which deviates from the value found by Schwarzschild modeling. However, the Jeans models were fitted to the PPAK data only, which were not corrected for the offset between the PPAK and SAURON velocity dispersions. Scott et al. (2009) present anisotropic models of NGC 2549 based on SAURON kinematics and find a best-fitting  $M/L$  of  $4.8 M_\odot/L_{\odot,R}$ , in agreement the Schwarzschild models of Krajnović et al. (2009).

### 4.5.3 Dark matter fractions

In Figure 4.14 we show the enclosed dark matter fraction as a function of radius for our best-fitting Schwarzschild model. The total stellar mass in this model is  $2.8 \times 10^{10} M_\odot$ , which is a factor  $\sim 250$  smaller than the total halo mass  $M_{200} = 7 \times 10^{12} M_\odot$ . Within  $1 R_e$ , 16 per cent of the total mass is dark, while within  $5 R_e$ , this percentage has grown to 63 per cent. Note however that this model assumes

a maximal spheroid, and that therefore these percentages are lower limits.

Since we also have an estimate of the stellar  $M/L$  based on stellar population modeling, we scaled our Schwarzschild models to this value. This resulted in a decrease of almost 50 per cent in stellar mass, as now  $M_*/L$  was fixed to  $2.6 M_\odot/L_{\odot,R}$ , instead of the maximal allowed value of  $4.7 M_\odot/L_{\odot,R}$ . Consequently, the mass of the best-fitting dark halo increased, to compensate for the loss in stellar mass. The best-fitting halo for this model has  $M_{200} = 1 \times 10^{15} M_\odot$ , again assuming an NFW profile with a concentration  $c = 10$ . The dark mass inside  $1 R_e$  for this model corresponds to 65 per cent of the total mass, increasing to 95 per cent at  $5 R_e$  (see also Figure 4.14). However, this model overpredicts the velocity dispersion at larger radii, and therefore  $M_*/L$  is most likely underestimated. This implies however that the dark matter fractions in NGC 2549 are bracketed by the values quoted here for these two extreme models.

The difference in  $M_*/L$  as determined by the maximal spheroid model and the stellar population models seems rather large, but a comparable difference between these two values was observed by Weijmans et al. (2008) for the early-type galaxy NGC 2974. They determined dark matter fractions in this galaxy, using the kinematics of a large H I ring surrounding this system. For the two early-type galaxies NGC 3379 and NGC 821, studied by Weijmans et al. (2009a), the difference between dynamical and stellar  $M/L$  was much smaller (see also Cappellari et al. 2006), and these systems seem to be less dark matter dominated than NGC 2549. It is interesting to note that both NGC 2549 and NGC 2974 are disc-like galaxies that show rotation out to at least  $5 R_e$ , while NGC 3379 and NGC 821 are both rounder and show little rotation at large radii. However, a comparison between the different models for these galaxies is not straightforward because of the maximal spheroid assumption. A more thorough analysis is needed to make a fair comparison between these models, but this is currently beyond the scope of this text.

## 4.6 Discussion and summary

We observed the early-type galaxy NGC 2549 with the integral-field spectograph PPAK out to at least  $4 R_e$ . We obtained integrations of several hours and in the outer part of the galaxy binned individual spectra together, to obtain sufficient signal-to-noise to measure both stellar kinematics and absorption line strengths. The velocity map displays regular rotation out to the edge of the observed field, while the velocity dispersion has a declining profile, followed by a slight increase outside 30 arcsec. Using stellar population models and the observed line strengths



as constraints, we constructed maps of age, metallicity and stellar  $M/L$ . The metallicity map shows evidence for a younger, metal-rich disc-like component, embedded in a larger disc or bulge. Further hints for an embedded disc were presented by Krajnović et al. (2009), who reported the presence of two disc-like components based on the SAURON stellar kinematics. Our Schwarzschild model, based on the new PPAK spectra, complemented with SAURON kinematics for the central part of the galaxy, also show evidence for embedded components: we identify from the orbital structure a compact bulge, a thin inner disc and a large thick disc. These observations provide hints for the merger and starformation history of NGC 2549. One would expect to find an inner disc as we described here, as a result from secondary starformation after a major merger (e.g. Hopkins et al. 2009b).

From our Schwarzschild model we find that a dark halo is required to reconstruct the observed kinematics. We explored possible halo masses of a spherical NFW halo, with a concentration  $c = 10$ , within the maximum spheroid (or minimal halo) assumption. The best-fitting halo mass agrees with the one obtained from anisotropic Jeans modeling of the PPAK kinematics. Since the two modeling methods arise from different principles, the agreement in halo mass is very encouraging. We find that within  $1 R_e$  at least 16 per cent of the total mass is dark, while within  $5 R_e$  this percentage has grown to 63 per cent. However, if we adopt the stellar  $M/L$  found by stellar population modeling, NGC 2549 becomes much more dark matter dominated: already within  $1 R_e$  more than half (65 per cent) of the total mass lies within the dark halo. However, even within the same stellar population model, differences in initial-mass function, treatment of stellar winds and lower-mass cuts can introduce large uncertainties (up to 40 per cent) in  $M_*/L$ .

Our Schwarzschild model cannot exactly reproduce the observed behaviour of the velocity dispersion at larger radii. This could be caused by the restrictions that we have imposed on our halo model. To limit the parameter phase, we only explored spherical haloes with a (cuspy) NFW profile. However, simulations have shown that haloes are most likely flattened or triaxial (e.g. Hayashi, Navarro & Springel 2007), while observations of low-surface brightness and dwarf galaxies have found evidence for cored halo profiles (e.g. Weldrake, de Blok & Walter 2003; de Blok et al. 2008). Now that we have obtained stellar kinematics over the complete galaxy field out to  $4 R_e$  instead of only major axis measurements (Weijmans et al. 2009a), we should start to explore whether we can constrain the shape and profile of the dark halo. If indeed it becomes possible to model the dark halo in such detail, this will provide important tests for galaxy formation theories.

## Acknowledgements

It is a pleasure to thank Felix Hormuth and Sebastian Sánchez for preparing and performing our observations at Calar Alto. We also gratefully acknowledge Eric Emsellem, Davor Krajnović and Richard McDermid for fruitful discussions.

This research was supported by the Netherlands Organization of Scientific Research (NWO) through grants 614.000.426 and 614.000.301. MC acknowledges support from an STFC Advanced Fellowship (PP/D005574/1).

This work is based on observations collected at the Centro Astronómico Hispano Alemán (CAHA) at Calar Alto, operated jointly by the Max-Planck Institut für Astronomie and the Instituto de Astrofísica de Andalucía (CSIC).

---

## Chapter 5

---

# Dissecting the Lyman Alpha emission halo of LAB1

We report observations of Lyman Alpha Blob 1 (LAB1) in the SSA 22 protocluster region ( $z = 3.09$ ) with the integral-field spectrograph SAURON. We increased the signal-to-noise in the spectra by more than a factor three compared to our previous observations. This allows us to probe the structure of the LAB system in detail, examining its structure in the spatial and wavelength dimensions. We find that the emission from the system comes largely from five distinct blobs. Two of the emission regions are associated with Lyman Break Galaxies, while a third appears to be associated with a heavily obscured submillimeter galaxy. The fourth and fifth components do not appear to be associated with any galaxy despite the deep imaging that is available in this field. If we interpret wavelength shifts in the line centroid as velocity structure in the underlying gas, many of these emission systems show evidence of velocity shear. It remains difficult to distinguish between an underlying rotation of the gas and an outflow driven by the central object. We have examined all of the line profiles for evidence of strong absorption features. While several systems are better fitted by the inclusion of a weak absorption component, we do not see evidence for a large-scale coherent absorption feature such as that seen in LAB2.

Anne-Marie Weijmans, Richard G. Bower, James E. Geach, A. Mark Swinbank,  
Richard J. Wilman, P. Tim de Zeeuw & Simon L. Morris  
Submitted to *Monthly Notices of the Royal Astronomical Society*

## 5.1 Introduction

By allowing us to probe the gaseous haloes around  $z \sim 3$  galaxies, large scale Lyman  $\alpha$  nebulae provide a fascinating insight into the formation of high-redshift galaxies. The first and brightest of these haloes were discovered by Steidel et al. (2000) in the SSA 22 protocluster region at  $z = 3.09$ . Subsequently a population of fainter Lyman Alpha Blobs (LABs) was detected in deep narrow-band imaging surveys (e.g. Matsuda et al. 2004; Nilsson et al. 2006, Smith & Jarvis 2007), revealing that LABs have a large spread in properties such as surface brightness and morphology, and it has been suggested that their presence is linked to dense environments (Matsuda et al. 2004). Follow-up observations in the optical, near-infrared and particularly the far-infrared suggest that LABs are sites of massive galaxy formation, enhanced by the cluster environment (e.g. Chapman et al. 2004). This view is supported by the discovery of luminous submillimeter sources in several LABs (e.g. Geach et al. 2005). LAB systems like those discovered by Steidel et al. (2000) are also found around high-redshift radio galaxies (e.g. Chambers, Miley & van Breugel 1990; Villar-Martín et al. 2002). However, the study of such radio loud systems is complicated by the presence of radio jets and lobes. It is unclear whether these systems are directly comparable to the radio quiet LABs that we discuss in this paper, or that they have a different power source, such as the injection of cosmic rays by the radio source (e.g. Ferland et al. 2009).

The origin of radio quiet LABs is still unclear, and three different scenarios have been proposed to explain their existence. One is that the gas in LABs is heated by photo-ionisation, caused by massive stars and/or active galactic nuclei (AGN) (Geach et al. 2009). However, for one third of the LABs in the sample of Matsuda et al. (2004), the observed UV luminosities are too low to produce the observed Ly $\alpha$  radiation, although putative ionising sources could be obscured along our line of sight. For example, Geach et al. (2009) argue that in a large fraction of LABs there is sufficient UV flux from an obscured AGN component to power the extended line emission, despite large dust covering fractions. While photo-ionisation is likely to play a role in powering LABs, it is nonetheless instructive to consider alternative or additional power sources for the Ly $\alpha$  emission in LABs, since it is not clear that a single mechanism (such as photo-ionisation) is responsible for all of the observed properties of these objects.

An alternative scenario is that the gas in LABs is excited by cooling flows (e.g. Haiman, Spaans & Quataert 2000; Fardal et al. 2001; Dijkstra & Loeb 2009). Nilsson et al. (2006) argue that the emission in the LAB they detected in the GOODS South field originates from cold accretion onto a dark matter halo. This view is supported by the lack of continuum counterparts, which could photo-

ionise the gas, and the absence of a massive starburst in the infrared, that could point to a superwind outflow (see below). Instead, they find a good match between their observed surface brightness profile and the profiles derived from theoretical models for collapsing clouds from Dijkstra, Haiman & Spaans (2006). A similar analysis is given by Smith et al. (2008) for the LAB presented in Smith & Jarvis (2007).

The third proposed origin for extended Ly $\alpha$  emission haloes is provided by the so-called superwind model (e.g. Taniguchi & Shioya 2000; Ohyama et al. 2003). After an initial starburst, massive stars die in supernovae. If the resulting supernova remnants overlap, they could form a superbubble (e.g. Heckman, Armus & Miley 1990), from which a superwind can blow gas into the intergalactic medium if the kinetic energy in the gas is large enough to overcome the gravitational potential. Taniguchi & Ohyama (2000) suggest an evolutionary sequence for elliptical galaxies that includes LABs. During the initial starburst, a galaxy can be enshrouded by gas and dust grains, and is therefore observable as a (dusty) submillimeter source. The LABs represent the subsequent superwind phase, expelling the gas and dust, and therefore rendering the galaxy fainter in the submillimeter regime. After this phase, the galaxy continues to develop into a normal elliptical galaxy.

The brightest and most extended LAB observed to date is LAB1 (SSA22a-C11), one of the two LABs described by Steidel et al. (2000). This LAB has a Ly $\alpha$  luminosity of  $1.1 \times 10^{44}$  ergs s $^{-1}$  at  $z = 3.1$  (Matsuda et al. 2004), and a spatial extent of  $\sim 100$  kpc. Matsuda et al. (2004) find bubble-like structures in narrowband images of LAB1, in support of the superwind model for this LAB. Bower et al. (2004) observed LAB1 with the integral-field spectrograph SAURON (Bacon et al. 2001). They found extensive emission, and a large velocity dispersion for the Ly $\alpha$  emission line ( $\sim 500$  km s $^{-1}$ ). Although interpretation of the spectra of LAB1 is not straightforward, since Ly $\alpha$  is a resonant line and therefore emission can easily get scattered, they find similarities between LAB1 and the local emission-line halo of NGC 1275 in the Perseus cluster. Longer observations of LAB2 with the same spectrograph suggested the existence of a dense outflowing shell of material around this system (Wilman et al. 2005). However, spectra of higher signal-to-noise are needed to find evidence for outflows in LAB1.

We therefore reobserved LAB1 with SAURON, adding signal to the data already published by Bower et al. (2004). By increasing the observing time from 9 hours in the original dataset to 23.5 hours in our new datacube, we increased the signal-to-noise in the spectra, and therefore were able to obtain line profiles and kinematic maps of the Ly $\alpha$  emission in this region. We describe the new observa-

tions and data reduction of LAB1 in Section 5.2 and analyse the spectra in Section 5.3. In Section 5.4 we discuss our results and speculate on the structure and origin of LAB1. Throughout this paper, we assume a flat cosmology with  $H_0 = 70 \text{ km s}^{-1} \text{ Mpc}^{-1}$ ,  $\Omega=0.3$  and  $\Lambda = 0.7$ . In this scenario, 1 arcsec at  $z = 3.1$  corresponds to 7.5 kpc.

## 5.2 Observations and data reduction

LAB1 was previously observed for 9 hours with SAURON at the William Herschel Telescope at La Palma, Spain, in July 2002. The relatively large field-of-view ( $41 \times 33 \text{ arcsec}^2$ ) and high throughput (20 per cent) make this spectrograph a very suitable instrument for deep Ly $\alpha$  observations, even though it was originally built to study the dynamics and stellar populations of nearby early-type galaxies (de Zeeuw et al. 2002). The relatively high spectral resolution of  $4.2 \text{ \AA}$  (FWHM) of the instrument, in combination with the wide field, was obtained by compromising on the total wavelength coverage (4810 to 5350  $\text{\AA}$ ). As a result, SAURON can observe Ly $\alpha$  systems at redshifts  $2.96 < z < 3.40$ , and fortunately, LAB1 resides within this redshift range ( $z = 3.1$ ). A description of the earlier observations of LAB1 and their reduction can be found in Bower et al. (2004).

In these previous observations, we lacked the signal-to-noise ( $S/N$ ) to search for asymmetries in the line profiles and signs for possible neutral absorption, as found in SAURON spectra of LAB2 by Wilman et al. (2005). We therefore re-observed LAB1 for an additional 15 hours with SAURON, between 15 and 21 September 2006. The observations were split into individual exposures of 1800 seconds and dithered by a few arcseconds. The data were reduced using the dedicated XSAURON software (Bacon et al. 2001). We replaced our calibration frames, to correct for a malfunctioning shutter (see Weijmans et al. 2009a for more details). We had also observed six blank sky fields, and created a so-called superflat by taking the smoothed median of these blank frames and the dithered object frames in the spectral direction. Dividing our already flat-fielded data by this superflat removed most of the remaining flat-field residuals. The spectra were degraded to a resolution of  $4.9 \text{ \AA}$  (FWHM) to be consistent with the LAB1 observations of Bower et al. (2004), and sky subtracted with the signal from the SAURON skylenslets, that obtain simultaneous sky spectra pointing 2 arcminutes away from the main field-of-view.

Before merging this new dataset with the cubes of Bower et al. (2004), we first re-reduced these spectra in the same way as described above to make sure that both datasets were treated identically. One of the frames had to be discarded because of

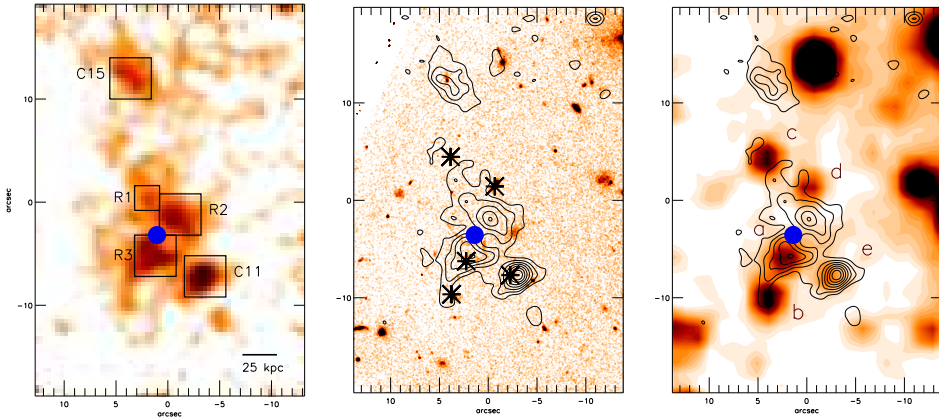


**Figure 5.1** — Ly $\alpha$  emission in the LAB1 region. Left panel: continuum subtracted Ly $\alpha$  emission, obtained from collapsing the SAURON spectra over a narrow wavelength range centred on the emission line. Interesting regions are indicated by boxes (see text). Middle panel: *HST*/STIS optical image overlaid with Ly $\alpha$  contours from the left panel. Black asterisks indicate the IRAC sources from Geach et al. (2007). Right panel: same as middle panel, but now a *Spitzer*/IRAC 3.6  $\mu\text{m}$  image is displayed. Sources identified in Geach et al. (2007) are indicated with identical nomenclature (*a-e*). In all plots, the blue dot denotes the position of the radio source (Chapman et al. 2004). All images are plotted on the same scale and are orientated such that North is up and East to the left. See colour supplement for a colour version of this plot.

bad sky subtraction. The remaining 17 frames of the old dataset were then merged with the 30 frames of the new dataset, using a faint star in the south-east corner of the field-of-view to align the cubes. In the merged cube, this star has a FWHM of 1.3 arcsec. We set the spatial resolution of the cube to 0.4 arcsec per pixel, while the spectral resolution is 1.15  $\text{\AA}$  per pixel. This final cube represents 23.5 hours of observing time, and is the deepest SAURON observation to date. The increase in  $S/N$  is a factor of 3.7 compared to the dataset of Bower et al. (2004), which is more than would be expected based on the factor 2.6 increase in exposure time. The higher than expected  $S/N$  results from improved observing and data reduction techniques, developed over the past few years within the SAURON team.

Unfortunately due to the malfunctioning shutter of the spectrograph we could not observe flux stars during the 2006 observing run. We therefore flux calibrated our data using flux values for C15 from the literature. We added the flux in a wavelength interval centred around the Ly $\alpha$  line ( $4960 \text{ \AA} < \lambda < 5000 \text{ \AA}$ ) in a  $4 \times 4 \text{ arcsec}^2$  box around C15, and scaled the number of counts to the flux given by



Field	$\alpha$	$\delta$	L (Ly $\alpha$ ) erg s $^{-1}$	STIS mag	$m_{3.6\mu\text{m}}$ mag
C15	22 <sup>h</sup> 17 <sup>m</sup> 26.1 <sup>s</sup>	00° 12' 54.1''	$1.7 \times 10^{43}$	$26.13 \pm 0.02$	>23.7
R1	22 <sup>h</sup> 17 <sup>m</sup> 26.0 <sup>s</sup>	00° 12' 42.5''	$8.4 \times 10^{42}$	>27.42	>23.7
R2	22 <sup>h</sup> 17 <sup>m</sup> 25.8 <sup>s</sup>	00° 12' 40.9''	$2.3 \times 10^{43}$	>27.42	>23.7
R3	22 <sup>h</sup> 17 <sup>m</sup> 26.0 <sup>s</sup>	00° 12' 36.9''	$2.7 \times 10^{43}$	>27.42	$22.6 \pm 0.1$
C11	22 <sup>h</sup> 17 <sup>m</sup> 25.6 <sup>s</sup>	00° 12' 34.9''	$2.3 \times 10^{43}$	$24.21 \pm 0.01$	$23.6 \pm 0.1$

**Table 5.1** — Ly $\alpha$  blobs indicated in Figure 5.1. Coordinates are provided in J2000 notation. The uncertainties in the observed Ly $\alpha$  luminosity are around 50 per cent (see §2). The last two columns give the optical (*HST*/STIS) and infrared (*Spitzer*/IRAC 3.6 $\mu\text{m}$ ) fluxes in AB magnitudes. The IRAC fluxes have been measured in circular apertures of 4 arcsec diameter, and corrected for a small aperture loss. Lower magnitude limits for non-detections are  $3\sigma$  limits.

Matsuda et al. (2004). We checked our conversion factor with Bower et al. (2004), and found a deviation of 50 per cent. As the flux calibration is the main source of uncertainty, we adopt this deviation to estimate the errors on our obtained fluxes (see Table 5.1).

## 5.3 Analysis

### 5.3.1 The halo structure of LAB1

In Figure 5.1 we show a continuum subtracted Ly $\alpha$  image of LAB1, obtained by integrating the spectra in our SAURON datacube over a small wavelength range (4960 - 5040 Å) containing the redshifted emission line. The most striking result is that LAB1 is not one coherent structure, but that the emission is concentrated in five distinct emission regions (labeled R1-R3, C11, C15), embedded in a Ly $\alpha$  emission halo (see also Matsuda et al. 2004). We estimate that about 55 per cent of the total Ly $\alpha$  emission can be associated with one of these regions. Thus it appears that the giant emission halo results from a combination of smaller emission blobs more typical LABs identified by Matsuda et al. (2004).

In order to attempt to identify each of the Ly $\alpha$  blobs (R1-R3, C11 and C15) with underlying galaxies, we overlay the Ly $\alpha$  emission line contours of our cube with an *HST*/STIS image and a *Spitzer*/IRAC 3.6  $\mu\text{m}$  image (see Figure 5.1). Geach et al. (2007) used the same images as well as MIPS 24  $\mu\text{m}$  imaging to identify IRAC counterparts in the LAB1 region. They found five sources, labeled *a-e* in Figure 5.1, of which two (*c* and *d*) have mid-infrared colours inconsistent



with galaxies at  $z = 3.1$ , and therefore are most likely not part of the proto-cluster. The IRAC source  $b$  is located at the southern extreme of LAB1, and the new SAURON observations reveal that it is not coincident with a peak in the Ly $\alpha$  emission (although there is some low-surface brightness emission extending from the north). The two remaining IRAC sources,  $a$  and  $e$ , seem to be related to the Ly $\alpha$  emission. We discuss the Ly $\alpha$  emission blobs in more detail below.

Two of the brightest Ly $\alpha$  emitting regions (C11 and C15) were identified with Lyman Break Galaxies (LBGs) by Steidel et al. (2000). These can be clearly seen in the STIS continuum image. The positional uncertainty between the Ly $\alpha$  emission and continuum detection in the STIS image is less than 1.5 arcsec. C11 is also weakly detected in the IRAC bands (source  $e$ ), with a  $3.6 \mu\text{m}$  flux of  $1.5 \mu\text{Jy}$ . C15 was labeled by Matsuda et al. (2004) as LAB8, as this blob is clearly separated from the main emission halo. Neither C15 nor C11 is detected in X-ray ( $L_X < 2.0 \times 10^{43} \text{ ergs s}^{-1}$ , 2-43 keV band) in the deep *Chandra* exposures of this region (Geach et al. 2009).

The bright Ly $\alpha$  blob R3 is associated with an extremely red galaxy (source  $a$  in Geach et al. 2007) and thought to be the counterpart to a bright submillimeter source detected by Chapman et al. (2001; 2004). This source has an unresolved submillimeter flux of  $S_{850\mu\text{m}} = 16.8 \pm 2.9 \text{ mJy}$  and  $S_{450\mu\text{m}} = 45.1 \pm 15.5 \text{ mJy}$ , measured with the Submillimeter Common-User Bolometer Array (SCUBA). The peak of the Ly $\alpha$  emission of R3 lies within 1.3 arcsec of the submillimeter centroid, and 0.7 arcsec of the IRAC counterpart  $a$ . Higher resolution submillimeter observations with the Submillimeter Array (SMA) (Matsuda et al. 2007) yielded no detection, and hinted that the submillimeter emission could originate from an extended starburst component on scales of  $>4$  arcseconds ( $>30 \text{ kpc}$ ), and indeed this source is co-incident with several low-surface brightness UV components in the STIS imaging.

Nearly tentative radio and CO detections (Chapman et al. 2004) further reinforce the view that the submillimeter source is associated with the IRAC source  $a$ , and therefore most likely with Ly $\alpha$  blob R3. Because of the large positional uncertainties on the radio detection, which could be consistent with either the submillimeter source or the cavity in the Ly $\alpha$  emission that separates R3 from R2, we prefer to associate the radio source with the submillimeter source, given the strong association between those identifications in other submillimeter studies (e.g. Ivison et al. 2007). Assuming a modified blackbody spectrum with characteristic temperature  $T_d = 35 \text{ K}$  (Blain, Barnard & Chapman 2003), the observed  $850 \mu\text{m}$  flux corresponds to a bolometric luminosity of  $L_{\text{bol}} = 1.5 \times 10^{13} L_{\odot}$ . If this luminosity arises from starformation alone with a standard IMF (Kennicutt 1998), then

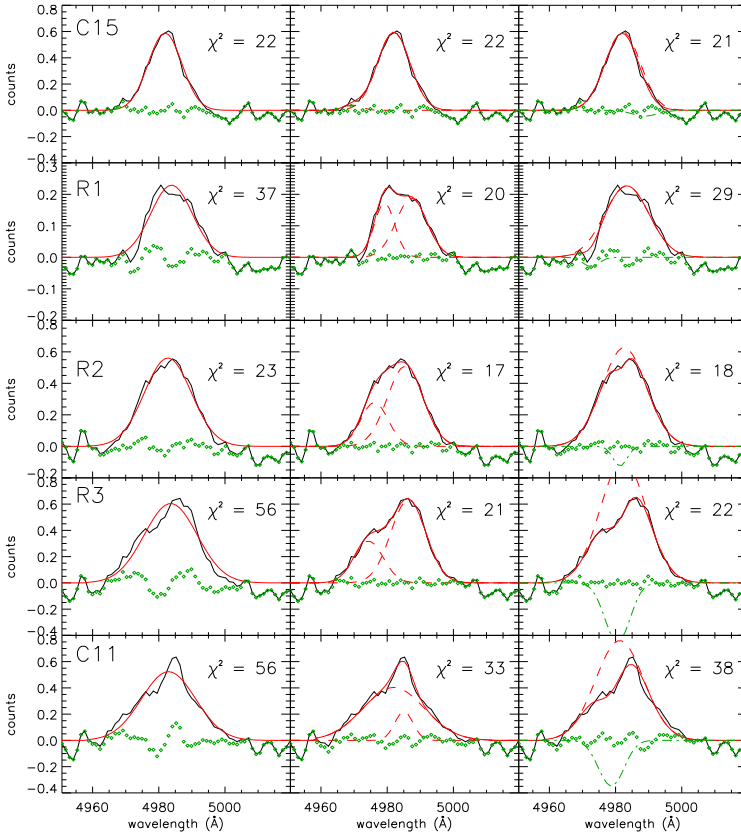


**Figure 5.2** — Single Gaussian (left), double Gaussian (middle) and combined Gaussian emission and Voigt absorption profiles (right) fitted to the spectra in indicated regions of Figure 5.1. Rows show the spectra and fits for different blobs, as indicated in the upper left corner of the left panel. The observed spectra are shown in black, while the fit is overplotted in red. Dashed red lines show Gaussian profiles, and in the right hand panels the green dotted-dashed line indicates the absorber. The green dots show the residuals of the fit. All fits have been convolved with the instrumental dispersion profile of  $108 \text{ km s}^{-1}$ . See Table 5.2 for the fitted parameters.

the implied star formation rate (SFR) is  $\sim 2500 M_{\odot} \text{ yr}^{-1}$ . We note that an AGN contribution in LAB1 is not likely to significantly affect this result: LAB 1 is not detected in a 400 ks *Chandra* exposure, with a luminosity limit  $L_X < 2.4 \times 10^{43} \text{ ergs s}^{-1}$  in the 2–32 keV band (Geach et al. 2009). The radio source has a flux of  $44.4 \mu\text{Jy}$  (Chapman et al. 2004), which is too weak to contribute significantly. The most likely scenario is that source *a* is dominated by a dusty, potentially extended, starburst.

In contrast to C11, C15 and R3, the Ly $\alpha$  emission regions R1 and R2 do not appear to have either an optical or a mid-infra red counterpart (down to a 3.6  $\mu\text{m}$  flux of  $< 1\mu\text{Jy}$ ). Given the depth of the IRAC imaging of this field it seems unlikely that these sources are identified with a dust obscured galaxy. Although offsets of several arcseconds are also seen in the field Ly $\alpha$  emission survey of Matsuda et al. (2004), analysis of the optical to mid-IR colours suggests that the nearest IRAC source  $d$  is not part of the proto-cluster system. An appealing possibility is therefore that components R1 and R2 are genuinely associated with gas trapped in the proto-cluster potential, as they reside at the same velocity as the other components and show no clear signs of outflow (see § 5.3.3).

### 5.3.2 Emission line profiles

One of the principle goals of our deeper observations was to analyse the structure of LAB1 as a function of wavelength in search of outflows and coherent absorption line systems, such as seen in LAB2 (Wilman et al. 2005). To analyse the line profiles, we bin the spectra of each blob in a square region centred on the emission peak. Each square has sides of 4 arcsec, except for the smaller blob R1, where we used a square with sides of 2.4 arcsec (Figure 5.1). We initially fit the resulting spectra with a single Gaussian emission line, but with the exception of C15 and R2 this provides a poor fit to the data. Better fits are obtained by instead modeling the line shape with a double Gaussian or a Gaussian emission profile combined with a Voigt absorption profile (for details of the fitting procedure see Wilman et al. 2005). In the case of absorption, the wavelength of the underlying Gaussian profile and Voigt profile are allowed to vary freely, but we found that if we allowed both the column density and equivalent width of the absorption to vary, the solutions were too degenerate because of their position on the curve of growth. We therefore fixed the column density at  $3 \times 10^{14} \text{ cm}^{-2}$ , typical of the range of the fits when this parameter was left free.

As Figure 5.2 shows, a clear improvement (a change in  $\chi^2$  larger than  $3\sigma$ ) for R1, R3 and C11 is obtained by including the absorber, or by allowing multiple Gaussian components. For R2, the fit improves, but the improvement in  $\chi^2$  is not significant. These fits cannot, however, discern between a situation with multiple emission sources or an absorbing medium.

In Table 5.2 we show the parameters of the best fits. It is remarkable that the redshift of the underlying Gaussian emission lines between the various components is  $z = 3.099 \pm 0.001$  and varies in the restframe by less than 150  $\text{km s}^{-1}$  over the whole region. This supports the interpretation of the LAB1 system as a high-redshift virialised group. The Gaussian line-widths are  $\sigma \sim 400 \text{ km s}^{-1}$ ,

Field	Single Gaussian			Double Gaussian					Gauss + Absorber				
	$z$	$\sigma$ km s <sup>-1</sup>	$\chi^2$	$z_1$	$\sigma_1$ km s <sup>-1</sup>	$z_2$	$\sigma_2$ km s <sup>-1</sup>	$\chi^2$	$z_G$	$\sigma_G$ km s <sup>-1</sup>	$z_A$	$EW_A$ km s <sup>-1</sup>	$\chi^2$
C15	3.098	280	22	3.098	270	3.089	109	21	3.099	294	3.109	379	22
R1	3.100	356	37	3.096	137	3.103	251	20	3.100	385	3.090	100	29
R2	3.099	409	23	3.093	216	3.101	302	17	3.099	386	3.098	20	18
R3	3.100	464	56	3.092	236	3.102	292	21	3.099	399	3.097	275	22
C11	3.099	476	56	3.101	108	3.098	545	33	3.098	422	3.095	280	38

**Table 5.2** — Parameters of the fitted profiles (see Figure 5.2) to the Ly $\alpha$  emission lines in selected regions in LAB1. For the Gaussian profiles we show redshift  $z$  and velocity dispersion  $\sigma$ , and for the Voigt absorber redshift  $z$ , and effective width EW. The column density  $n$  was fixed to  $3 \times 10^{14}$  cm<sup>-2</sup> for each region. The instrumental dispersion ( $\sigma = 108$  km s<sup>-1</sup>) has been taken into account.

measured in the restframe of the cluster, which is a typical value for LABs. In contrast to the case in LAB2 (Wilman et al. 2005) we do not find that the absorption is particularly strong, nor is the redshift of the absorber constant across the system. In LAB2 we used this to argue for the existence of a large-scale absorbing shell of outflowing material. In LAB1 we find no evidence for such a feature: indeed the strength of these putative absorption systems is such that they might well arise in the Lyman-alpha forest surrounding the LAB1 system (Wilman et al. 2004).

### 5.3.3 Kinematic signatures of outflow or rotation

Given that the line profiles are generally better matched by a more complex profile, we investigated the three-dimensional structure of the emission in each of the emission regions. Since we find no strong evidence for absorption, it is likely that the line profiles arise from velocity shear in the emission surrounding each of the systems. In the discussion that follows we will implicitly assume that the shift occurs as a response to the bulk velocity of the emitting gas. The reader should be aware, however, that the line profile has a complex interaction with the gas velocity field as a result of radiative transfer effects (Neufeld 1991; Hansen & Oh 2006; Verhamme, Schaerer & Maselli 2006).

In Figure 5.3 we show kinematic maps of each of the blobs. At each pixel, we fit a single Gaussian emission line to each SAURON spectrum. We show only those lines which have an amplitude-to-noise<sup>1</sup>  $A/N > 3$ . The median velocity of the observed field has been subtracted, in order to reveal any velocity shear that may be indicative of outflow or rotation. We also show the velocity dispersion, corrected for the instrumental dispersion. One spatial sampling element is  $0.4 \times 0.4$  arcsec<sup>2</sup>.

Bower et al. (2004) identified a velocity shear in the C15 system, and this is confirmed in the deeper data. The flow has a peak to peak shear of  $\sim 250$  km s<sup>-1</sup>. The velocity field does not have sufficient spatial resolution to distinguish rotation from outflow (or even inflow). However, the orientation of the shear, perpendicular to the axis of the underlying galaxy, is strongly suggestive of outflows such as those seen in the local starburst galaxy M82 (Shopbell & Bland-Hawthorn 1998; Walter, Weiss & Scoville 2002).

A similar velocity field (but with a substantially higher peak-to-peak shear of  $550$  km s<sup>-1</sup>) is revealed for LBG C11, although in this case the optical source has no clearly identified axis which can help distinguish between rotation and outflow

---

<sup>1</sup>We define amplitude-to-noise as the ratio between the amplitude of the fitted Gaussian emission peak and the noise level of the emission free part of the spectrum.

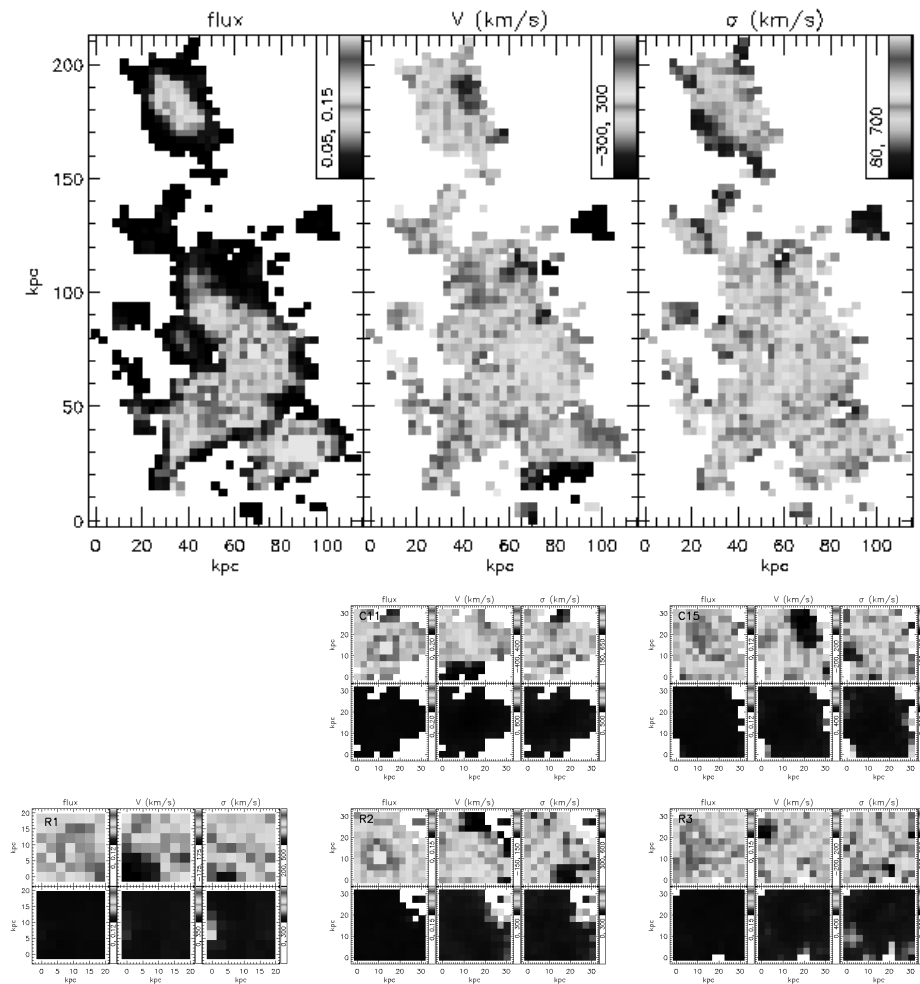


**Figure 5.3** — Kinematic maps of the Ly $\alpha$  gas in LAB1. Top figure shows the total LAB1 region, with from left to right: flux (in arbitrary units), velocity ( $\text{km s}^{-1}$ ) and velocity dispersion ( $\text{km s}^{-1}$ ), obtained by fitting a single Gaussian line to each separate SAURON spectrum. The colour scale is indicated in the upper right corner of each plot, and only lines with amplitude-to-noise  $A/N > 3$  are shown. In the remaining figures we show blow-ups of C11 and C15 (middle row, from left to right) and R1, R2 and R3 (bottom row, from left to right). Top figures of each panel show the kinematic maps (flux, velocity and velocity dispersion), while the bottom figures show on the same colour scale the corresponding error ( $1\sigma$ ) maps, obtained by Monte Carlo simulations. See the colour supplement for a colour version of this figure.

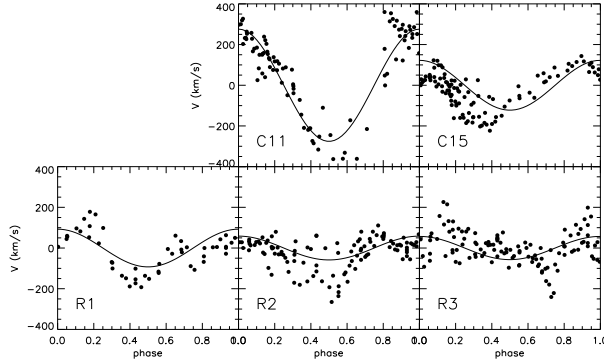


**Figure 5.4** — Rotation signatures in the Ly $\alpha$  regions identified in LAB1. With black dots we show the observed velocities, and the black solid line represents the best cosine fit to the data (see text and Equation 5.1). The regions C11, C15 and R1-R3 are indicated in the lower-left corner for each plot. C11, C15 and possibly R1 show velocity shear signatures, while R2 and R3 do not.

(or inflow). Weaker evidence for velocity shear is also apparent in R1 (peak-to-peak velocity shear of  $\sim 300 \text{ km s}^{-1}$ ), while R2 and R3 show no detectable shear. This is also illustrated in Figure 5.4, where we show fits of the observed velocity field ( $V_{\text{obs}}$ ) with a simple rotation description given by

$$V_{\text{obs}} = V_{\text{rot}} \cos(\phi - \text{PA}). \quad (5.1)$$

Here  $V_{\text{rot}}$  is the amplitude of the rotation and PA the kinematic position angle. The azimuthal angle  $\phi$  was defined in the standard way with respect to a central pixel  $(x_c, y_c)$ . For C11 and C15 we were able to fit for this central pixel, but for R1-R3 the fit was noisier, and instead we fixed  $x_c$  and  $y_c$  to the geometrical centre of the field. These fits show more quantitatively than the velocity maps the absence of a shear pattern in R2 and R3, while C11 and C15 (and to a smaller extent also R1) have clear signatures of velocity shears. Although it is difficult to discern trends on the basis of so few objects (C11 and C15), it seems that outflows are common in the systems where an unobscured galaxy is associated with the source of emission. However, the possibility of inflows also remains (e.g. Villar-Martín et al. 2006). A much larger sample is needed to draw any quantitative conclusions.

It is interesting to note that Shapiro et al. (2008) analysed velocity and dispersion maps of starforming galaxies around  $z \sim 2$ , using the H $\alpha$  emission line. They found that several of their galaxies could be described by rotating discs. Ly $\alpha$  velocity maps are more difficult to interpret, as Ly $\alpha$  is a resonant line and traces the surface of last scattering. While the H $\alpha$  emission line traces the ionised gas in the

galaxy disc, Ly $\alpha$  lines can also probe the large-scale diffuse gas structure. Thus it is likely that the two emission lines probe different gas regimes, and are highly complementary for studying the formation of young galaxies.

## 5.4 Discussion and conclusion

We have presented very deep integral-field spectrograph observations of the LAB1 Ly $\alpha$  emission halo. The deep data allow us to study the spatial and velocity structure of this system in unprecedented detail.

We find that the giant halo is made up from a superposition of four or five distinct blobs, with the emission from these regions accounting for at least 55 per cent of the total diffuse flux. Most of the emission regions are associated with individual galaxies. The regions C15 and C11 are associated with optical Lyman Break Galaxies and region R3 is associated with a bright submillimeter source. While this source is faint in the optical, it is bright at 3.6  $\mu\text{m}$ , suggesting that it is a strongly dust-obscured starforming galaxy. None of these sources are detected at X-ray wavelengths, suggesting that it is unlikely that the emission is powered by an AGN. The regions R1 and R2 are not associated with any optical or IR source, and the emission from these blobs could plausibly come from gas associated with the proto-cluster potential.

The integral-field spectra allow us to examine the emission line profiles and velocity structure in each of the blobs. In R1, R3 and C11, we find that the integrated emission line profiles are not adequately fitted by a single component Gaussian, and that a better fit is obtained with either a two component Gaussian or the combination of a Gaussian emission and Voigt absorption line profile. We find that the underlying emission has a velocity centroid that is extremely similar from region to region, reinforcing the idea that the LAB1 system is a virialised group with velocity dispersion  $\sim 100 \text{ km s}^{-1}$ . However, in contrast to the LAB2 system, we find no evidence for a coherent shell of absorption that covers the entire system. Any absorption features are significantly weaker than those seen in LAB2, so that they might arise in the large-scale structure foreground to the proto-cluster.

C15, C11 and possibly R1 show evidence of coherent velocity shear arising from an outflow or rotation. In C15 the velocity gradient is perpendicular to the morphology of the underlying galaxy, consistent with the pattern expected for an outflowing galactic wind. In the other systems the relation between the velocity field and the underlying galaxy is unclear. The velocity shear is largest in C11 where it is  $\sim 550 \text{ km s}^{-1}$  over approximately 25 kpc. The implied outflow velocity



is comparable with that seen in many other Lyman break systems, and does not suggest that the sources seen in LAB1 are undergoing unusually strong feedback.

The primary motivation for these observations was to discover whether the coherent absorption systems such as seen by Wilman et al. (2005) in LAB2 are a ubiquitous feature. These observations have shown that they are not. The data for LAB2 are best interpreted as a large-scale super-bubble of material that has been expelled by a high power, perhaps explosive feedback event. The two LAB system both seem to be made up of smaller emission clouds. So why does the absorption pattern in LAB1 and LAB2 differ? One possible answer is that a similar event has occurred in LAB1 in the past, but that the shell has now broken up, or is sufficiently blue shifted that it cannot be seen in absorption against the system's Ly $\alpha$  emission. Another explanation might be that LAB1 is a younger system in which the large scale outflow is yet to develop. This seems unlikely, however, since we see no signs of spectacular outflows associated with the individual emission systems. Now that we have dissected the giant emission halo into a number of smaller systems, these seem quite comparable to the many radio quiet LAB systems identified by Matsuda et al. (2004). In many ways, the composite system represents a microcosm of diffuse Ly $\alpha$  emission in general, with the systems reflecting a diversity of power sources. Geach et al. (2009) favour photo-ionisation as the principle power source for LABs. This fits in well with C11, C15 and R3 (if we allow for the possibility that it is only so strongly obscured along our line of sight). However, this appears to describe the R1/R2 emission less well. Possibly the emission from this part of the system is much more closely related to the emission seen around radio galaxies (Chambers et al. 1990; Villar-Martín et al. 2002) and (perhaps) in local cooling flow clusters (Johnstone & Fabian 1988).

## Acknowledgments

It is a pleasure to thank Michele Cappellari, Eveline van Scherpenzeel, Chris Benn and the ING staff for support on La Palma. We gratefully acknowledge Huub Röttgering, Joop Schaye, Kristen Shapiro and Ian Smail for fruitful discussions, and Roland Bacon and Eric Emsellem for their help in the initial stages of this project.

This research was supported by the Netherlands Research School for Astronomy NOVA, and by the Netherlands Organization of Scientific Research (NWO) through grant 614.000.426. AW acknowledges The Leids Kerkhoven-Bosscha Fonds and the European Southern Observatory for contributing to working visits. AMS and JEG acknowledge support from an STFC fellowship.

The SAURON observations were obtained at the William Herschel Telescope, operated by the Isaac Newton Group in the Spanish Observatorio del Roque de los Muchachos of the Instituto de Astrofísica de Canarias.

## Colour figures

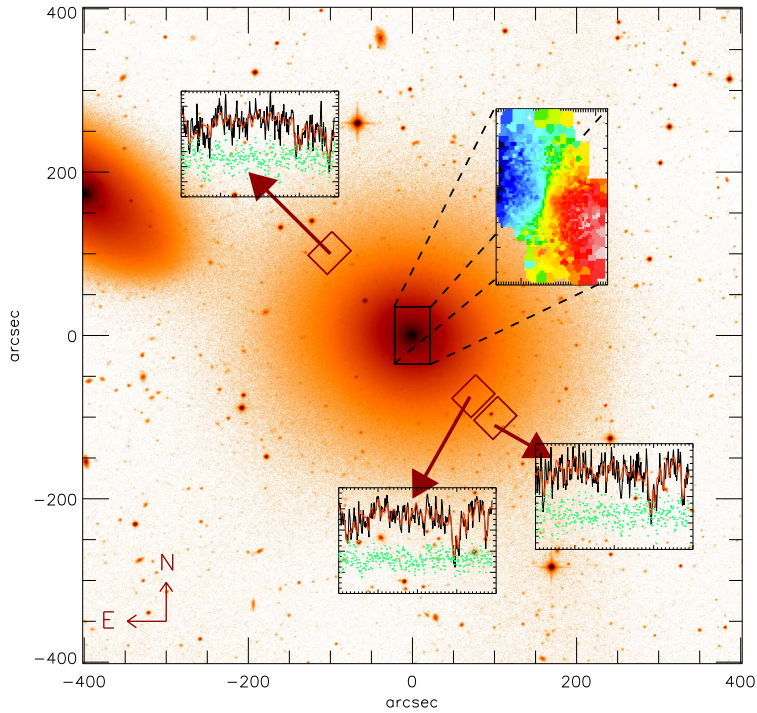


**Figure 1.3** — Illustration of the usage of SAURON as a 'photon-collector'. The underlying red image is a V-band image of early-type galaxy NGC 3379. In the central part of the galaxy,  $S/N$  in individual spectra is high, and we can construct kinematic maps, where binning of spectra is only needed along the edges of the field-of-view (FoV), where the galaxy is fainter. At large radii ( $3$  and  $4 R_e$ ) we bin the light of all spectra within the SAURON FoV together, in order to obtain a spectrum with sufficient  $S/N$  to measure the stellar kinematics.

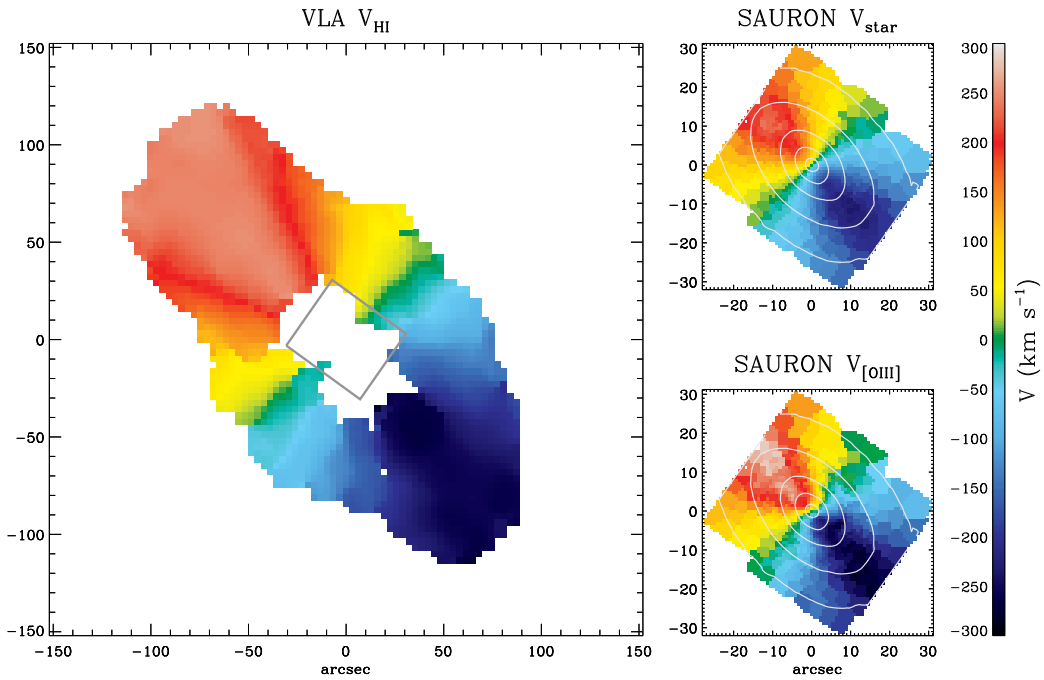


**Figure 2.2** — Velocity maps of the neutral hydrogen (VLA) and ionised gas and stars (SAURON) in NGC 2974. Both the stars and the neutral and ionised gas are well aligned. The maps are orientated so that North is up and East is to the left. The grey box in the VLA map encloses the SAURON fields shown at the right.

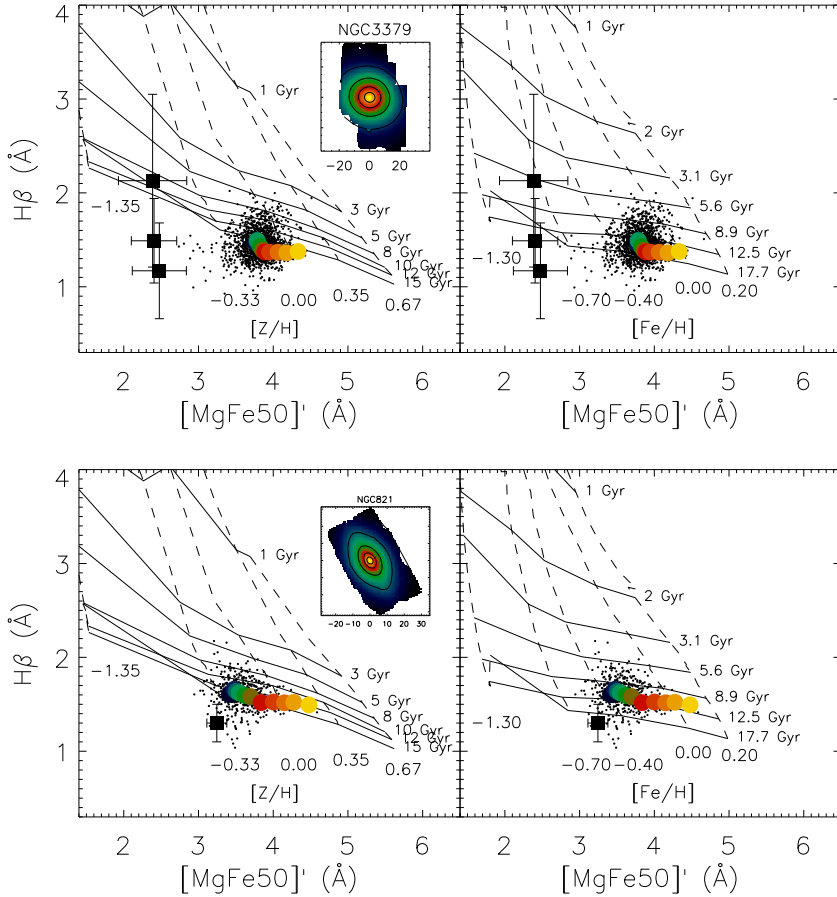


**Figure 3.9** —  $H\beta$  index against  $[MgFe50]'$  (both in Å) in NGC 3379 (top) and NGC 821 (bottom). Left panels show the Thomas et al. (2003) stellar population models (solid and dashed lines) and right panels the Schiavon (2007) models. Black dots indicate measurements from the SAURON central field, while the coloured dots are averaged along isophotes (see inset for colour coding). The black filled squares show the data at large radii, revealing an old (12 Gyr) and metal-poor (below 20 per cent solar metallicity) population for both models, though the uncertainties in these values are large.

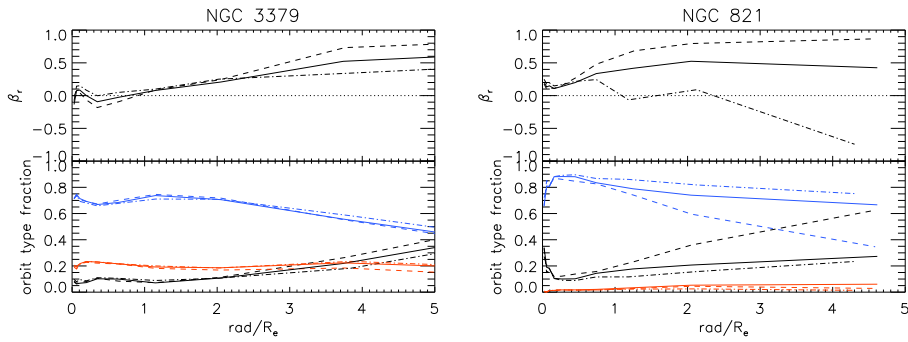


**Figure 3.15** — Orbital structure in NGC 3379 (left) and NGC 821 (right). Top panel: velocity anisotropy  $\beta_r$  as a function of radius (see Equation 3.9). The lines are as in Figures 3.12 and 3.14, with the solid line for our best-fit model, the dashed line for the model without halo and the dashed-dotted line for the model with the too heavy halo. Bottom panel: fraction of orbit types as a function of radius for the models of the top panel. Blue lines denote the fractions of short axis tubes, red the fractions of long axis tubes and black the fractions of box orbits.

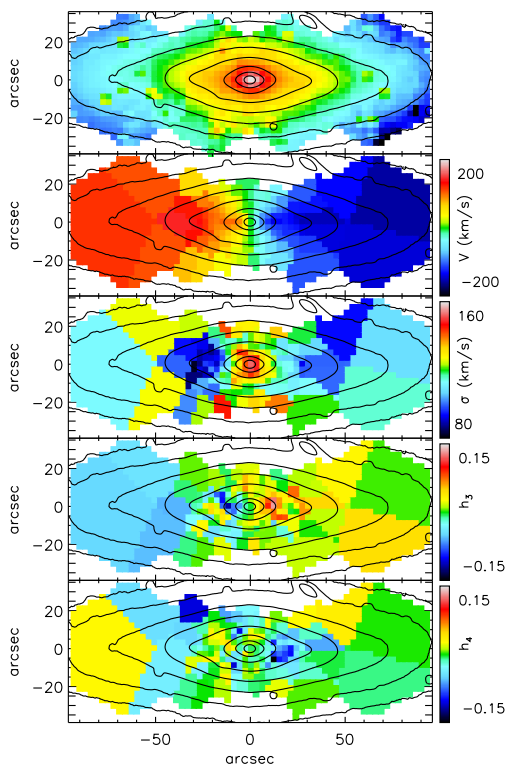


**Figure 4.3** — Stellar kinematics extracted from the PPAK spectra of NGC 2549. From top to bottom: total flux, velocity, velocity dispersion,  $h_3$  and  $h_4$ . The maps are orientated such that North is to the left and East is down.

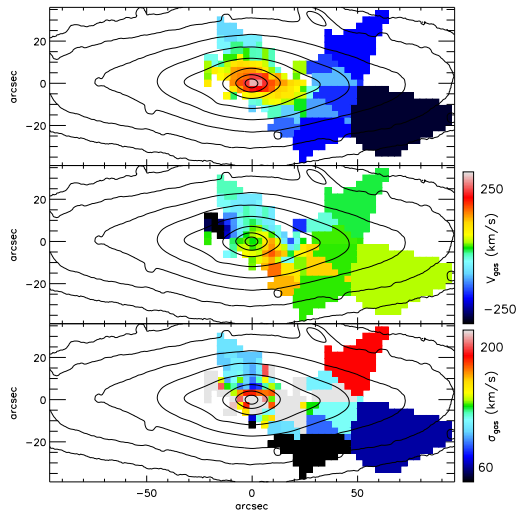


**Figure 4.5** — Gas kinematics of NGC 2549, measured from [O III]. From top to bottom: flux, velocity and velocity dispersion. Only bins with amplitude-to-noise  $A/N > 4$  are shown. Maps are orientated as in Figure 4.3.

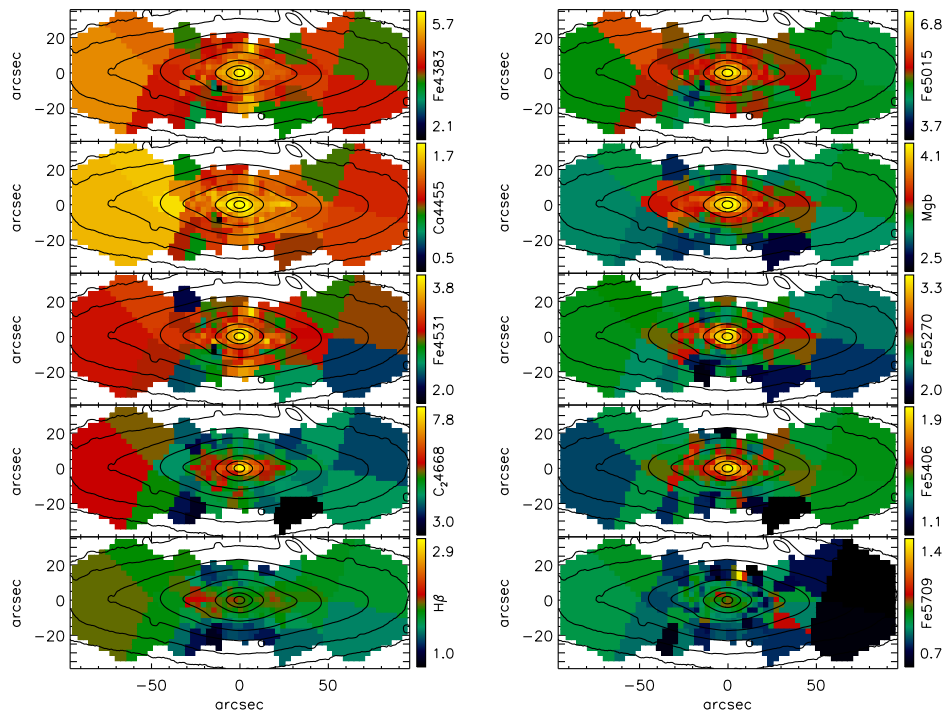


**Figure 4.7** — Line strength maps of NGC 2549. Maps are orientated such that North is to the left and East down. The Fe5335 line strength map has been omitted, as this index was affected by a bad column on the CCD and could therefore not be reliably measured.

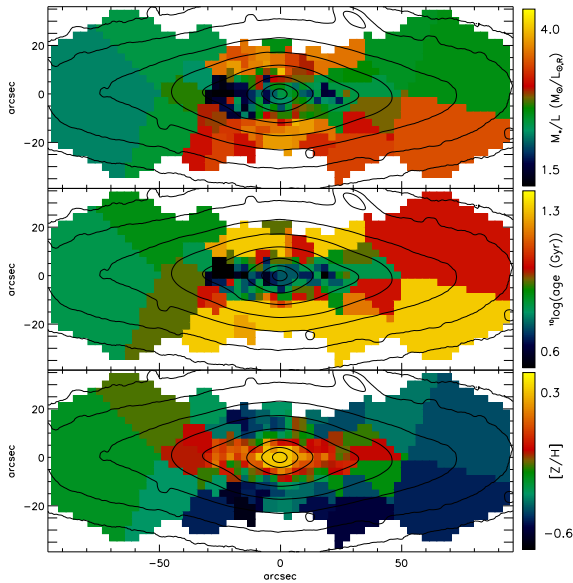


**Figure 4.8** — From top to bottom: stellar mass-to-light ratio ( $M_*/L$ ) in  $R$ -band, age and metallicity ( $[Z/H]$ ) in NGC 2549. Maps are again orientated with North to the left and East down.

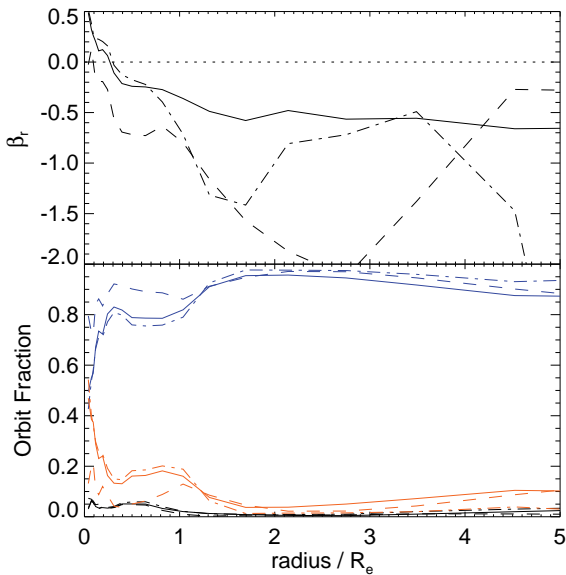


**Figure 4.12** — Orbital structure of NGC 2549. Top panel: velocity anisotropy  $\beta_r$  as a function of radius (see Equation 3.9). The solid line indicates our best-fitting model ( $M_{200} = 7 \times 10^{12} M_\odot$ ), the dashed and dashed-dotted line denote the model without halo and the model with a too heavy halo ( $M_{200} = 3 \times 10^{13} M_\odot$ ), respectively. Bottom panel: fraction of orbit types as function of radius for the models of the top panel. Blue lines denote fractions of short axis tubes, red lines long axis tubes and black lines the fractions of box orbits.



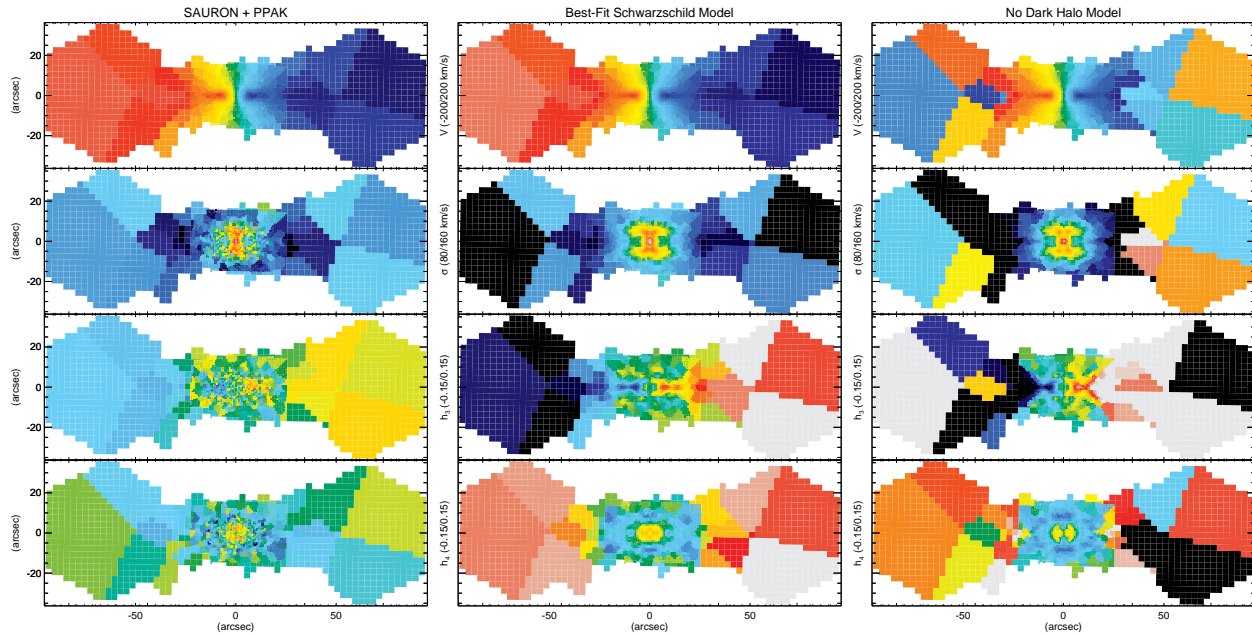


**Figure 4.11** — Point-symmetrized kinematics of the SAURON and PPAK data and the best-fitting model with a spherical NFW halo. The model reproduces the flat rotation curve well, but has trouble reproducing the rising dispersion at radii larger than 40 arcseconds. Consequently, the higher moment at those radii cannot be reproduced either. The model without a dark halo cannot reproduce the observed rotation field, and is overall a poor fit to the data.

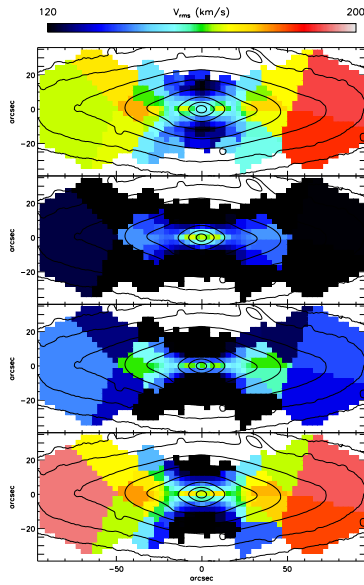


**Figure 4.13** — Jeans anisotropic models of NGC 2549, based on the second velocity moments of the PPAK kinematics. From top to bottom: bi-symmetrized observations, model without dark halo and  $\beta_z = 0.17$ , model without dark halo with  $\beta_z = 0.17$  for  $R < 20$  arcsec and  $\beta_z = -10$  for  $R > 20$  arcsec, and the finally the best-fitting model with an NFW halo and  $\beta_z = 0.17$ .

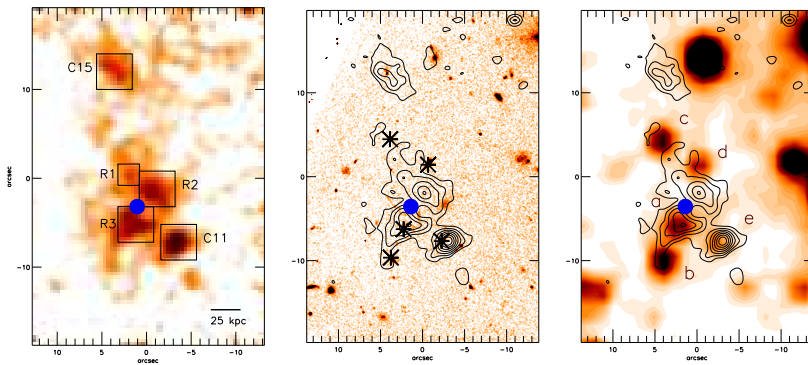


**Figure 5.1** —  $\text{Ly}\alpha$  emission in the LAB1 region. Left panel: continuum subtracted  $\text{Ly}\alpha$  emission, obtained from collapsing the SAURON spectra over a narrow wavelength range centred on the emission line. Interesting regions are indicated by boxes (see text). Middle panel: *HST/STIS* optical image overlaid with  $\text{Ly}\alpha$  contours from the left panel. Black asterisks indicate the IRAC sources from Geach et al. (2007). Right panel: same as middle panel, but now a *Spitzer/IRAC*  $3.6 \mu\text{m}$  image is displayed. Sources identified in Geach et al. (2007) are indicated with identical nomenclature (a-e). In all plots, the blue dot denotes the position of the radio source (Chapman et al. 2004). All images are plotted on the same scale and are orientated such that North is up and East to the left.

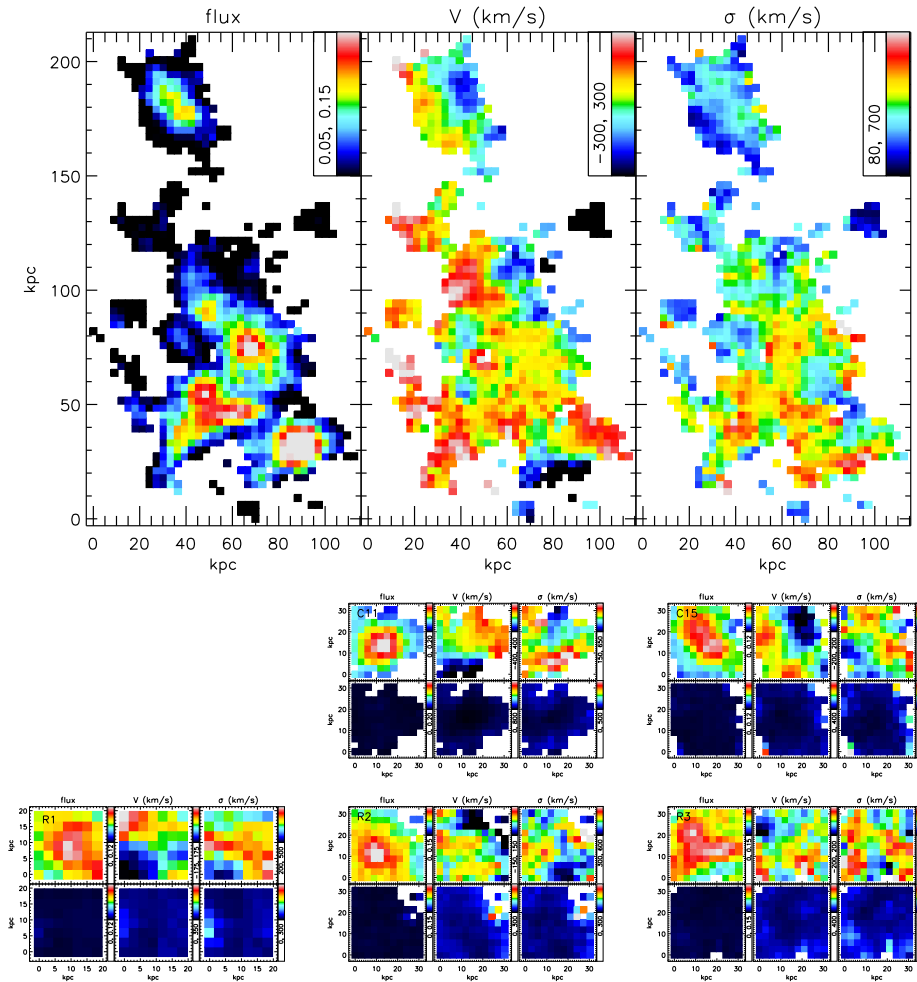


**Figure 5.3** — Kinematic maps of the Ly $\alpha$  gas in LAB1. Top figure shows the total LAB1 region, with from left to right: flux (in arbitrary units), velocity ( $\text{km s}^{-1}$ ) and velocity dispersion ( $\text{km s}^{-1}$ ), obtained by fitting a single Gaussian line to each separate SAURON spectrum. The colour scale is indicated in the upper right corner of each plot, and only lines with amplitude-to-noise  $A/N > 3$  are shown. In the remaining figures we show blow-ups of C11 and C15 (middle row, from left to right) and R1, R2 and R3 (bottom row, from left to right). Top figures of each panel show the kinematic maps (flux, velocity and velocity dispersion), while the bottom figures show on the same colour scale the corresponding error ( $1\sigma$ ) maps, obtained by Monte Carlo simulations.



# Bibliography

- Bacon R., et al., 2001, MNRAS, 326, 23
- Barnabe M., Czoske O., Koopmans L., Treu T., Bolton A., Gavazzi R., 2009, MNRAS, in press (arXiv0904.3861)
- Begeman K.G., 1978, PhD thesis, Groningen University
- Begeman K.G., Broeils A.H., Sanders R.H., 1991, MNRAS, 249, 523
- Benn, C.R., Ellison, S.L., 1998, NewAr, 42, 503
- Bertola F., Pizzella A., Persic M., Salucci P., 1993, ApJ, 416L, 45
- Binney J., Mamon G.A., 1982, MNRAS, 200, 361
- Binney J., Tremaine S., 2008, Galactic Dynamics, second edition. Princeton Univ. Press, Princeton N.J.
- Blain A.W., Barnard V.E., Chapman S.C., 2003, MNRAS, 338, 733
- Bower R.G., et al., 2004, MNRAS, 351, 63
- Bregman J.N., Hogg D.E., Roberts M.S., 1992, ApJ, 387, 484
- Bridges T., et al., 2006, MNRAS, 373, 157
- Bruzual G., Charlot S., 2003, MNRAS, 344, 1000
- Bullock J.S., Kolatt T.S., Sigad Y., Somerville R.S., Kravtsov A.V., Klypin A.A., Primack J.R., Dekel A., 2001, MNRAS, 321, 559
- Capaccioli M., Vietri M., Held E.V., Lorenz H., ApJ, 1991, 371, 535
- Cappellari M., 2002, MNRAS, 333, 400
- Cappellari M., Verolme E.K., van der Marel R.P., Verdoes Kleijn G.A., Illingworth G.D., Franx M., Carollo C.M., de Zeeuw P.T., 2002, ApJ, 371, 535
- Cappellari M., Copin Y., 2003, MNRAS, 342, 345
- Cappellari M., Emsellem E., 2004, PASP, 116, 138
- Cappellari M., et al., 2006, MNRAS, 366, 1126
- Cappellari M., et al., 2007, MNRAS, 379, 418
- Cappellari M., 2008, MNRAS, 390, 71
- Carlberg R.G., 1984, ApJ, 286, 403
- Carollo C.M., de Zeeuw P.T., van der Marel R.P., Danziger I.J., Qian E.E., 1995, ApJ, 441, L25
- Casertano S., van Gorkom J.H., 1991, AJ, 101, 1231
- Catinella B., Giovanelli R., Haynes M.P., 2006, ApJ, 640, 751
- Cayatte V., Kotanyi C., Balkowski C., van Gorkom J.H., 1994, AJ, 107, 1003
- Chambers K.C., Miley G.K., van Breugel W.J.M., 1990, ApJ, 363, 21
- Chapman S.C., Lewis G.F., Scott D., Richards E., Borys C., Steidel C.C., Adelberger K.L., Shapley A.E., 2001, 548, 17
- Chapman S.C., Scott D., Windhorst R.A., Frayer D.T., Borys C., Lewis G.F., Ivison R.J., 2004, ApJ, 606, 85
- Cinzano P., van der Marel R.P., 1994, MNRAS, 270 325
- Cocato L., et al., 2009, MNRAS, 394, 1249
- Côté P., McLaughlin D.E., Cohen J.G., Blakeslee J.P., 2003, ApJ, 591, 850
- Davies R.L., Sadler E.M., Peletier R.F., 1993, MNRAS, 262, 650
- de Blok W.J.G. & Bosma A., 2002, A&A, 385, 816
- de Blok W.J.G., 2005, ApJ, 634, 227
- de Blok W.J.G., Walter F., Brinks E., Trachternach C., Oh S.-H., Kennicutt R.C., 2008, AJ, 136, 2648
- Dekel A., Stoehr F., Mamon G.A., Cox T.J., Novak G.S., Primack J.R., 2005, Nature, 437, 707
- de Lorenzi F., et al., 2009, MNRAS, 395, 76
- de Zeeuw P.T., et al., 2002, MNRAS, 329, 513
- Dijkstra M., Haiman Z., Spaans M., ApJ, 649, 14
- Dijkstra M., Loeb A., 2009, MNRAS, submitted (arXiv0902.2999)

- Di Matteo P., Pipino A., Lehnert M.D., Combes F., Semelin B., 2009, *A&A*, 499, 427
- Douglas N.G., et al., 2002, *PASP*, 114, 1234
- Douglas N.G., et al., 2007, *ApJ*, 664, 257
- Emsellem E., Monnet G., Bacon R., 1994, *A&A*, 285, 723
- Emsellem E., Goudfrooij P., Ferruit P., 2003, *MNRAS*, 345, 1297
- Emsellem E., et al., 2004, *MNRAS*, 352, 721
- Emsellem E., et al., 2007, *MNRAS*, 379, 401
- Evans N.W., de Zeeuw P.T., 1994, *MNRAS*, 271, 202
- Famaey B., Binney J., 2005, *MNRAS*, 363, 603
- Famaey B., Gentile G., Bruneton J.-P., Hongsheng, 2007, *PhRvD*, 75, 3002
- Fardal M.A., Katz N., Gardner J.P., Hernquist L., Weinberg D.H., Davé R., 2001, *ApJ*, 562, 605
- Ferland G.J., Fabian A.C., Hatch N.A., Johnstone R.M., Porter R.L., van Hoof P.A.M., Williams R.J.R., 2009, *MNRAS*, 392, 1475
- Forestell A., Gebhardt K., 2008, arXiv0803.3626
- Franx M., Illingworth G., 1990, *ApJ*, 359L, 41
- Franx M., van Gorkom J.H., de Zeeuw P.T., 1994, *ApJ*, 436, 642
- Freedman W.L., et al., 2001, *ApJ*, 553, 47
- Frenk C.S., White S.D.M., Davis M., Efstathiou G., 1988, *ApJ*, 327, 507
- Gavazzi R., Treu T., Rhodes J.D., Koopmans L.V.E., Bolton A.S., Burles S., Massey R.J., Moustakas L.A., 2007, *ApJ*, 436, 176
- Geach J.E., et al., 2005, *MNRAS*, 363, 1398
- Geach J.E., Smail I., Chapman S.C., Alexander D.M., Blain A.W., Stott J.P., Ivison R.J., 2007, *ApJ*, 655L, 9
- Geach J.E., et al., 2009, *ApJ*, 700, 1
- Gerhard O.E., 1993, *MNRAS*, 265, 231
- Gerhard O., Kronawitter A., Saglia R.P., Bender, R., 2001, *AJ*, 121, 1936
- Haiman Z., Spaans M., Quataert E., 2000, *ApJ*, 537, 5
- Hansen M., Oh S.P., 2006, *MNRAS*, 367, 979
- Håring-Neumayer N., Cappellari M., Rix H.-W., Hartung M., Prieto M.A., Meisenheimer K., Lenzen R., 2006, *ApJ*, 643, 226
- Hayashi E., Navarro J.F., Springel V., 2007, *MNRAS*, 377, 50
- Heckman T.M., Armus L., Miley G.K., 1990, *ApJS*, 74, 833
- Hopkins P.F., Cox T.J., Dutta S.N., Hernquist L., Kormendy J., Lauer T.R., 2009a, *ApJS*, 181, 135
- Hopkins P.F., Lauer T.R., Cox T.J., Hernquist L., Kormendy J., 2009b, *ApJS*, 181, 486
- Humphrey P.J., Buote D.A., Gastaldello F., Zappacosta L., Bullock J.S., Brighenti F., Mathews W.G., 2006, *ApJ*, 646, 899
- Hunter C., de Zeeuw P.T., 1992, *ApJ*, 389, 79
- Ivison R.J., et al., 2007, *MNRAS*, 380, 199
- Jeong H., Bureau M., Yi S.K., Krajnović D., Davies R.L., 2006, *MNRAS*, 2007, 376, 1021
- Johnstone R.M., Fabian A.C., 1988, *MNRAS*, 233, 581
- Kauffmann G., van den Bosch F., 2002, *SciAm*, 286, 36
- Kelz A., et al., 2006, *PASP*, 118, 129
- Kennicutt R.C., 1998, *ApJ*, 498, 541
- Kent S.M., de Zeeuw P.T., 1991, *AJ*, 102, 1994
- Kim D.-W., Jura M., Guhathakurta P., Knapp G.R., van Gorkom J.H., 1988, *ApJ*, 330, 684
- Kobayashi C., 2004, *MNRAS*, 347, 740
- Komatsu E., et al., 2009, *ApJS*, 180, 330
- Koopmans L.V.E., Treu T., Bolton A.S., Burles S., Moustakas L.A., 2006, *ApJ*, 649, 599
- Krajnović D., Cappellari M., Emsellem E., McDermid R.M., de Zeeuw P.T., 2005, *MNRAS*, 357, 1113
- Krajnović D., Cappellari M., de Zeeuw P.T., Copin Y., 2006, *MNRAS*, 366, 787
- Krajnović D., et al., 2008, *MNRAS*, 390, 93
- Krajnović D., McDermid R.M., Cappellari M., Davies R.L., 2009, *MNRAS*, submitted
- Kroupa P., 2001, *MNRAS*, 322, 231
- Kuijken K., Tremaine S., 1991, in Sundelius B., ed., *Dynamics of Disc Galaxies*. Göteborg Univ. Press, Göteborg, p.71
- Kuntschner H., 2000, *MNRAS*, 315, 184

- Kuntschner H., et al., 2006, MNRAS, 369, 497  
Maraston C., 2005, MNRAS, 362, 799  
Matsuda Y., et al., 2004, AJ, 128, 569  
Matsuda Y., Iono D., Ohta K., Yamada T., Kawabe R., Hayashino T., Peck A.B., Petitpas G.R., 2007, ApJ, 667, 667  
McDermid R.M., 2002, PhD thesis, University of Durham  
McDermid R.M., et al., 2006, MNRAS, 373, 906  
Mei S., et al., 2005, ApJ, 625, 121  
Milgrom M., 1983, ApJ, 270, 365  
Morganti R., Sadler E.M., Oosterloo T., Pizzella A., Bertola F., 1997, AJ, 113, 937  
Morganti, R., et al., 2006, MNRAS, 371, 157  
Navarro J.F., Frenk C.S., White S.D., 1996, ApJ, 462, 563  
Napolitano N.R., et al., 2009, MNRAS, 393, 329  
Neufeld, D.A., 1991, ApJ, 370L, 85  
Nilsson K.K., Fynbo J.P.U., Møller P., Sommer-Larsen J., Ledoux C., 2006, A&A, 452, 23  
Noordermeer E., van der Hulst J.M., Sancisi R., Swaters R.S., van Albada T.S., 2007, MNRAS, 376, 1513  
Norris M.A., Sharples R.M., Kuntschner H., 2006, MNRAS, 367, 815  
Ohyama Y., et al., 2003, ApJ, 591, 9  
Oosterloo T.A., Morganti R., Sadler E.M., Vergani D., Caldwell N., 2002, AJ, 371, 729  
Oosterloo T.A., Morganti R., Sadler E.M., van der Hulst T., Serra P., 2007, A&AA, 465, 787  
O'Sullivan E., Ponman T.J., 2004, MNRAS, 354, 935  
Pellegrini S., Ciotti L., 2006, MNRAS, 354, 1797  
Pierce M., et al., 2006, MNRAS, 366, 1253  
Proctor R.N., Forbes D.A., Forestell A., Gebhardt K., 2005, MNRAS, 362, 857  
Qian E.E., de Zeeuw P.T., van der Marel R.P., Hunter C., 1995, MNRAS, 274, 602  
Richstone D.O., Tremaine S., 1984, ApJ, 286, 27  
Rix H.-W., de Zeeuw P.T., Cretton N., van der Marel R.P., Carollo C.M., 1997, ApJ, 488, 702  
Romanowsky A.J., Douglas N.G., Arnaboldi M., Kuijken K., Merrifield M.R., Napolitano N.R., Capaccioli M., Freeman K.C., 2003, Science, 301, 1696  
Rubin, V.C., Burstein, D., Ford, W.K., Jr., Thonnard, N., 1985, ApJ, 289, 81  
Sadler E.M., Oosterloo T.A., Morganti R., Karakas A., 2000, AJ, 119, 1180  
Sambhus N., Gerhard O, Méndez R.H., 2006, AJ, 131, 837  
Sánchez S.F., Aceituno J., Thiele U., Pérez-Ramírez D., Alves J., 2007, PASP, 119, 1186  
Sánchez-Blázquez P., et al., 2006, MNRAS, 371, 703  
Sánchez-Blázquez P., Forbes D.A., Strader J., Brodie J., Proctor R., 2007, MNRAS, 377, 759  
Sánchez-Blázquez P., et al., 2009, A&A, 499, 47  
Sanders R.H., McGaugh S.S., 2002, ARA&A, 40, 263  
Sanders R.H., Noordermeer E., 2007, MNRAS, 379, 702  
Sandin C., et al., 2009, PASP, submitted  
Sarzi M., et al., 2006, MNRAS, 366, 1151  
Sault, R.J., Teuben, P.J., Wright, M.C.H. 1995, in ADASS IV, ed. R. Shaw, H.E. Payne, J.J.E. Hayes, ASP Conf. Ser., 77, 433,  
Schiavon R.P., 2007, ApJS, 171, 146  
Schoenmakers R.H.M., 1998, ASPC, 136, 240  
Schoenmakers R.H.M., Franx M., de Zeeuw P.T., 1997, MNRAS, 292, 349  
Schwarzschild M., 1979, ApJ, 232, 236  
Schweizer F., 1986, Science, 231, 227  
Scott N., et al., 2009, MNRAS, in press (arXiv0906.3321)  
Serra P., Trager S.C., van der Hulst J.M., Oosterloo T.A., Morganti R., 2006, A&A, 453, 493  
Shapiro K.L., Cappellari M., de Zeeuw P.T., McDermid R.M., Gebhardt K., van den Bosch R.C.E., Statler T.S., 2006, MNRAS, 370, 559  
Shapiro K.L., et al., 2008, ApJ, 682, 231  
Shopbell P.L., Bland-Hawthorn J., 1998, ApJ, 493, 129  
Smith D.J.B., Jarvis M.J., MNRAS, 378, L49  
Smith D.J.B., Jarvis M.J., Lacy M., Martínez-Sansigre A., 2008, MNRAS, 389, 799

- Soucail G., Mellier Y., Fort B., Mathez G., Cailloux M., 1988, *A&A*, 191L, 19
- Spekkens K., Giovanelli R., 2006, *AJ*, 132, 1426
- Spolaor M., Proctor R.N., Forbes D.A., Couch W.A., 2009, *ApJ*, 691L, 138
- Springel V., et al., 2005, *Nature*, 435, 629
- Statler T.S., Smecker-Hane T., 1999, *AJ*, 117, 839
- Statler T.S., 2001, *AJ*, 121, 244
- Steidel C.S., Adelberger K.L., Shapley A.E., Pettini M., Dickinson M., Giavalisco K., 2000, *ApJ*, 532, 170
- Swinbank A.M., Bower R.G., Smith G.P., Smail I., Kneib J.-P., Ellis R.S., Stard D.P., Bunker A.J., 2006, *MNRAS*, 368, 1631
- Taniguchi Y., Shioya Y., 2000, *ApJ*, 532, 13
- Thomas D., Maraston C., Bender R., 2003, *MNRAS*, 339, 897
- Thomas J., Saglia R.P., Bender R., Thomas D., Gebhardt K., Magorrian J., Corsini E.M., Wegner G., 2007, *MNRAS*, 382, 657
- Thomas J., et al., 2009, *MNRAS*, 393, 641
- Tonry J.L., Dressler A., Blakeslee J.P., Ajhar E.A., Fletcher A.B., Luppino G.A., Metzger M.R., Moore C.B., 2001, *ApJ*, 546, 681
- Trager S.C., Worthey G., Faber S.M., Burstein D., González J.J., 1998, *ApJS*, 116, 1
- van Albada T.S., Bahcall J.N., Begeman K., Sancisi R., 1985, *ApJ*, 295, 305
- van den Bosch F.C., Robertson B.E., Dalcanton J.J., de Blok W.J.G., 2000, *AJ*, 119, 1579
- van den Bosch R.C.E., van de Ven G., Verolme E.K., Cappellari M., de Zeeuw P.T., 2008, *MNRAS*, 385, 647
- van den Bosch R.C.E., van de Ven G., 2009, *MNRAS*, in press (arXiv0811.3474)
- van den Bosch R.C.E., de Zeeuw P.T., 2009, *MNRAS*, submitted
- van de Ven G., de Zeeuw P.T., van den Bosch R.C.E., 2008a, *MNRAS*, 385, 614
- van de Ven G., Falcón-Barroso J., McDermid R.M., Cappellari M., Miller B.W., de Zeeuw P.T., 2008b, *ApJ*, submitted (arXiv0807.4175)
- van der Kruit P.C., Allen R.J., 1978, *ARA&A*, 16, 103
- van Starkenburg L., van der Werf P.P., Franx M., Labbé I., Rudnick G., Wuyts S., 2008, *A&A*, 488, 99
- Vazdekis A., et al., 2007, in Vazdekis A., Peletier R.F., ed., *Proc. IAU Symp. 241, Stellar Populations as Building Blocks of Galaxies*. Cambridge University Press, Cambridge, p. 133
- Verhamme A., Schaerer D., Maselli A., 2006, *A&A*, 460, 397
- Villar-Martín M., Vernet J., di Serego Alighieri S., Fosbury R., Pentericci L., Cohen M., Goodrich R., Humphrey A., 2002, *MNRAS*, 336, 436
- Villar-Martín M., et al., 2006, *MNRAS*, 366L, 1
- Walter F., Weiss A., Scoville N., 2002, *ApJ*, 580L, 21
- Weijmans A., Krajnović D., van de Ven G., Oosterloo T.A., Morganti R., de Zeeuw P.T., 2008, *MNRAS*, 383, 1343 (Chapter 2)
- Weijmans A., et al., 2009a, *MNRAS*, in press (arXiv0906.0018) (Chapter 3)
- Weijmans A., Bower R.G., Geach J.E., Swinbank A.M., Wilman R.J., de Zeeuw P.T., Morris M.L., 2009b, *MNRAS*, submitted (Chapter 5)
- Weldrake D.T.F., de Blok W.J.G., Walter F., 2003, *MNRAS*, 340, 12
- White S.D.M., 1980, *MNRAS*, 191, 1p
- Wilman R.J., Jarvis M.J., Röttgering H.J.A., Binette L., 2004, *MNRAS*, 351, 1109
- Wilman R.J., Gersten J., Bower R.G., Morris S.L., Bacon R., de Zeeuw P.T., Davies R.L., 2005, *Nature*, 436, 227
- Worthey G., Ottaviani D.L., 1997, *ApJS*, 111, 377
- Zibetti S., Charlot S., Rix H.-W., 2009, *MNRAS*, submitted (arXiv0904.4252)
- Zwicky F., 1933, *Helvetica Physica Acta*, 6, 110



# Publicatielijst

## REFEREED PAPERS

- **Spectroscopic mapping of the stellar and dark halo of the early-type galaxy NGC 2549** (Chapter 4)  
A. Weijmans, J. Gerssen, M. Cappellari, P.T. de Zeeuw, J. Falcón-Barroso, H. Kuntschner, R.C.E. van den Bosch  
*2009, MNRAS, to be submitted*
- **Dissecting the Lyman Alpha emission halo of LAB1** (Chapter 5)  
A. Weijmans, R.G. Bower, J.E. Geach, A.M. Swinbank, R.J. Wilman, P.T. de Zeeuw, S.L. Morris  
*2009, MNRAS, submitted*
- **Stellar velocity profiles and line strengths out to four effective radii in the early-type galaxies NGC 3379 and NGC 821** (Chapter 3)  
A. Weijmans, M. Cappellari, R. Bacon, P.T. de Zeeuw, E. Emsellem, J. Falcón-Barroso, H. Kuntschner, R.M. McDermid, R.C.E. van den Bosch, G. van de Ven  
*2009, MNRAS, in press, arXiv0906.0018*
- **The shape of the dark matter halo in the early-type galaxy NGC 2974** (Chapter 2)  
A. Weijmans, D. Krajnović, G. van de Ven, T.A. Oosterloo, R. Morganti, P.T. de Zeeuw  
*2008, MNRAS, 383, 1343–1358*
- **The kinematics and morphology of the HI in gas-poor galaxies**  
T.A. Oosterloo, R. Morganti, P.T. de Zeeuw, R.M. McDermid, D. Krajnović, M. Cappellari, F. Kenn, A. Weijmans, M. Sarzi  
*2007, NewAR, 51, 8–12*

- **Neutral hydrogen in nearby elliptical and lenticular galaxies: the continuing formation of early-type galaxies**  
R. Morganti, P.T. de Zeeuw, T.A. Oosterloo, R.M. McDermid, D. Krajnović, M. Cappellari, F. Kenn, A. Weijmans, M. Sarzi  
2006, *MNRAS*, 371, 157–169

## CONFERENCE PROCEEDINGS

- **Stellar populations of early-type galaxies in the ATLAS<sup>3D</sup> sample**  
P. Serra, R.M. McDermid, K. Alatalo, L. Blitz, M. Bois, F. Bournaud, M. Bureau, M. Cappellari, R.L. Davies, T.A. Davis, P.T. de Zeeuw, E. Emsellem, J. Falcón-Barroso, S. Khochfar, D. Krajnović, H. Kuntschner, P.-Y. Lablanche, R. Morganti, T. Naab, M. Sarzi, N. Scott, R.C.E. van den Bosch, G. van de Ven, A. Weijmans, L.M. Young  
2009, *Probing Stellar Populations out of to the Distant Universe, AIP Conference Proceedings, Volume 1111, pp 111–114*
- **Stellar velocity profiles and line strengths out to four effective radii in the early-type galaxies NGC 3379.** A. Weijmans, M. Cappellari, P.T. de Zeeuw, E. Emsellem, J. Falcón-Barroso, H. Kuntschner, R.M. McDermid, R.C.E. van den Bosch, G. van de Ven  
2008, *to appear in Galaxy Evolution: Emerging Insights and Future Challenges (arXiv0811.2840)*
- **The continuing formation of early-type galaxies: an HI survey**  
R. Morganti, E. Manthey, A. Crocker, T.A. Oosterloo, P.T. de Zeeuw, R.M. McDermid, D. Krajnović, M. Cappellari, A. Weijmans, M. Sarzi  
2008, *The Evolution of Galaxies through the Neutral Hydrogen Window, AIP Conference Proceedings, Volume 1035, pp 129–131*
- **Dark matter in NGC 2974**  
A. Weijmans, D. Krajnović, T.A. Oosterloo, R. Morganti, P.T. de Zeeuw  
2007, *Galaxy Evolution Across the Hubble Time, eds. F. Combes, J. Palous, Proceedings of the International Astronomical Union, IAU Symposium 235, pp 147*

- **VADER: a satellite mission concept for high precision dark energy studies**

R. Fassbender, J. Stegmaier, A. Weijmans, S. Köstner, A. Kruselburger, C. Diethart, P. Fertl, E. Valiante, M. Hayes, P. Schuecker, G. Hasinger

2006, *Space Telescopes and Instrumentation II: Ultraviolet to Gamma Ray*, Eds. M.J.L. Turner, G. Hasinger, *Proceedings of the SPIE*, Volume 6266, pp 626632

#### POPULAR ARTICLES

- **SAURON ziet alles...**

A. Weijmans

2008, *Eureka!*, November, edition 23

- **SAURON – het oog dat alles ziet**

A. Weijmans & D. Krajnović

2005, *Zenit*, September, pp 393–395

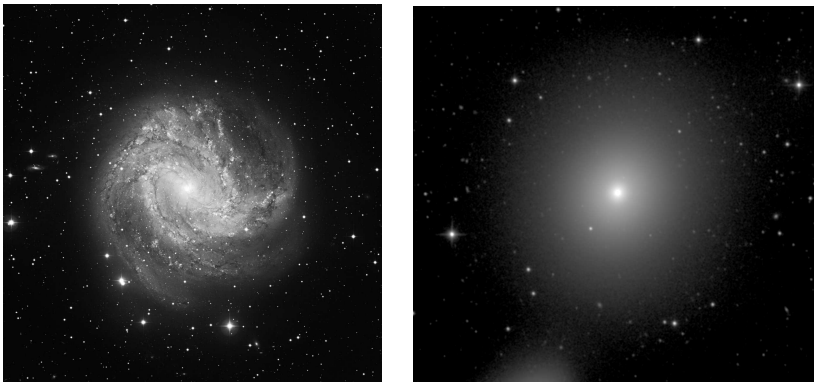


# Nederlandse samenvatting

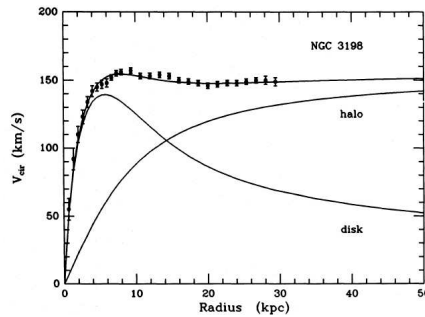
Sterrenstelsels komen in alle maten en soorten aan de hemel voor. Sommige hebben indrukwekkende spiraalarmen en stofschijven, andere zijn elliptisch en zien er wat eenvoudiger uit, zo op het eerste gezicht zonder duidelijke structuur (Figuur 1). Hoe zijn deze sterrenstelsels ontstaan en hoe hebben zij zich tot zo veel verschillende vormen kunnen ontwikkelen? Dit zijn enkele van de grote vragen waarop sterrenkundigen een antwoord proberen te vinden.

## Donkere materie in sterrenstelsels

Wanneer we sterrenstelsels bestuderen, doen we dat in de eerste plaats door te kijken naar hun sterren, stof en gas. Deze zijn relatief eenvoudig vast te leggen met CCD-camera's. Daarnaast kunnen we met spectrografen de spectra van stelsels opnemen en hieruit zowel de bewegingen van ster-



**Figuur 1** — Afbeeldingen van twee type sterrenstelsels. Links: spiraal stelsel M83, vastgelegd door de Wide Field Imager van La Silla Observatory, Chili (Credit: ESO), rechts elliptisch stelsel NGC 3379, vastgelegd door de 1,3m McGraw-Hill Telescoop van het MDM Observatory, Kitt Peak, Verenigde Staten.



**Figuur 2** — Links: de Westerbork Radio Synthesis Telescope (Bron: ASTRON). Rechts: een rotatiekromme van een sterrenstelsel, waargenomen door de WRST (van Albada et al. 1985). De horizontale as geeft de afstand in het stelsel weer, de verticale as de gemeten snelheid. De snelheid blijft hoog, zelfs op grote afstand van het centrum van het sterrenstelsel, wat duidt op een grote hoeveelheid donkere materie.

ren en gas, als de chemische samenstelling van een sterrenstelsel bepalen. Maar de belangrijkste component van een sterrenstelsel is letterlijk onzichtbaar: de zogenaamde donkere materie. Donkere materie is anders dan de normale (baryonische) materie waar we op aarde aan gewend zijn. We weten niet precies wat donkere materie is, maar we weten wel dat er ongeveer vijf keer zoveel donkere materie als normale materie in het heelal is. Donkere materie heeft een grote rol gespeeld in de vorming van structuur in het heelal en dus bij het ontstaan en de ontwikkeling van sterrenstelsels. Daarom zullen we, als we de evolutie van sterrenstelsels willen begrijpen, ook moeten kijken naar de donkere materie. Dat is het onderwerp van dit proefschrift.

Maar hoe bestudeer je iets dat onzichtbaar is? Donkere materie heeft geen enkele interactie met de elektromagnetische kracht, wat wil zeggen dat het geen licht uitzendt en ook geen licht absorbeert. Maar donkere materie heeft wel interactie met de zwaartekracht. Door naar de bewegingen van sterren en gas binnen sterrenstelsels te kijken, kunnen we bepalen waar de donkere materie zit en hoeveel ervan in het stelsel zit. Met radiotelescopie, zoals de Westerbork Radio Synthesis Telescope (WRST) in Drenthe (Figuur 2, links), zijn veel gasschijven van neutraal waterstof rond spiraalstelsels bestudeerd. Aan de hand van de rotatiekrommen die hieruit volgden (Figuur 2, rechts) is gevonden dat deze stelsels in een zogenaamde halo van donkere materie liggen. In het centrum van zo'n halo is ooit gas

samengeklonterd dat sterren is gaan vormen. Vandaar dat in het centrum van een sterrenstelsel sterren en gas domineren en pas op grotere afstand de invloed van de donkere halo merkbaar wordt.

In tegenstelling tot spiraalstelsels hebben elliptische stelsels vaak geen grote gasschijf of ring, waarmee de donkere materie getraceerd kan worden. Om toch de zwaartekrachtspotentiaal, en daarmee de massaverdeling van een stelsel in kaart te brengen, moeten we dus een andere component gebruiken. Door het meten van de bewegingen van de sterren (hun kinematica) kunnen we in principe ook in elliptische stelsels de eigenschappen van de donkere halo bepalen. Het probleem is echter, dat in tegenstelling tot het gas in gasschijven, de hoeveelheid sterren en daarmee de sterkte van het sterlicht snel afneemt op grote afstand van het centrum. De donkere halo is pas op grotere afstand merkbaar, voorbij zo'n 3 tot 4 effectieve stralen<sup>1</sup>. Met traditionele spectrografie kunnen we hier vaak niet genoeg sterlicht waarnemen. Vandaar dat voor elliptische stelsels verschillende andere technieken zijn ontwikkeld om de halo te bestuderen, waarbij gebruik wordt gemaakt van andere componenten in het stelsel.

Sommige elliptische stelsels bevatten heet gas, met temperaturen boven de 10 miljoen graden. Met speciale ruimtetelescopen kan de röntgenstraling worden opgevangen die dit hete gas uitzendt en kunnen de temperatuur en dichtheid van het gas worden bepaald. Met behulp van thermodynamische wetten kan dan vervolgens de massa worden uitgerekend die nodig is om het gas in de waargenomen toestand te behouden. Door de lichtgevendende massa (sterren en gas) met deze totale massa te vergelijken is dan de massa van de donkere materie bekend.

Een andere methode is te kijken naar de kinematica van bepaalde sterpopulaties. Het vaakst worden hiervoor planetaire nevels gebruikt. Dit zijn sterren met een massa kleiner dan acht zonsmassa's (1 zonsmassa =  $M_{\odot} = 2 \times 10^{30}$  kg), die aan het einde van hun leven zijn gekomen en hun buitenste sterlagen afstoten. Deze sterren zullen hun laatste levensdagen slijten als witte dwergen en langzaam afkoelen en uitdoven. Onze zon staat over zo'n 4,5 miljard jaar dit lot te wachten.

Planetaire nevels in onze eigen Melkweg leveren prachtige plaatjes op (Figuur 3, links), maar ook in andere sterrenstelsels kunnen we straling van deze sterren oppikken, omdat ze sterk stralen in een bepaalde emissielijn

---

<sup>1</sup>Afstanden binnen sterrenstelsels worden vaak uitgedrukt in effectieve straal. Eén effectieve straal omringt de helft van het totale sterlicht in het sterrenstelsel.



**Figuur 3** — Twee objecten waarvan de radiële snelheden gebruikt kunnen worden om donkere materie in elliptische sterrenstelsels te traceren. Links: een planetaire nevel (Helix nevel). Rechts: een bolvormige sterhoop (47 Tuc). Credits: ESO.

(de [O III] lijn, veroorzaakt door geïoniseerd zuurstof in de afgestoten sterlagen). Met behulp van deze emissielijn kan van iedere planetaire nevel de radiële snelheidscomponent<sup>2</sup> worden bepaald. Door van een groot aantal planetaire nevels deze snelheden te meten, kan een massamodel worden opgesteld dat deze snelheden kan verklaren. Dit massamodel kan vergeleken worden met de massa aanwezig in sterren en gas om de massa van de donkere halo te bepalen.

Behalve planetaire nevels kunnen ook bolvormige sterhopen voor deze techniek worden gebruikt. Dit zijn verzamelingen van honderdduizenden sterren, die gravitationeel aan elkaar gebonden zijn (Figuur 3, rechts). Bolvormige sterhopen zijn door het licht van hun vele sterren erg helder en kunnen daarom ook in andere stelsels dan de Melkweg worden waargenomen.

Helaas kunnen deze methodes niet voor alle elliptische stelsels gebruikt worden. Niet alle stelsels hebben heet gas en bovendien moet de aanname gemaakt worden dat het gas in evenwicht is, wat niet altijd het geval hoeft te zijn. Om een massamodel op te stellen aan de hand van planetaire nevels of bolvormige sterhopen moet de snelheid van een groot aantal van deze objecten gemeten worden, wat niet altijd mogelijk is. Daarbij moet aangetoond worden dat de planetaire nevels of bolhopen een representatieve afspiegeling zijn van de totale sterpopulatie. Als we in plaats daarvan het totale sterlicht gebruiken, vermijden we deze aannames. Bovendien

---

<sup>2</sup>De radiële snelheid is de snelheid waarmee een object zich van ons af beweegt.



kunnen we door de kinematica van het sterlicht te meten ook de verdeling van sterbanen benaderen, wat gebruikt kan worden bij het opstellen van het massamodel. In dit proefschrift maken we daarom gebruik van een nieuwe techniek, waarbij we integral-field spectrografie gebruiken om in de zwakke buitendelen van sterrenstelsels toch voldoende licht te verzamelen voor een bruikbaar spectrum.

## Integral-field spectrografie

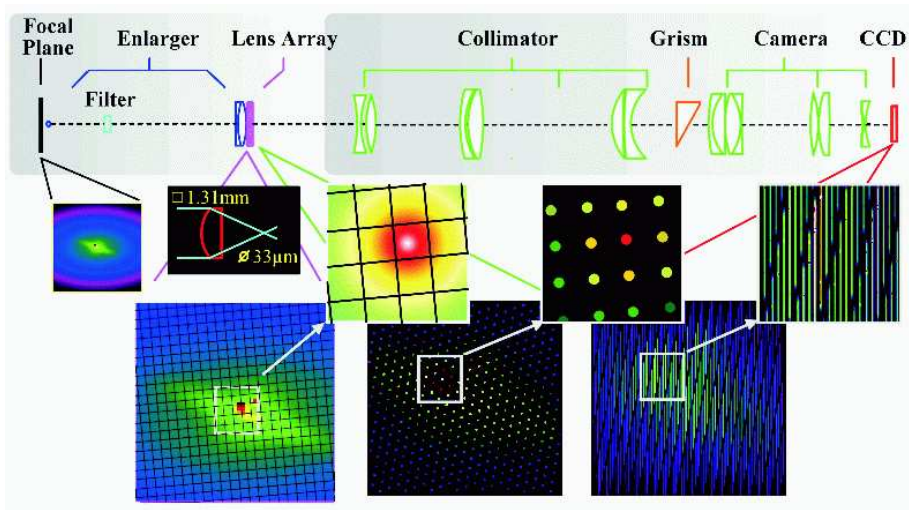
Integral-field spectrografie is een techniek waarmee gelijktijdig spectra genomen kunnen worden in een groot gezichtsveld. Voor iedere positie  $(x, y)$  binnen het gezichtsveld wordt een spectrum genomen. Hiermee kunnen we op iedere positie zowel de kinematica van sterren en gas als de chemische samenstelling van de sterren bepalen. Met de kinematica kunnen we de massaverdeling van het stelsel achterhalen (en dus ook de hoeveelheid donkere materie), terwijl de chemische samenstelling informatie geeft over de leeftijd en het metaalgehalte van de sterren en daarmee ook over het verloop van de stervorming.

In dit proefschrift hebben we voornamelijk gebruik gemaakt van de integral-field spectrograaf SAURON (Spectrographic Aerial Unit for Research on Optical Nebulae). Deze spectrograaf heeft lensjes, die het licht opvangen en naar een tralie sturen, waar het licht van ieder lensje in een apart spectrum uiteen wordt gerafeld (zie Figuur 4). SAURON is speciaal ontworpen voor de William Herschel Telescope van de Isaac Newton Group op het Canarische eiland La Palma, Spanje.

Daarnaast maken we in één hoofdstuk gebruik van de integral-field spectrograaf PPAK. PPAK werkt in tegenstelling tot SAURON niet met lensjes, maar met fibers die het licht opvangen. Deze spectrograaf heeft een groter gezichtsveld dan SAURON en kan spectra over een langer golflengte gebied nemen, wat inhoudt dat we de leeftijd en het metaalgehalte van de sterren beter kunnen bepalen. De spatiële resolutie is echter lager: een fiber heeft een doorsnede van 2,7 boogseconden<sup>3</sup>, terwijl een lensje van SAURON 0,94 bij 0,94 boogseconden meet. PPAK hoort bij het instrumentarium van de 3,5m telescoop op Calar Alto, nabij Almeria, Spanje.

---

<sup>3</sup>1 boogseconde is 1/60 boogminuut, ofwel 1/3600 graad. Dit is te vergelijken met de grootte van een euromunt op een afstand van 4,7 km. Ter vergelijking: de volle maan heeft een doorsnede van 30 boogminuten.



**Figuur 4** — Optische lay-out van de integral-field spectrograaf SAURON. Het filter zorgt ervoor dat alleen licht uit een bepaald golflengtegebied wordt doorgelaten. Het gezichtsveld wordt vergroot en het licht wordt opgevangen door de lensjes. Deze sturen het licht door naar een grisma (een prisma met een tralie), dat het licht uiteenrafelt in een spectrum. De spectra van ieder lensje worden afgebeeld op de CCD.

## Dit proefschrift

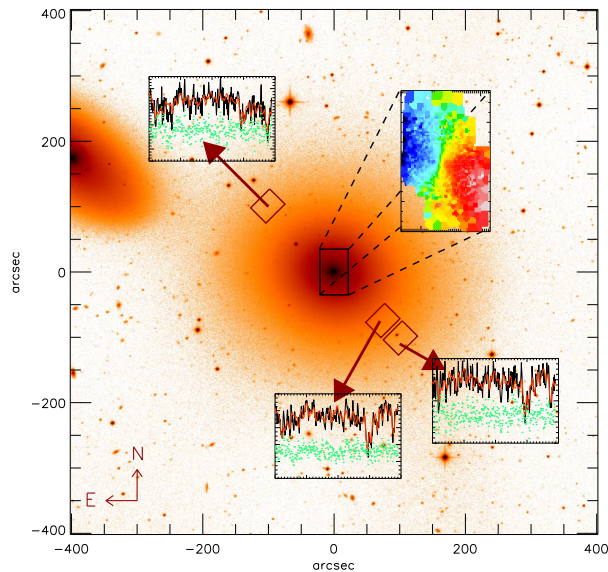
In **hoofdstuk 2** van dit proefschrift modelleren we het elliptische stelsel NGC 2974. Dit stelsel is uitzonderlijk, omdat het één van de weinige elliptische stelsels is met een ring van neutraal waterstof. We hebben de kinematica van de gasring in kaart gebracht met de Very Large Array (VLA), een radiotelescoop in New Mexico, VS. De ring heeft een diameter van 12 kpc, wat voor dit stelsel overeenkomt met 5 effectieve stralen<sup>4</sup>. Met behulp van deze radiodata stellen we een rotatiekromme op voor NGC 2974, maar doordat we met een ring te maken hadden en niet met een schijf, ontbreekt de kromme voor het binnenste gedeelte van het stelsel. Daarom gebruiken we ook gegevens van SAURON, die al voor een ander project het binnengebied van NGC 2974 (tot 1 effectieve straal) in kaart had gebracht. We combineren de kinematica van geïoniseerd, warm gas in het centrum en neutraal koud gas uit de ring tot één rotatiekromme en stellen een massamodel voor het stelsel op. Hieruit blijkt dat NGC 2974 een ha-

<sup>4</sup>Een kpc of kiloparsec is een afstandsmaat binnen de sterrenkunde, en komt overeen met  $3 \times 10^{16}$  kilometer, ofwel 3260 lichtjaar.

lo van donkere materie nodig heeft om de waargenomen rotatiekromme te kunnen verklaren: binnen een straal van 5 effectieve stralen is ten minste 55% van de totale hoeveelheid materie donker.

**Hoofdstuk 3** is gewijd aan twee andere elliptische stelsels, NGC 3379 en NGC 821. Deze stelsels hebben geen neutraal waterstofgas, dus om de halo te kunnen modelleren maken we gebruik van de sterkinematica. Hiervoor hebben we een nieuwe techniek ontwikkeld: we gebruiken SAURON als een “lichtvanger”. In het binnengedeelte van het sterrenstelsel is voldoende licht om op iedere positie een spectrum te meten, en daarmee de sterkinematica. Op grotere afstand is het sterlicht hiervoor te zwak, maar als we het licht van alle posities (ofwel van alle lensjes) bij elkaar optellen, krijgen we een spectrum waaruit we wel de kinematica kunnen halen (zie Figuur 5). Door de kinematica van het binnenveld te combineren met de kinematica van de spectra op grotere afstand van het centrum, kunnen we een massamodel opstellen. Voor beide stelsels is donkere materie nodig om de sterkinematica op grote straal in het model te kunnen reproduceren, net zoals we met gaskinematica hadden vastgesteld in NGC 2974. We vinden dat in NGC 3379 ten minste 34% van de massa donker is binnen 4 effectieve stralen, en voor NGC 821 is dit zelfs 49%.

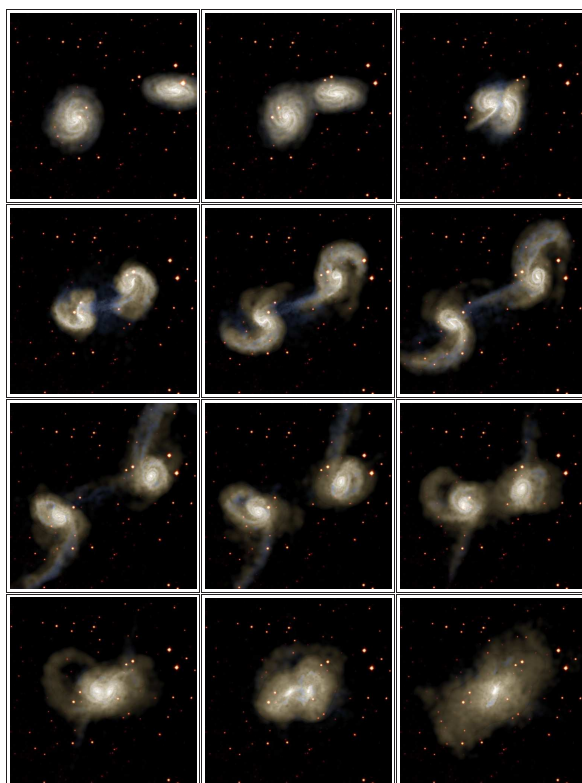
Daarnaast kunnen we uit de sterspectra de chemische samenstelling van de sterren bepalen. We kijken vooral naar de hoeveelheid magnesium in de sterren, wat een maat is voor het metaalgehalte. Het metaalgehalte van sterren is belangrijk om de stervormingsgeschiedenis van een sterrenstelsel te bepalen: als sterren metaalrijk zijn, zijn ze gevormd uit metaalrijk gas, dat weer uitgestoten is door zware stervende sterren. Dit betekent dus dat metaalrijke sterren pas vanaf een bepaald moment in het heelal konden ontstaan, namelijk pas nadat eerdere sterren metalen hadden gevormd en weer uitgestoten. Wij vinden dat het magnesiumgehalte van de sterren in NGC 3379 afneemt met afstand tot het centrum. Het was al bekend dat dit verschijnsel optreedt binnen één effectieve straal, en onze waarnemingen hebben laten zien dat deze afname doorzet tot ten minste 4 effectieve stralen. De sterren in de halo zijn dus metaalarmer en daarmee ook ouder dan de sterren in het centrale gedeelte van het sterrenstelsel. Dit sluit aan bij de theorie dat elliptische stelsels ontstaan door het samensmelten van twee spiraalstelsels. Bij zo’n botsing beweegt het gas van de spiraalstelsels naar het centrum, waar dan stervorming optreedt. Het resultaat is een elliptisch stelsel met een schijf jonge sterren in het centrum, omhuld door oudere



**Figuur 5** — Toelichting van het gebruik van SAURON als “lichtvanger”. Het onderliggende plaatje is een afbeelding van het elliptische sterrenstelsel NGC 3379. In het centrum levert SAURON een snelheidsveld. Op grotere afstand van het centrum levert het sterrenstelsel te weinig sterlicht om een snelheidskaart samen te stellen. We tellen daarom het licht van alle lensjes bij elkaar op en krijgen zo één spectrum, waaruit we de sterkinematica kunnen bepalen.

sterren uit de oorspronkelijke spiraalstelsels. Figuur 6 laat een aantal beelden zien uit een computersimulatie, waarin twee spiraalstelsels botsen en een elliptisch stelsel ontstaat.

In **hoofdstuk 4** kijken we naar een ander stelsel zonder neutraal waterstofgas: NGC 2549. Dit stelsel is een lensstelsel en bevindt zich qua vorm op het grensgebied van elliptische en spiraalstelsels: lensstelsels zijn structuurloos (geen spiraalarmen), maar hebben wel vaak een duidelijk zichtbare sterschijf. Met PPAK hebben we een mozaïek waargenomen van dit stelsel, dat zich uitstrekt tot 5 effectieve stralen (6 kpc). We bepalen de sterkinematica en de chemische samenstelling. In de kinematica vinden we aanwijzingen voor een tweede sterschijf, die verstopt zou zitten in een grotere schijf. Dit zou kunnen duiden op een jongere schijf, ontstaan bij het samensmelting van twee stelsels bij de vorming van NGC 2549. We vinden hiervoor aanvullende bewijzen in de chemische samenstelling van het stelsel: het centrum is jonger en metaalrijker. Ook van dit stelsel stellen we een massamodel op, en we gebruiken een hogere resolutie SAURON



**Figuur 6** — Een computersimulatie van twee botsende spiraalstelsels. Door de getijdekrachten worden de stelsels uitgerekt en verliezen ze gas en sterren. Uiteindelijk smelten de twee stelsels samen tot een elliptisch stelsel. Figuur uit Springel & White (1999), ter beschikking gesteld door het Max-Planck-Institut für Astrophysik.

kaart voor het centrale gedeelte. Door het grote mozaïek hebben we een veel groter aantal onafhankelijke waarnemingen dan in hoofdstuk 3, en heeft het model minder vrijheid. Ons model kan daarom de waarnemingen niet precies reproduceren en moet dus nog verbeterd worden. Wel kunnen we vaststellen dat ook NGC 2549 omringd is door een donkere halo: ten minste 63 procent van de totale massa binnen 5 effectieve stralen is donker.

Ten slotte maken we in **hoofdstuk 5** een uitstapje naar hoge roodverschuiving. Met SAURON bestuderen we de structuur en de kinematica van een wolk waterstofgas op een roodverschuiving van 3,1, wat overeenkomt met een afstand van 11,5 miljard lichtjaar. De straling die we van deze wolk oppikken is uitgezonden toen het heelal nog maar 2 miljard jaar oud

was, minder dan een vijfde van zijn huidige leeftijd.

De gaswolk die we in dit hoofdstuk bekijken, bevindt zich in een proto-cluster (gebied in het heelal met een hoge dichtheid aan materie, waaruit zich een cluster van sterrenstelsels zal ontwikkelen) en straalt voornamelijk in een bepaalde waterstoflijn, namelijk de Lyman  $\alpha$  lijn. De gaswolk staat bekend onder de naam LAB1, wat staat voor Lyman Alpha Blob 1. Behalve deze LAB zijn nog vele andere LABs bekend, maar LAB1 is de grootste, met een doorsnede van meer dan 100 kpc (326 000 lichtjaar). Het is niet bekend wat deze LABs precies zijn en waar ze hun energiebron vandaan halen, vandaar dat deze objecten bij sterrenkundigen erg in de belangstelling staan.

SAURON neemt alleen spectra waar over een beperkt golflengtegebied, dat geoptimaliseerd is voor het waarnemen van spectra van sterrenstelsels in het nabije heelal. De Lyman  $\alpha$  lijn valt eigenlijk buiten dit gebied, maar als deze lijn wordt uitgezonden op een roodverschuiving tussen 3,0 en 3,4, is de lijn zover verschoven dat deze weer door SAURON kan worden opgepikt. We hebben dus 'geluk' dat LAB1 op een voor SAURON gunstige roodverschuiving staat.

Met onze diepe waarnemingen (meer dan 23,5 uur!) zien we dat LAB1 niet één grote blob is, maar uit 5 kleine blobjes bestaat. We vergelijken vervolgens onze waarnemingen met die van de Hubble Ruimte Telescoop (optisch licht) en de Spitzer Ruimte Telescoop (infrarood licht). Daarmee kunnen we aantonen dat twee van de blobjes samenvallen met sterrenstelsels. Met de SAURON spectra bepalen we van deze twee blobjes een snelheidsveld en vinden dat deze twee stelsels waarschijnlijk materiaal (gas) aan het uitstoten zijn. Een derde blobje komt overeen met een bron die wel zichtbaar is in het infrarood, maar niet in het optisch. Deze bron is waarschijnlijk een sterrenstelsel dat een uitbarsting van stervorming ondergaat van meer dan 1000 zonsmassa's aan sterren per jaar. Dit gaat gepaard met stofontwikkeling, waardoor het stelsel alleen in het infrarood en langere golflengtes zichtbaar is. Voor de twee resterende blobjes kunnen we geen onderliggende bron vinden. Dit zouden dus losse gaswolken kunnen zijn, gevangen in het zwaartekrachtsveld van de proto-cluster. De energiebron voor deze twee blobjes is daarmee niet helemaal duidelijk. We concluderen dat de kleine blobjes waaruit LAB1 bestaat veel overeenkomsten hebben met andere kleinere LABs, maar dat LABs onderling sterk kunnen verschillen.



## Conclusies en vooruitblik

Door het gebruik van integral-field spectrografie is het nu mogelijk om sterkinematica in de buitendelen van sterrenstelsels te meten. Dit houdt in dat we nu voor elliptische stelsels massamodellen kunnen bouwen, waarmee we de donkere halo in kaart kunnen brengen, net zoals dat al voor spiraalstelsels met gaskinematica is gedaan.

Er zitten echter ook wat onzekerheden in deze modellen, die we in dit proefschrift nog niet hebben kunnen oplossen. Zo is één van de onzekerheden in de modellen de totale massa van de sterren. We zijn in hoofdstuk 3 uitgegaan van een maximaal toegestane sterre-massa, wat inhoudt dat als de eigenlijke sterre-massa kleiner is, de donkere halo dus zwaarder kan zijn. In hoofdstuk 4 hebben we de sterre-massa nauwkeuriger kunnen bepalen, omdat we spectra over een groter golflengtegebied tot onze beschikking hadden, waardoor de eigenschappen van de sterpopulatie beter bepaald konden worden. Met spectra over langere golflengtegebieden kunnen we deze onzekerheid dus uit onze modellen halen. Daarnaast zijn we steeds uitgegaan van een bolvormige halo, terwijl de meeste theorieën op het gebied van de vorming van sterrenstelsels juist een drie-assige halo voorspellen. Dit zou kunnen verklaren waarom ons model in hoofdstuk 4 de waarnemingen niet precies kan reproduceren. Wij zijn van plan hier in toekomstige artikelen dieper op in te gaan en de effecten van een drie-assige halo op de sterpopulatie te onderzoeken.

Een volgende stap is het onderzoeken van halo's rond sterrenstelsels op verschillende roodverschuivingen, zodat we de ontwikkeling van de donkere halo kunnen volgen in de tijd. In dit proefschrift hebben we alleen gekeken naar sterrenstelsels in het nabije heelal, op een afstand minder dan 50 Mpc (= 160 miljoen lichtjaar). Als we de kinematica van sterren en gas op grotere afstand willen bestuderen, verliezen we spatiële resolutie, die juist nodig is om een nauwkeurig massamodel te maken. Daarnaast zijn deze stelsels lichtzwak doordat ze ver van ons verwijderd zijn. Daarom hebben we lange waarneemtijden nodig om toch voldoende signaal van deze objecten te verzamelen. Hoofdstuk 5 is hiervan een illustratie. Toch worden nu al snelheidskaarten gemaakt van schijfstelsels op hogere roodverschuiving (tot 10 miljard lichtjaar) met integral-field spectrografen op 8-meter telescopen. Ook kan handig gebruik gemaakt worden van zogenaamde gravitationele lenzen: als een sterrenstelsel op grote afstand ach-

ter een zware cluster van sterrenstels staat, werkt de cluster als een soort lens en zien we een weliswaar vervormd, maar ook uitvergroot beeld van het verre sterrenstelsel. Zo zijn de gaskinematica al in kaart gebracht van sterrenstelsels op afstanden van 7,8 miljard lichtjaar, terwijl de spatiële resolutie zo goed is alsof het stelsel slechts 1,3 miljard lichtjaar van ons verwijderd is.

Uiteindelijk willen we weten hoe sterrenstelsels ontstaan en hoe zij zich verder ontwikkelen. Waarnemingen aan stelsels in het nabije en in het verre heelal laten ons zien hoe sterrenstelsels in de loop van de tijd veranderen door stervorming en interacties met andere stelsels. Maar als we deze waarnemingen goed willen begrijpen, zullen we ook theorieën moeten ontwikkelen over de vorming en evolutie van sterrenstelsels waarmee we de waarnemingen kunnen verklaren. Op supercomputers worden simulaties gedraaid waarin sterrenstelsels ontstaan, groeien en kunnen samensmelten met andere stelsels. De verdeling van donkere materie die vanuit deze simulaties wordt voorspeld komt nog niet overeen met wat de waarnemingen ons vertellen. Waarnemingen en theorie zullen dus samengebracht moeten worden om het raadsel van de vorming en evolutie van sterrenstelsels te kunnen doorgronden.



## Curriculum vitae

Op 16 november 1981 ben ik geboren in Boxmeer. Na een aantal jaren in het Limburgse Venray te hebben gewoond, verhuisde ik naar het Zeeuwse Kortgene. In 1999 rondde ik het gymnasium af aan het Goese Lyceum. Daarna vertrok ik naar Leiden voor een doctoraal studie sterrenkunde. Ik bracht drie maanden door in Oxford voor een onderzoek naar de fotometrische eigenschappen van sterrenstelsels in de cluster Abell 1689, onder leiding van dr. J.M. Barr en prof. dr. R.L. Davies. Mijn afstudeeronderzoek naar de intrinsieke vormen van vroeg-type sterrenstelsels voerde ik uit in de groep van prof. dr. P. T. de Zeeuw en in 2004 sloot ik mijn studie sterrenkunde cum laude af. Gedurende mijn studententijd was ik nauw betrokken bij het organiseren van en lesgeven op examencursussen voor middelbare scholieren, door de Stichting Studiebegeleiding Leiden en de Universiteit Leiden.

In 2005 begon ik met mijn promotie-onderzoek onder leiding van prof. dr. P. T. de Zeeuw, waarvan de resultaten in dit proefschrift worden besproken. Voor mijn onderzoek heb ik met verschillende telescopen waargenomen op La Palma, Calar Alto en Kitt Peak. Ik nam deel aan een zomerschool in Oostenrijk, waar de opdracht een eigen ruimtemissie te ontwerpen uitmondde in het VADER project. Ook bracht ik werkbezoeken aan de Universiteiten van Oxford en Durham (Verenigd Koninkrijk), het Institute for Advanced Study te Princeton (Verenigde Staten), het Observatoire de Lyon (Frankrijk) en het European Southern Observatory (Duitsland). Ik presenteerde mijn promotieonderzoek op verscheidene conferenties in Brazilië, Duitsland, Mexico, Nederland, Tsjechië en de Verenigde Staten.

Ik heb tweemaal geassisteerd bij het Sterrenkundig Practicum 2 en de studentprojecten van Daniel Szomoru en Sef Welles (Nijmegen) begeleid. Ik heb publieke lezingen gegeven door heel Nederland, waaronder lezingen voor kinderen. Ook ben ik mede-oprichter van de Nederlandse Sterrenkunde Olympiade en was voorzitter van het eerste organiserende comité.

Na mijn promotie zal ik als Dunlap Fellow werkzaam zijn aan het Dunlap Institute in Toronto, Canada.



## Nawoord

Een proefschrift schrijf je niet alleen: vele personen hebben direct en indirect een bijdrage geleverd aan dit boekje.

First of all, many thanks to my colleagues and co-authors for all their help and support. A special thank you to my Leiden and ESO colleagues, Davor, Eric, Glenn, Harald, Jesús, Michele, Remco and Richard, for all the fruitful, open discussions which were so helpful in writing this thesis. Het gaat natuurlijk om de inhoud, maar het oog wil ook wat: oom Clemens, hartelijk dank voor het ontwerpen van de prachtige kaft!

Jan-Pieter, Maarten en Chael: jullie waren geweldige kamergenoten. Dank voor alle koppen thee die jullie me hebben voorgezet en voor het verstoppertje van de chocola. Barbera, Caroline, Christianne, Demerese en Marieke: ik heb genoten van onze etentjes en filmavonden, ook al kwamen we door het vele geklets vaak niet eens aan de film toe. Eveline, Maarten, Marcel, Nathan en Ignas: het was geweldig om met jullie het eerste NeSO team te vormen. Een speciaal woord van dank voor de computergroep: David, Tycho, Erik en Aart, die soms eerder dan ik wisten dat ik een computerprobleem had. Kirsten, Jeanne, Anita en Liesbeth: bedankt voor jullie ondersteuning vanuit het secretariaat. Isolde, thanks for all your support that made my visits to ESO run so smoothly.

Buiten de sterrenkunde is er altijd de muziek. Ik heb met veel plezier afgelopen jaren meegespeeld met de Leidse Harmoniekapel en Sinfonietta Voorschoten en vele muziekvrienden gemaakt, te veel om hier op te noemen. Benjamin, bedankt voor al je wijze hobolessen. Chris en Florence, ons laatste optreden als blazertrio moet nog komen, maar ik weet al dat het een succes gaat worden. Bedankt dat jullie mijn Nederlandse samenvatting kritisch hebben doorgenomen. Kathryn, Patrick, Annette and Harry: thanks for exposing me to music I otherwise never would have discovered, and for providing the constant challenge to keep up with you.

De laatste regels van dit proefschrift zijn voor mijn familie. Frederike, pap en Graddy: bedankt voor jullie geduld, jullie steun en jullie liefde. Ik weet dat jullie nooit ver weg zijn.

Dit onderzoek werd gefinancierd door de Nederlandse Organisatie voor Wetenschappelijk Onderzoek (NWO) onder projectnummer 614.000.426. Dit proefschrift is mede mogelijk gemaakt door financiële steun van het Leids Kerkhoven-Bosscha fonds en het European Southern Observatory.



